



Kent Academic Repository

Žurauskas, Mantas (2014) *Advanced systems and methods for collecting accurate data in optical coherence tomography*. Doctor of Philosophy (PhD) thesis, University of Kent,.

Downloaded from

<https://kar.kent.ac.uk/48728/> The University of Kent's Academic Repository KAR

The version of record is available from

<https://doi.org/10.22024/UniKent/01.02.48728>

This document version

UNSPECIFIED

DOI for this version

Licence for this version

CC BY-NC-ND (Attribution-NonCommercial-NoDerivatives)

Additional information

Versions of research works

Versions of Record

If this version is the version of record, it is the same as the published version available on the publisher's web site. Cite as the published version.

Author Accepted Manuscripts

If this document is identified as the Author Accepted Manuscript it is the version after peer review but before type setting, copy editing or publisher branding. Cite as Surname, Initial. (Year) 'Title of article'. To be published in *Title of Journal*, Volume and issue numbers [peer-reviewed accepted version]. Available at: DOI or URL (Accessed: date).

Enquiries

If you have questions about this document contact ResearchSupport@kent.ac.uk. Please include the URL of the record in KAR. If you believe that your, or a third party's rights have been compromised through this document please see our [Take Down policy](https://www.kent.ac.uk/guides/kar-the-kent-academic-repository#policies) (available from <https://www.kent.ac.uk/guides/kar-the-kent-academic-repository#policies>).

University of Kent
School of Physical Sciences
Applied Optics Group

**Advanced systems and methods for collecting
accurate data in optical coherence
tomography**

Mantas Žurauskas

Abstract

Optical coherence tomography (OCT) has recently emerged as a valuable technique in biomedical research and medical diagnostics. OCT based instruments allow acquisition of high-resolution information about the internal structure of translucent organs and tissues without damaging the object. However, unaccounted object movements reduce the quality of acquired data, particularly in functional imaging and in OCT modalities that rely on continuous monitoring. Therefore there is a need for methods that allow mitigating the negative effects of the object movements on the data quality.

In this thesis we present several methods and devices that allow improving the accuracy of collected data. First we introduce a novel frequency multiplexing method for OCT, which enables simultaneous measurements using several frequency-encoded channels. By doing so, several parameters are measured in the same time, reducing the time to acquire the data and making the technology less sensitive to object movements. We employed the method to extend the functionality of several OCT modalities. We have applied the multiplexer to enable simultaneous *en face* time domain OCT imaging at different depths. We have demonstrated a polarisation sensitive OCT set-up where different multiplexer channels are employed to perform polarisation sensitive measurements.

Furthermore, we have demonstrated how the multiplexer can be applied to extend the sensitivity range in swept source based OCT systems. The experiments presented in this thesis illustrate the flexibility of our new multiplexing method, which has proven useful not only for increasing the accuracy of collected data, but as well for increasing the efficiency in using the light from the object.

Alternatively, we have investigated tracking as a way to improve the quality of the OCT data acquired from the moving targets. We have demonstrated a closed-loop tracking based set-up that uses low coherence interferometry to continuously monitor the cardiac dynamics of a *Drosophila melanogaster* embryo.

Acknowledgements

First of all, I would like to thank my supervisor Prof. Adrian Podoleanu for his continuous support throughout my PhD. A never-ending stream of great ideas supplied by Adrian formed my research and I am particularly grateful for that. Additionally, I would like to thank my co-supervisor Dr. George Dobre for having open doors for any questions.

Equally, I would like to thank the Applied Optics group for providing a good research environment, the encouragement and optimism that they had shared with me. In particular I would like to thank Dr. John Rogers and Dr. Adrian Bradu for their support.

I would like to thank Dr. Daniel Ferguson and Dr. Daniel Hammer for their advice on the closed-loop optical tracker.

I also acknowledge the European Research Council funding which enabled my research.

Abbreviations

2D	Two dimensions
3D	Three dimensions
AO	Adaptive optics
AOD	Acousto-optic deflector
AOM	Acousto-optic modulator
ASE	Amplified spontaneous emission
FWHM	Full width at half maximum
HWP	Half wave plate
LSLO	Line scanning laser ophthalmology
MEMS	Micro-electro-mechanical system
NI	National Instruments
OCT	Optical coherence tomography
OFDI	Optical frequency domain imaging
OPD	Optical path difference
PC	Personal computer
PS	Polarisation sensitive
PSI	Physical sciences incorporated
QWP	Quarter wave plate
RF	Radio frequency
RMS	Root mean square
SD	Spectral domain
SLD	Super luminescent diode
SLO	Scanning laser ophthalmology
SS	Swept source
TD	Time domain
TTL	Transistor-transistor logic
VCSEL	Vertical cavity surface emitting laser

Contents

Abstract	i
Acknowledgements	ii
Abbreviations	iii
1 Introduction	1
1.1 Introduction	1
1.1.1 Time domain optical coherence tomography	3
1.1.2 Swept source based optical coherence tomography	5
1.2 Thesis statement and contributions	6
1.3 Thesis summary	7
I Multiplexing	10
2 Multiplexing in OCT	11

2.1	Introduction	11
2.2	Multiple object beam imaging based multiplexing strategies	13
2.3	Single object beam imaging based multiplexing strategies	17
2.4	Future outlook	19
3	Optical design considerations for a novel Bragg cell based frequency domain multiplexer for optical coherence tomography	21
3.1	Introduction	21
3.2	Designing a multiplexer for a multichannel OCT system	25
3.2.1	Frequency domain multiplexing based OCT	25
3.2.2	Angular overlap of adjacent channels	28
3.2.3	Spatial overlap of adjacent channels	30
3.2.4	Multiplexer optical power budget	32
3.2.5	Operation in reflection	33
3.2.6	Channel quantity limitation	35
3.3	Application-related notes and discussion	35
3.3.1	Time domain <i>en face</i> multiple depth OCT	35
3.3.2	Long range SS-OCT	36
3.3.3	Polarisation sensitive imaging	36
3.3.4	Structured interference	38

3.4	Conclusions	39
4	Simultaneous multiple-depths <i>en face</i> optical coherence tomography using multiple signal excitation of acousto-optic deflectors	40
4.1	Introduction	40
4.2	Method	42
4.2.1	Set-up	42
4.2.2	Delay method	46
4.3	Results	51
4.3.1	RF spectrum of the photodetected signal	51
4.3.2	<i>En face</i> OCT imaging	52
4.4	Discussion	55
4.5	Conclusions	59
5	Multiplexing based polarisation sensitive <i>en face</i> optical coherence tomography	61
5.1	Introduction	61
5.2	Methods	63
5.2.1	Experimental set-up	63
5.2.2	De-multiplexing of RF spectrum of the photodetected signal	67

5.2.3	Method of calculating the sample reflectivity and birefringence parameters	70
5.3	Results	71
5.4	Discussion	74
5.5	Conclusions	76
6	Frequency multiplexed long range swept source optical coherence tomography	78
6.1	Introduction	78
6.2	Method	80
6.2.1	Set-up	80
6.2.2	Choice of excitation frequencies	83
6.2.3	Data processing	84
6.2.4	Choice of differential delay δ	86
6.3	Results	88
6.3.1	Spectrum	88
6.3.2	Imaging	90
6.4	Discussion	92
6.5	Conclusions	94

II Tracking	95
7 Review of methods for sample tracking and image stabilisation in optical coherence tomography	96
7.1 Introduction	96
7.2 Computational post-processing video stabilisation methods	99
7.3 Dithering reflectometer based real time tracking	100
7.4 Post processing using a witness channel	101
7.5 Real time correction with fast witness channel	104
7.6 Speckle informed tracking	105
7.7 Axial, hardware-based tracking	106
7.8 Conclusion	108
8 Closed loop tracked Doppler optical coherence tomography based heart monitor for the <i>Drosophila melanogaster</i> larvae	109
8.1 Introduction	109
8.2 Experimental setup	111
8.3 System characterisation using a vibrating phantom	113
8.4 Tracked monitoring of the <i>Drosophila</i> larva	117
8.5 Discussion and conclusions	120

9	Conclusions	122
9.1	Thesis achievements	122
9.2	Future work	125
9.2.1	Multiplexing based OCT	125
9.2.2	Closed-loop tracking for accurate data acquisition in low coherence interferometry based imaging and monitoring	126
9.3	List of publications	127
A	Supplementary list of technical documents about selected instruments used in the work presented in this thesis	129
	Bibliography	130

List of Figures

1.1	Time domain OCT setup based on Michelson interferometer.	3
2.1	Summary of the various multiplexing strategies employed in optical coherence tomography	12
2.2	Multiple interferometer based multiplexing strategies for multiple object beam imaging OCT	14
2.3	Polarisation multiplexed OCT	16
2.4	Two frequency shifting based OCT Strategies	18
3.1	Basic layout of OCT system employing a multiplexer	26
3.2	Several multiplexer-enabled imaging modalities.	27
3.3	Illustration of a Bragg cell operating at three frequencies where the spectrum of the optical source is comprised of four distinct wavelengths	28
3.4	Angular overlap threshold for three cases of 830 nm, 1050 nm and 1300 nm for TeO_2 Bragg cell, limited by a driving signal of 100 MHz frequency.	30

3.5	Optimisation of frequency distribution while maintaining non overlapping beams with thick delay elements	31
3.6	Diagram illustrating the distribution of optical power in the multiplexer operated with two driving signals of different frequency.	33
3.7	Proposed multiplexer set-ups based on transmission, reflection, polarisation in transmission and polarisation in reflection.	34
3.8	Layout of the multiplexer design that can be used to interrogate the polarisation properties of the sample at different depths.	37
4.1	Schematic layout of the multiple-depths <i>en face</i> OCT system	43
4.2	A drawing and a photograph depicting the light passing through a multiple delay element	45
4.3	Relationship between the beam separation, source bandwidth and the distance from the AOD	49
4.4	Typical frequency spectrum of the photodetected signal when all eight RF signals are applied simultaneously to the pair of AODs in the reference path	51
4.5	Normalised autocorrelation function for the compound source used in the experiments	53
4.6	A montage of eight <i>en face</i> OCT images of <i>rmadillidium vulgare</i> dorsal side and superimposed maximum values of eight simultaneously generated <i>en face</i> images of a tilted 10 pence coin	54
5.1	Schematic layout of the RF encoded polarisation OCT system	64

5.2	Typical photodetected RF spectrum when two signals are applied simultaneously to the AODs pair in the reference arm of the interferometer .	67
5.3	Normalized autocorrelation function for the compound source used in the experiments	72
5.4	<i>In-vitro</i> images of intact and thermally damaged muscle tissue	73
6.1	Schematic layout of the long range SS-OCT system	81
6.2	Frequency division multiplexer, where each diffracted beam traverses a different delay step	82
6.3	Data processing algorithm	85
6.4	Sensitivity curves in each channel versus optical path difference	88
6.5	Measured sensitivity curve for four channels	89
6.6	B-scan images of a tilted mouse head obtained with a long-range constant sensitivity SS-OCT system	91
7.1	Most common motion artefact correction techniques are patch-based cross-correlation image registration algorithms	98
7.2	The schematic of a dithering circle reflectometer guided tracking set-up and tracking algorithm	101
7.3	Schematic of a tracked OCT set-up employing fast SLO witness channel, where the vertical scanner is shared by both channels and waveforms that are used to drive the galvo-mirrors	102

7.4	Orthogonal scanning based motion artefact mitigation method where at least one image taken for each of the scenarios: Xfast, Yslow and Yfast, Xslow	103
7.5	Schematic of a fast SLO witness channel based tracking imaging set-up	104
7.6	Handheld probe for the freehand sample scanning	105
7.7	Single A-scan based axial tracking approach	107
8.1	Schematic layout of tracked Doppler OCT monitor	112
8.2	Photograph showing the vibrating target mounted in front of the objective lens	114
8.3	Oscilloscope trace of the Doppler signal acquired from a phantom under four different conditions	115
8.4	Frequency analysis of a typical frequency content of photodetected Doppler signal with and without trackings	116
8.5	<i>En face</i> OCT slice of a <i>Drosophila</i> larva	117
8.6	Images of the <i>Drosophila</i> larva illuminated by the tracking beam, collected using a camera	118
8.7	Signal from the Doppler OCT based larval heart rate monitor	119

Chapter 1

Introduction

1.1 Introduction

Biomedical research and medical diagnostics require a set of essential tools to be used for optical sensing and imaging. Key benefits of light based object interrogation techniques include high resolution, high speed and ability to perform measurements in a non-invasive or minimally intrusive fashion [168]. Optical coherence tomography (OCT) is based on coherence gating along the depth axis in the object investigated (measured or imaged). Even though OCT is a relatively new imaging technique [56], OCT based instruments are rapidly becoming an expected part of inventory in most well equipped hospitals and biomedical research facilities [150, 1].

OCT can offer high, up to 1-2 micrometer, resolution cross-sectional images from 1-3 millimetres deep biological tissues [117]. OCT based instruments typically have a small form factor and can provide images in a non-contact manner at high speeds. Due to their robustness and versatility, mainly fibre-based systems are currently used in OCT based instruments. All of the set-ups presented and discussed in this thesis

will be fibre-based.

In biomedical imaging it is commonly desirable to image objects *in vivo*, without disrupting the experimental environment in which the object is being observed or without altering its natural behaviour. In medical imaging and diagnostics it is important to avoid causing unnecessary discomfort to the patient. Therefore majority of the current applications rely on OCT to produce an accurate cross-sectional or volumetric data of motile objects.

Both time domain and swept source based confocal OCT systems require scanning to form the two dimensional (2D) and volumetric (3D) images. Therefore, due to object movements, the acquired images might not accurately represent the investigated object. An ever-increasing imaging speed partially mitigates the effects of sample movement [71, 63], however the diminishing amount of collected light that was backscattered from the sample reduces the signal to noise ratio and therefore it can be a limiting factor.

This thesis will investigate two distinct approaches, which can be used to mitigate the effects of sample movements to the accuracy of collected data. In the first part of this thesis we will investigate multiplexing as a way to perform OCT imaging in parallel, using several simultaneous channels. We propose a multiplexing method, based on the use of Bragg cells, that allows parallel operation on several simultaneous imaging channels. The data from all channels is acquired at the same time and therefore it allows unambiguous relative localisation of collected data. Additionally, the image acquisition speed is increased by a factor, which is proportional to the total number of imaging channels. In the second part of this thesis we will investigate object tracking as a way to improve the reliability of collected coherence gated data.

The principles of OCT have already been comprehensively presented in numerous

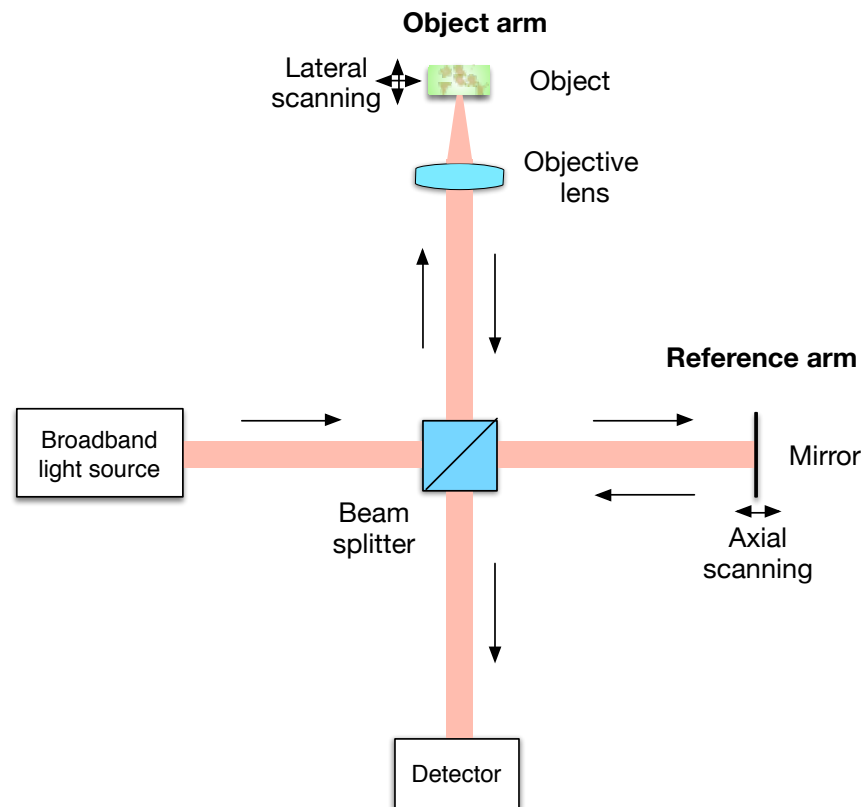


Figure 1.1: Time domain OCT setup based on Michelson interferometer. Arrows indicate the direction of light passing through the optical system.

peer-reviewed papers and books [11, 15, 33]. Therefore this thesis will provide only a brief introduction to the basic concepts underpinning OCT.

1.1.1 Time domain optical coherence tomography

Operation of a time domain OCT is based on low coherence interferometry using a Michelson interferometer. In its most basic form, a time domain OCT set-up consists of a broadband light source, beam splitter, reference mirror, objective lens and a detector. Such set-up is depicted in Fig.(1.1)

The light emitted by a broadband source is divided into an object and a reference

arm. In the object arm, the light is focused on the object using an objective lens. The backscattered light is collected using the same lens and launched back towards the beam splitter. The light in the reference arm is back-reflected by a mirror and the beam splitter recombines it with the light backscattered from the object to interfere on the photodetector. The intensity of the light as a function of optical path difference, $I(OPD)$, at the photodetector is defined by

$$I(OPD) = I_O + I_R + 2\sqrt{I_r I_s} \gamma(OPD) \Pi \cos\left(\frac{2\pi}{\lambda} OPD\right), \quad (1.1)$$

where I_O and I_R are the intensities of the light returned from the object and from the reference, $\gamma(OPD)$ is the cross-correlation function, Π is a polarisation term, $\frac{2\pi}{\lambda} OPD$ is the phase difference between the two beams. A cross-correlation function $\gamma(OPD)$ depends on the coherence length of a source l_c and to OPD .

$$\gamma(OPD) = \exp\left[-\ln(2)\left(\frac{2OPD}{l_c}\right)^2\right], \quad (1.2)$$

Axial resolution, δz , in low coherence interferometry depends on the coherence length of a source l_c . Therefore, here axial resolution is inverse proportional to the FWHM of the source optical bandwidth $\Delta\lambda$. For a Gaussian source, $\Delta\lambda$ and δz are related by

$$\delta z = \frac{l_c}{2} = \frac{2\ln 2}{\pi} \cdot \frac{\lambda_0^2}{\Delta\lambda}, \quad (1.3)$$

where λ_0 is the central optical wavelength. This is different from classic or confocal microscopy as here the axial resolution is decoupled from the numerical aperture of the objective lens or confocal pinhole size.

In time domain (TD) -OCT the image is formed by raster scanning the object. Lateral

scans are performed by scanning a focal point across an object. The scanning is usually accomplished by employing mirrors mounted either on galvoscaners or resonant scanners. For axial scans (A-scans) the reference mirror can be scanned to change the reference arm length.

1.1.2 Swept source based optical coherence tomography

Swept source based OCT uses a narrow band source, which is rapidly swept across the broad spectrum to perform the imaging. When an optical path difference (OPD) is introduced between the object and reference arms it creates modulation across the spectrum. The higher OPD values lead to the higher frequency modulation. In this way, when multiple reflectors are present in different depths, their position and reflectivity can be determined by measuring the frequency spectrum of the photo-detected signal.

Due to the Nyquist criterion, the highest frequency that can be detected by the photodetector determines the sensitivity range that can be achieved with a swept source based system. Therefore the largest OPD between the object and reference arm, OPD_{max} , can be found using a formula,

$$OPD_{max} = \frac{\lambda_0^2}{4\delta\lambda}, \quad (1.4)$$

where $\delta\lambda$ is the wavelength sampling interval. However in practice $\delta\lambda$ is obtained as a compound effect of sampling and the line-width of the swept source.

Swept source based OCT systems (as well as spectrometer based OCT systems) are generally regarded as superior to the time domain systems, as the information along the axial range is captured simultaneously. Furthermore, swept source based and

Fourier domain systems have been shown to produce higher quality images due to significantly better sensitivity [19].

1.2 Thesis statement and contributions

This thesis contributes to the field of optical coherence tomography by introducing several novel instruments and methods that improve the accuracy of collected data. Two main contributions can be singled out. First, this thesis proposes a new method for OCT data acquisition through several simultaneous independent imaging channels. Several possible instrument designs are suggested and three set-ups are implemented on the proof of concept level. Specifically, the set-ups for simultaneous *en-face* imaging at different depths, polarisation sensitive imaging and long range SS-OCT imaging are designed, implemented and tested.

The multiplexing method presented in the first method which allows several simultaneous degrees of freedom: (1) simultaneous polarisation sensitive measurements at different depths, (2) independent control of optical power in different channels, (3) free-space access to each beam in the reference arm, (4) stable high RF carrier for each channel.

Second major contribution of this thesis is a novel device for stabilised monitoring of live *Drosophila* larvae. A set-up based on a tracking method originally developed for retinal tracking by PSI Inc. is presented. This thesis introduces a novel design for an instrument for continuous monitoring of moving objects, which includes off-the-shelf electronic circuit for closed loop tracking. The design was implemented for continuous contactless monitoring of the heartbeat in a freely moving *Drosophila* larva. To the authors' knowledge, no other method allows such long term contactless monitoring in

freely moving animals.

1.3 Thesis summary

Medical imaging provides a wide spectrum of key tools in biomedical research, medical diagnostics, tissue monitoring and disease prevention. One of the modern imaging techniques extensively used for medical and biomedical imaging is OCT. OCT is an interferometric technique, which employs near-infrared light. OCT can provide high-resolution images of tissue, up to few millimetres deep, without the need for a biopsy and without the use of radioactive tracers or ionising radiation. Furthermore, different OCT modalities can provide functional imaging, revealing not only the structural information of a tissue but as well other properties such as its birefringence or the velocity information, the properties that can provide information for example about the polarisation properties of tissues and flow speeds. The work presented in this thesis focuses on the development of methods that facilitate the collection of accurate OCT data.

The thesis contains two main parts. A novel Bragg cell based multiplexing method, which enables simultaneous imaging in several parallel OCT channels is presented in the first part of the thesis. The part I contains: (1) a review of the state of the art multiplexing technologies; (2) a chapter on design considerations of our proposed multiplexing method and three chapters on experiments that explore how the multiplexer can be used to provide accurate data through simultaneous acquisition of data in several channels in (3) time domain OCT, (4) time domain polarisation sensitive OCT, (5) the sensitivity range can be extended in swept source based systems.

The second part of the thesis explores the optical tracking as a different way to counter

the movements of an object and produce consistent data. In this part, we review of the state of the art tracking methods, and we present a closed loop tracker based system for coherence gated Doppler monitoring of the *Drosophila melanogaster* larva heart.

Chapter 1 offers a general introduction to optical coherence tomography and coherence gated measurements as well as outlining the motivation of the thesis.

Chapter 2 positions the thesis contribution to the current state of the art, by presenting a review of recent multiplexing methods and strategies used in OCT.

Chapter 3 outlines the optical design considerations for building a Bragg cell based multiplexer. This chapter explains the reasoning behind the optical design solutions used in the experiments detailed in subsequent chapters. After exploring the theoretical limitations of the multiplexer, several solutions are presented how Bragg cell based multiplexer could be developed further to reduce its complexity, footprint and cost. Additionally, possible strategies for increasing the number of polarisation sensitive and polarisation insensitive channels are suggested. Finally, application-specific notes about tailoring the multiplexer design to achieve optimal performance are provided.

Chapter 4 presents the first experiment where a novel low-coherence interferometer configuration equipped with acousto-optic deflectors is used to simultaneously acquire eight time domain OCT *en face* images. The capabilities of the configuration presented are evaluated in terms of depth resolution, signal to noise ratio and crosstalk. Then the configuration is employed to demonstrate simultaneous *en face* OCT imaging at five different depths in a specimen of *Armadillidium vulgare*.

Chapter 5 presents a second experiment where a time-domain polarisation sensitive (PS) OCT configuration operating at 830 nm, is equipped with multichannel acousto-optic deflectors and single photodetectors. The system is used to simultaneously acquire interference information from multiple PS channels and measurement and imag-

ing of backscattered intensity to create both PS and polarisation insensitive images. This approach enables multiple channel imaging without the need to divide the object signal. Here, the system is employed in order to demonstrate PS imaging of a thermally damaged muscle tissue.

Chapter 6 presents a third experiment where a novel swept source OCT configuration is equipped with acousto-optic deflectors that can be used to simultaneously acquire multiple B-scans originating from different depths. The sensitivity range of the configuration is evaluated while acquiring four simultaneous B-scans. Longer than 17 mm OPD axial range, with a sensitivity variation of less than 2 dB is demonstrated. Then the configuration is employed to provide long range B-scan imaging by combining two simultaneous B-scans from a mouse head sample.

Chapter 7 presents a review of current object tracking and image stabilisation methods for improving the quality of OCT data.

Chapter 8 presents a novel instrument for biosciences, useful for studies of moving embryos. A dual sequential imaging/measurement channel is assembled via a closed-loop tracked scanning systems. The dual channel system can be operated either as a Doppler signal monitoring or as a fast 3D OCT imaging system. The system is demonstrated for characterising the cardiac dynamics of the *Drosophila melanogaster* larva. Closed loop tracking enables long term *in vivo* monitoring of the larvae heart with no need to anaesthetise or physically restrain the larva. Such an instrument can be used to measure subtle variations in the cardiac behaviour otherwise obscured by the Doppler frequency disturbances due to the body movement of the larvae.

Part I

Multiplexing

Chapter 2

Multiplexing in OCT

2.1 Introduction

One of the ways to improve the speed or functionality of OCT is to parallelise the imaging by using several imaging channels at the same time. This approach has been investigated since the early days of the OCT [119, 118]. Two approaches can be distinguished for implementing multichannel imaging in OCT – multiple object beam imaging and single object beam imaging, as depicted in Fig.(2.1).

The first group of strategies employ multiple spot imaging. Here, multiple foci on the object are created and, in effect, several interferometers are combined, to speed up the imaging. This is achieved by employing several beams to scan different areas on the sample or to perform the imaging under different conditions, i.e. the beams can be focused at different depths or they can be used for imaging of the same spot from the different angles. The multiple beams are created in the sample arm, where they are adjusted to image either the same area of the target at various angles or multiple areas at the same angle. Multiple spot imaging based multiplexing techniques are commonly

Multiplexing strategies

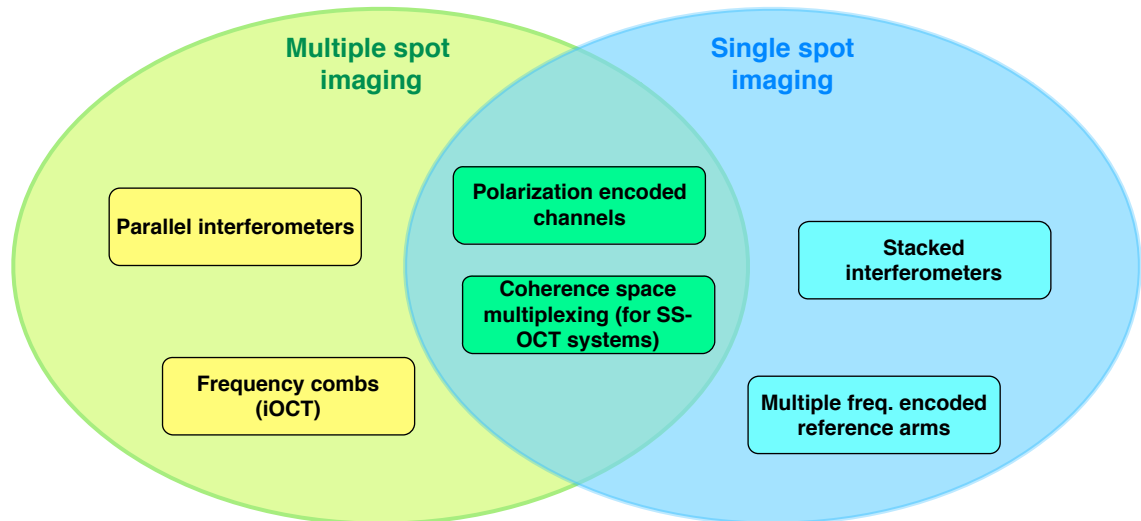


Figure 2.1: Summary of the various multiplexing strategies employed in optical coherence tomography.

employed for (A) speeding up the acquisition of 3D volumes [121, 155, 166], (B) Doppler imaging [10, 60], (C) depth of field improvement for imaging of the whole eye [27, 30] and (D) de-speckling [55, 58].

The second group of strategies employs single object beam imaging. Here, a single beam is scanned over a target, or the multiple beams are created and combined in a way that all the beams are perfectly overlapped, so during the imaging, only a single focal spot is created on the sample. Multiplexed single object beam imaging systems can be employed for either for (A) polarisation sensitive imaging [4], (B) increasing the imaging speed and efficiency of TD-OCT systems [128], and (C) extending the sensitivity range in SS-OCT systems [13].

There is a strong similarity in the optical design of set-ups for time domain and swept source based OCT systems. Therefore this chapter will review the multiplexing strategies that can be applied to such systems

2.2 Multiple object beam imaging based multiplexing strategies

One of the earliest implementations of multiplexing in OCT was the use of multiple interferometers combined together. In some of the most straightforward applications of this method, two interferometers, each with separate balanced photo-detectors, were combined to achieve fast dual spot swept source OCT [121]. This approach delivers increased image acquisition speed, at the expense of significantly increased cost and complexity of the imaging set-up. The maximum number of imaging channels in parallel interferometer based OCT imaging, is limited by the experimental cost of building complex interferometer arrays. Set-ups employing four parallel interferometers, such as the one depicted in Fig.(2.2a), were demonstrated to work equally well [155].

A similar idea of using two parallel interferometer configuration implemented using fibre arrays was used to perform bidirectional dual beam Doppler OCT [10]. Here a rotating Dove prism was used to illuminate the sample at two different angles allowing for measurement of the true flow velocity at arbitrary vessel orientations Fig.(2.2b). Balanced photo-detection was implemented for each channel separately, at 100 kHz sampling rate.

Other multiplexing strategies include separating two orthogonally polarised channels by their polarisation state - this approach is typically exploited in polarisation sensitive systems, in single spot imaging based multiplexing set-ups. However, polarisation multiplexing can be employed not only for PS-OCT, but in other imaging modalities as well. In a dual beam optical coherence angiography set-up (Fig.(2.3a)), polarisation multiplexing was employed to create two-dimensional choroidal vasculature maps [60]. In this configuration, a polarisation beam splitter is used to create two orthogonally polarised imaging beams with adjustable spatial (or angular) separation.

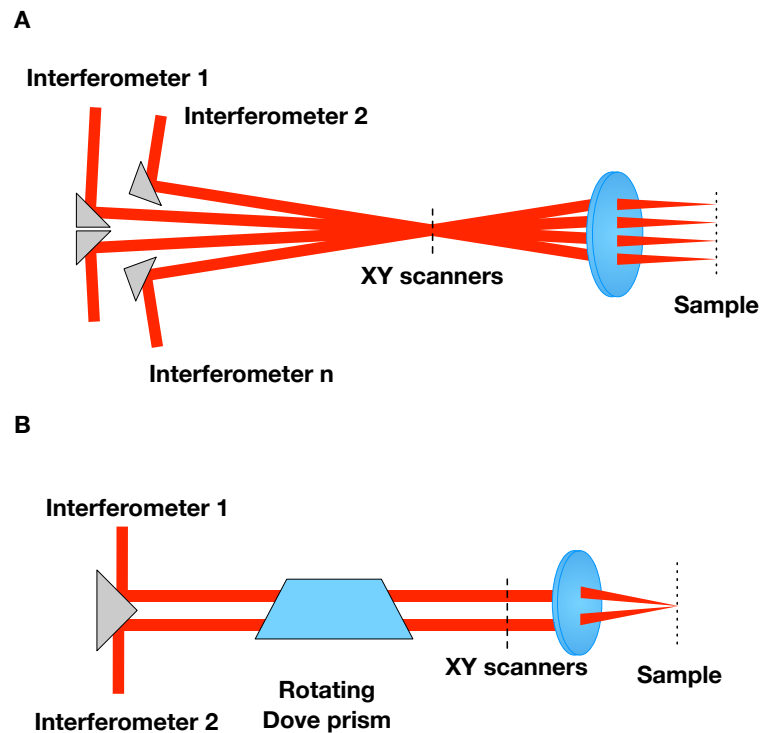


Figure 2.2: Multiple interferometer based multiplexing strategies for multiple object beam imaging OCT.

Separate balanced photo-detectors were used to detect the interference from each channel. The trade-off between the number of vessels that can be visualised and their contrast was studied.

A potential issue that can potentially deteriorate the image quality in the systems where different channels are encoded by their polarisation state, is the crosstalk between the channels. This can occur when imaging birefringent samples, that can change the polarisation state in different channels.

Multiple object beam imaging was shown to work well in applications, when each beam was optimised to do the imaging under different optical conditions. An early example of this approach employed two separate interferometers, operating with orthogonally oriented linear polarisation states. This was demonstrated for imaging,

optimised for different surfaces in the anterior segment of the eye [167] as well as for the whole eye imaging [27]. More recently, a set-up using coherence revival-based heterodyne swept source optical coherence tomography was demonstrated, employing an optical delay between two orthogonal polarisation states in the object arm light [30]. The separation of the interference signal resulting from the two orthogonal polarisation states in different RF bands of the photo-detected signal was implemented by using an optical delay. Just before entering the eye, the two signals were separated and then recombined with polarisation beam splitters. Optical elements are then placed between beamsplitters to ensure that one beam is optimised for anterior chamber imaging and the other channel provides high resolution retinal imaging (Fig.(2.3b)). The coherence revival technique [31] is used to extend the axial range of the overall system to cover the whole eye. The detection in this set-up is performed using a single balanced photo-detector.

A similar goal of covering a long axial range is achieved in a VCSEL based SS-OCT system [166]. The light from the 100 kHz source was divided into eight sub beams using a fibre coupler in the reference arm and then different delays were introduced into each beam. The resulting imaging channels are then detected within different frequency intervals in the RF spectrum. The performance of the set-up was demonstrated by imaging *Drosophila* larva *in vivo*. A sensitivity of 94.6 dB and a roll-off of < 2 dB over ~ 30 mm imaging axial range were measured for a single channel.

A different strategy is employed in an interlaced OCT (iOCT) set-up. This relies on splitting the continuous spectrum from the swept source into several frequency combs, propagating at different angles. In this way, several locations in the sample can be imaged simultaneously. The optical frequency combs are created with a *virtually imaged phase array* [139] and the number of resulting channels depends on the design parameters. It was reported that illumination with frequency combs does not deteriorate the

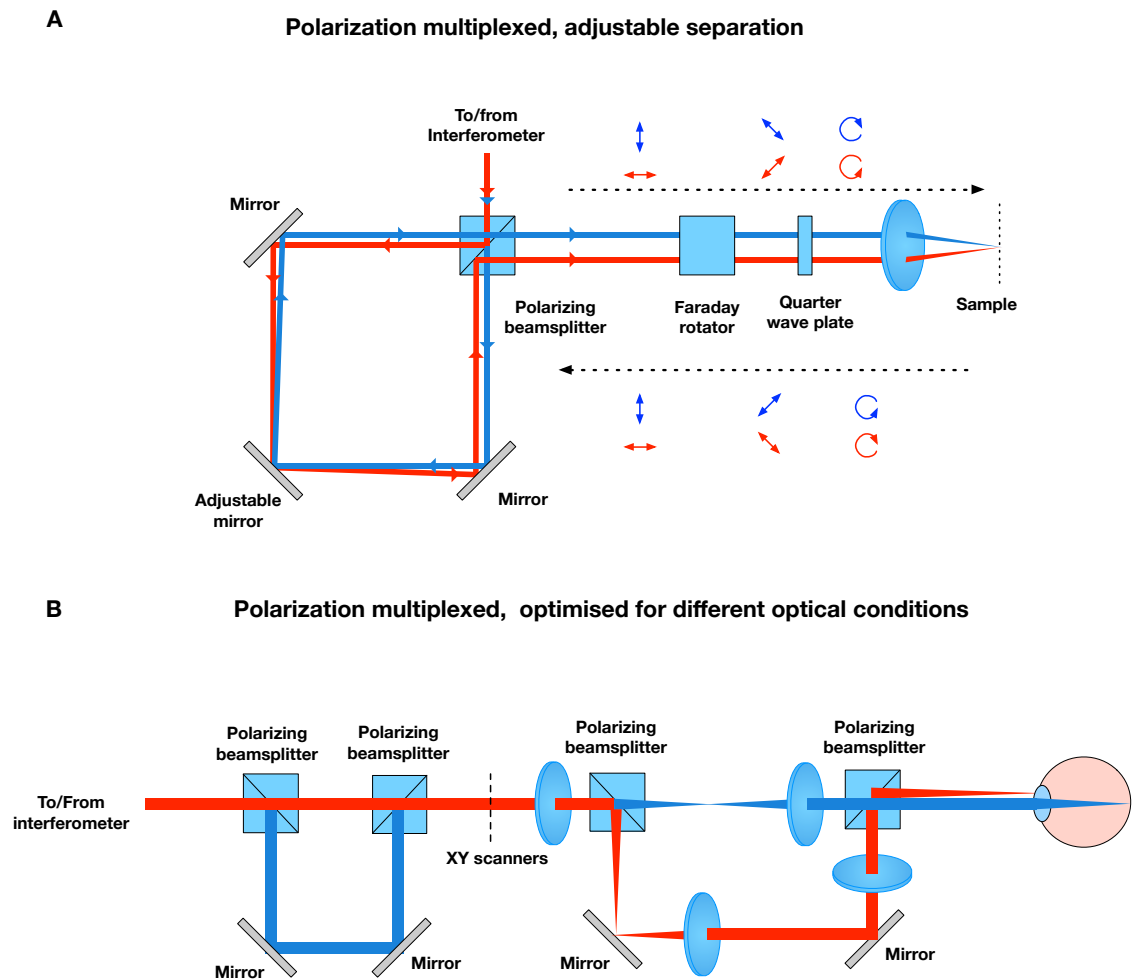


Figure 2.3: Polarisation multiplexed OCT.

image quality in terms of resolution, as the same spectral range is still used, however it reduces the sensitivity range [9]. The image acquisition speed was shown to increase up to 12 times, depending on the number of imaging channels used [77].

2.3 Single object beam imaging based multiplexing strategies

A vast majority of single object beam imaging based OCT imaging techniques employ frequency shifts to differentiate between different channels. The design of early set-ups usually employed multiple stacked interferometers, with a frequency shift inducing element (vibrating mirror, acousto-optic device) in each of the reference arms [119, 120]. This approach later evolved into configurations where a reference arm in the interferometer is divided into several sub-arms, encoded at different frequencies. The benefit of dividing and recombining the reference arm light is that it is compatible with fibre based OCT systems and it only requires a single balanced photo-detector for simultaneous detection of several OCT imaging channels. This approach was successfully demonstrated to work with both time domain and swept source based systems. There are variety of multiplexing set-ups that are based on frequency encoding. One of the first configurations employed an integrated optical modulator, where two *en face* OCT images were generated simultaneously [120], as depicted in Fig.(2.4b). A similar set-up [28] was employed to perform frequency multiplexed OCT with two polarisation maintaining channels [4].

Another strategy for creating multiple OCT channels employs a frequency shifter and recirculation loops (Fig.(2.4a)). In this way, a new channel is created during each recirculation, when a portion of the light repeats the same loop. Imaging at five different depths in a *Drosophila* sample was demonstrated using recirculation loops [101]. Later, the same approach was also used to increase the imaging range for the swept source based OCT [13], where the frequency shift and optical delay from channel to channel were selected in such a way that the sensitivity increase of each subsequent channel compensated for the sensitivity drop in a previous channel. A similar

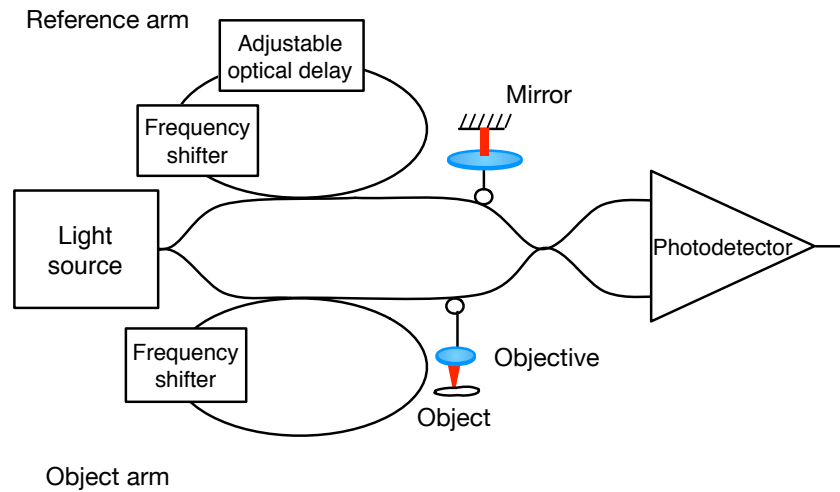
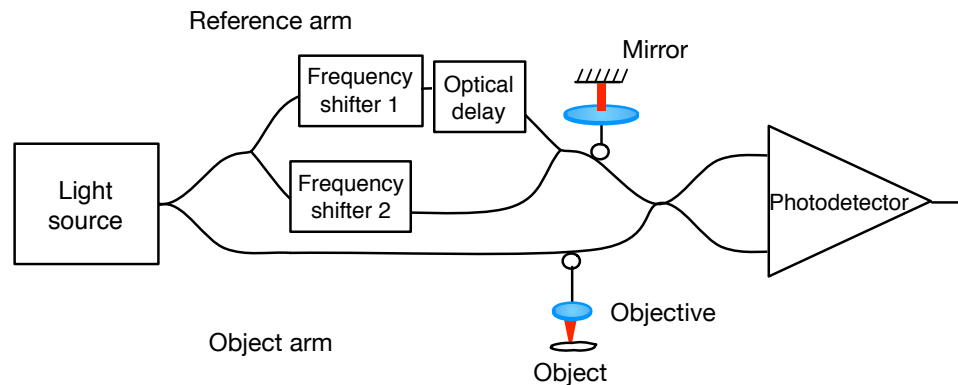
A Recirculation loop based OCT**B** Multiple frequency shifters based OCT

Figure 2.4: Two frequency shifting based OCT Strategies. Left: recirculation loop based OCT. Right: OCT with multiple frequency shifted reference arms. The systems are shown implemented in fibre, however they are compatible with free space configurations as well.

set-up employing active recirculation loops was designed for polarisation maintaining multiple-depth *en face* OCT [128].

Coherence domain multiplexing was employed for scattering angle diverse SS-OCT, the technique involves division of the object light via a glass ring centred on the object

beam axis to introduce an optical delay into the outer annulus of the object beam [153]. In this way, the light, scattered at different angles was detected on the different bands in the photo-detected spectrum.

Another multiplexing strategy is based on separating two orthogonally polarised channels by their polarisation state. This approach was successfully exploited with polarisation sensitive systems, where two channels are created in the reference arm [66]. However, polarisation multiplexed systems are commonly limited to two orthogonally polarised channels that require separate photo detectors.

2.4 Future outlook

Examples of multiplexing in optical coherence tomography have been demonstrated in a number of implementations and applications. There are still many technical challenges to be solved before efficient multiplexing methods could be applied in commercial OCT systems.

There are three main areas, where a multiplexer can enhance the OCT system: (A) the extended sensitivity range swept source based systems; (B) high speed imaging with parallel beams or simultaneous time domain imaging at different depths; and (C) functional imaging where each channel is used to perform the imaging under different conditions (i.e. polarisation measurement, de-speckling, Doppler imaging).

As the main application of optical coherence tomography is the imaging of biological specimens, the photo toxicity is an important issue. Therefore the desire for an efficient use of the object light favours multiplexing strategies, which only rely on the division of the light in the reference arm. In OCT, especially in biomedical imaging, the majority of optical power is commonly diverted to the reference arm. However,

commonly the power in the reference arm has to be attenuated to avoid saturation of photodetectors or reduce noise. Hence creation of several parallel reference arms may not require a proportional increase of total optical power. However more power is required for multiplexed OCT systems. As a result, the multiplexing approaches can greatly benefit from the development of high output power lasers [80] and advanced low noise optical amplifiers.

Finally, the techniques that rely on multiplexing in frequency, or in the coherence space can be severely restricted by the speed of data acquisition cards. This requires more research on the optimisation of allocation of frequency bands and advanced design of digitiser cards.

Chapter 3

Optical design considerations for a novel Bragg cell based frequency domain multiplexer for optical coherence tomography

3.1 Introduction

There is an interest in OCT of speeding up the acquisition to cope with the motion artefacts caused by sample movements or by the environment in biomedical settings [2, 42], particularly in retinal imaging [71]. In industrial applications, fast image acquisition is required for inspecting a large quantity of pieces in a short period of time as well as for imaging multiple areas of interest at the same time [157, 82]. In the previous chapter we have reviewed a variety of methods that were designed to speed up the acquisition of OCT data and in consequence provide data more tolerant to move-

ment, which accurately represent an object under investigation. The majority of these methods suffered from an inefficient use of the light, backscattered from the object. Single spot imaging methods required division of both the reference and object paths into several channels differentiated either by a frequency shift or by the polarisation state. Therefore, the irradiation of the sample had to be increased proportionally to compensate for the power division amongst parallel channels. Increase in power may cause photo toxicity in biomedical applications. Additionally there were several other recurring limitations such as inability to control the light levels, polarisation states in individual channels, or only few available imaging channels.

The configurations that employ versions of cascaded Mach-Zehnder interferometers in conjunction with frequency shifters to create multiple path length differences associated with unique frequencies [119, 59] present several disadvantages: (i) different states of polarisation cannot be associated with unique carrier frequencies; (ii) in integrated formats (such as in [59]), optical delays cannot be easily adjusted; (iii) after the wave passes through a train of cascaded interferometers, the intensity in channels corresponding to different carrier frequencies present unequal optical intensities. As each phase element introduces a separate frequency shift, the configuration is complex and not reconfigurable in terms of functionality.

Configurations of optical delay lines devised for telecommunications that employ acousto-optic deflectors to scan and de-scan the laser beam to achieve different delays [124] present several disadvantages when employed in OCT configurations: (i) employing a single frequency with spectral scanning in time to achieve different delays, the procedure is time consuming; (ii) different polarisation states cannot be associated with unique carrier frequencies.

In order to speed up the acquisition of images in time domain (TD)-OCT, a method and systems are presented in [113, 101], where an active recirculating loop is placed in

each interferometer arm together with a frequency shifter. The two frequency shifters are driven at different frequencies so as to encode signals from successive depths in the object on the frequency difference between the two frequencies. The depth positions are separated by the differential optical path difference of the two recirculating loops. To alleviate the attenuation at each round trip in the recirculator, optical amplification is used. Despite the employment of amplifiers in the secondary loops to compensate for losses at the expense of boosted noise. Only up to twenty recirculations could be produced and good signal to noise ratio images from five depths only could be obtained [101]. Two major causes for failure to achieve more channels are due to the amplified spontaneous emission (ASE) built up in the secondary loops and also owing to polarisation mismatch.

Configurations presented in the patent by Podoleanu [113] presents the following disadvantages: (1) From a round trip to the next, the interference signal decays by more than 4 dB, leading to decay from channel to channel in depth to the same extent. (2) Multiple states of polarisation could not be associated with multiple roundtrips along the multiple paths. (3) The depth is encoded on the frequency shift imprinted by the number of wave passages through frequency shifters. This limited the applicability of the configuration. (4) The object in OCT imaging is a multiple reflector, and the recirculating loop in the object arm creates multiple replicas. Out of the multiple replicas sent to the multilayer object, only one of these replicas is practically used to produce an image from a certain depth in the object. It appears to be inappropriate to split the object arm and send multiple replicas to a target that will return multiple replicas itself. (5) Optical amplification introduces ASE noise. Another problem is that of decay of sensitivity with depth in spectral OCT. A multiple path configuration with secondary loops in each interferometer arm [13] could reduce the decay with depth. However, the method presents the disadvantage of ASE and cost, and while

the method can enlarge the axial range of spectral OCT by 20-100 times the axial range in a conventional OCT configuration. In practice, extension by a much smaller factor of 2-3 of the axial range only is sufficient.

The designs presented in the rest of this chapter therefore seek to overcome the above mentioned disadvantages, by providing novel enhanced configurations and methods of operation. The novel features incorporated herewith can lead to better uniformity between at least some of the channels corresponding to different depths, better control of polarisation for at least a limited number of channels and better efficiency in using the signal. The acousto-optic cell based designs ensures that from within at least some adjacent layers in depth, the strength of signal is similar and strong. In addition, some of the designs are reconfigurable, allowing different functionality to be achieved with minimum changes.

Simultaneous collection of images for multiple depth interrogation, multiple polarisation interrogation, structured illumination can be achieved with more compact, lower cost, lower noise designs. In the spectral interferometry configurations proposed, constant decay with depth or lower attenuation with depth is obtained by using a limited number of parallel channels which make such designs more compact and reduce the cost of a set-up. In a majority of designs presented here, the depth is encoded on the pulsation frequency of the interference photodetected signal. By providing extra means to encode the depth, where the frequency shifters are placed outside the optical rings, more compact rings and lower costs configurations are possible. In all the previous approaches mentioned above, frequency shifters are driven at fixed frequencies. This limited the functionality of the interferometers.

This chapter will present and explore a multiplexer configuration that employs acousto-optic crystals that are excited by multiple frequencies simultaneously to create and later recombine a fan of first-order diffracted beams. The frequencies of the signals

applied are can be selected independently, which allows reduced cross talk. The adjacent excitation frequency spacing in the radio frequency (RF) spectrum possibilities will be evaluated. This chapter will be limited to a theoretical discussion only of several possible multiplexer designs. The chapter will focus on explaining the considerations that led to the design of the experiments presented in following chapters.

3.2 Designing a multiplexer for a multichannel OCT system

3.2.1 Frequency domain multiplexing based OCT

The basic design of a multiplexer proposed in this thesis includes two Bragg cells (or acousto-optic deflectors, AOD) enclosing two lenses positioned at a $4f$ arrangement (where f is a focal length of a lens) and a multiple optical delay element positioned at the focal distance in between two lenses, at the Fourier transform plane. Both Bragg cells are driven by a single digital frequency synthesizer, capable of simultaneously create a number n of frequencies F_n . A set of different frequency signals applied to the first Bragg cell generates multiple phase gratings, each of which diffracts an incident light and shifts the frequency of the first order diffracted beam by f_n . After exiting the first AOD1, the higher order of diffraction beams are spatially rejected using a conveniently placed pinhole. After passing the lenses and phase control element, a fan of first order diffracted beams converges on the AOD2 as depicted in Fig.(3.1). While propagating through the AOD2, each beam undergoes the same set of diffraction events as in the AOD1, as the same set of RF frequency values are used for the driving signal of the AOD2.

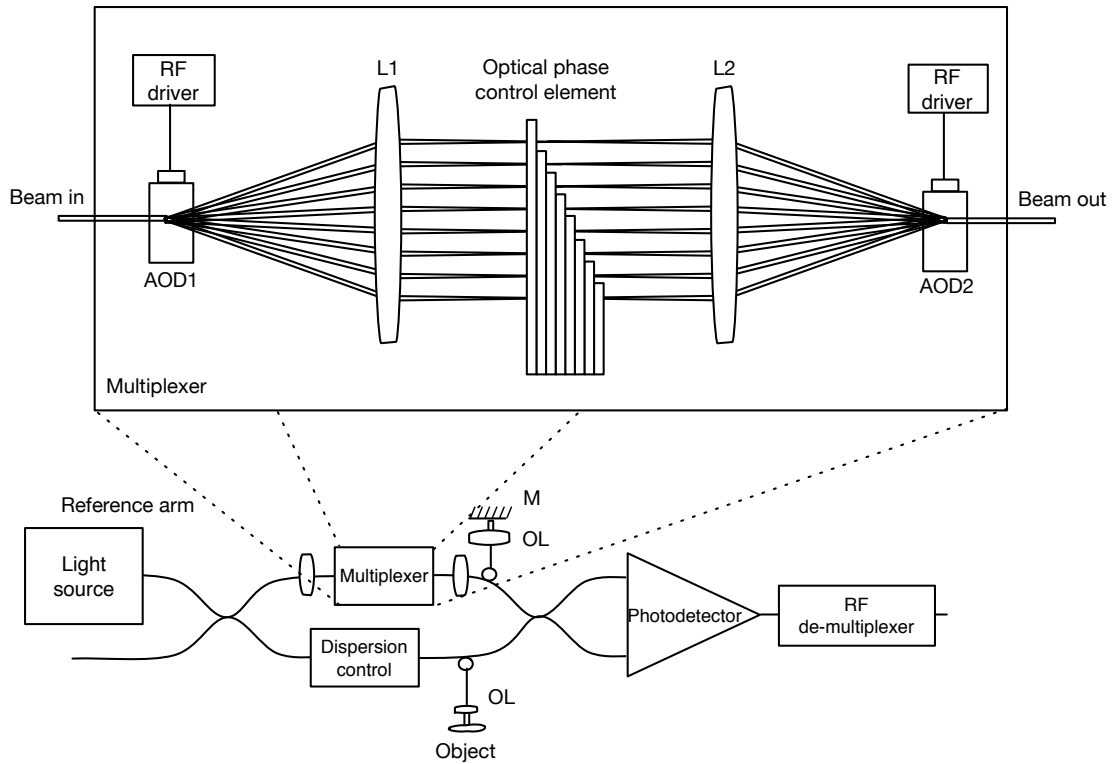


Figure 3.1: Basic layout of OCT system employing a multiplexer as detailed by the expanded view above. M: reference mirror; OL: objective lens.

Beams that undergo two diffraction events, caused by signals of the same frequency, i.e. f_1, f_1 and f_2, f_2 , spatially overlap. They emerge from the AOD2 along the same angle of propagation. In other words, the set of beams, each diffracted twice can be treated as a single beam and injected into a single mode fibre. The beams that are diffracted by non-matching frequency pairs i.e. f_1 and f_2 , f_3 and f_8 , etc., have different angles and can be filtered out spatially with a conveniently positioned pinhole.

A multiplexer included in the system, creates four degrees of freedom: (1) a carrier frequency can be independently selected for each channel allowing mirror term free spectral OCT imaging as well as elimination of low frequency noise. Spatially non overlapping beams are created in the multiplexer, enabling insertion of phase control elements which in turn allow independent control of both (2) OPD and (3) polarisation

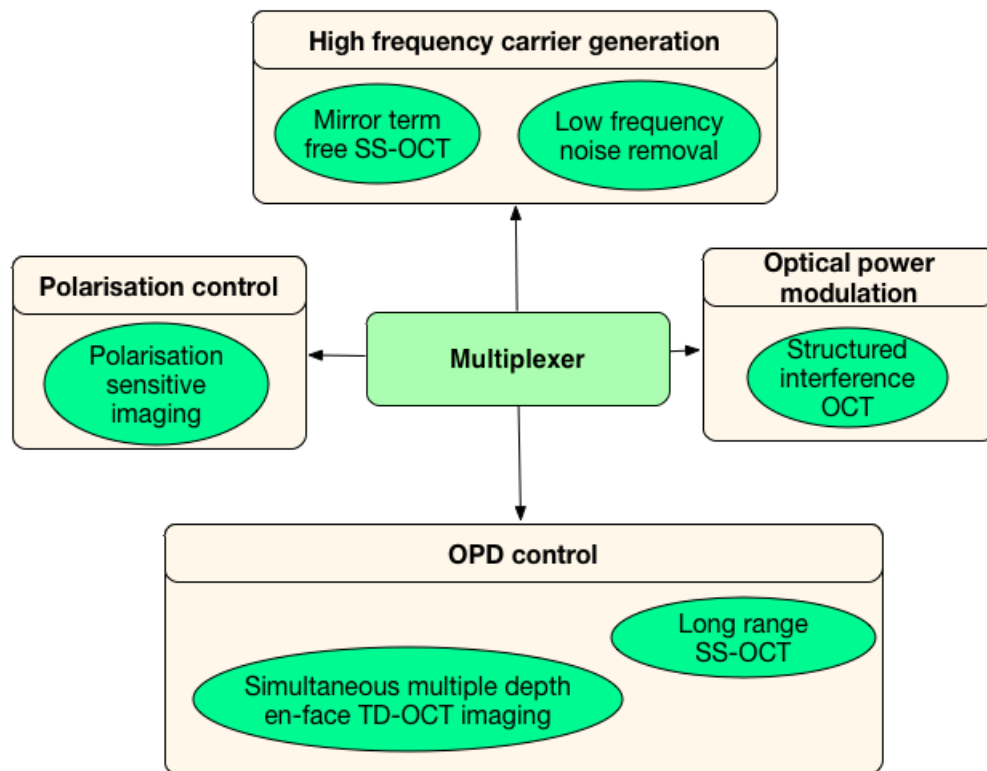


Figure 3.2: Several multiplexer-enabled imaging modalities.

for each channel. Lastly, the intensity of each phase grating in the Bragg cell can be easily manipulated by adjusting the intensity of the RF signal, which in turn (4) controls the amount of light being diffracted into each channel, thus enabling the structured interference techniques.

Different designs for the multiplexer can be used in conjunction with an OCT system to achieve a variety of imaging modalities (as shown in Fig.(3.2)). In the subsequent sections we will explore avenues to optimise the multiplexer for different applications requiring various optical phase control elements (polarisation and OPD control). We will also study the compatibility of a multiplexer with a time domain and swept source based OCT systems. Additionally, we will consider the choice of carrier frequency values and the ability to control the amount of light in individual channels.

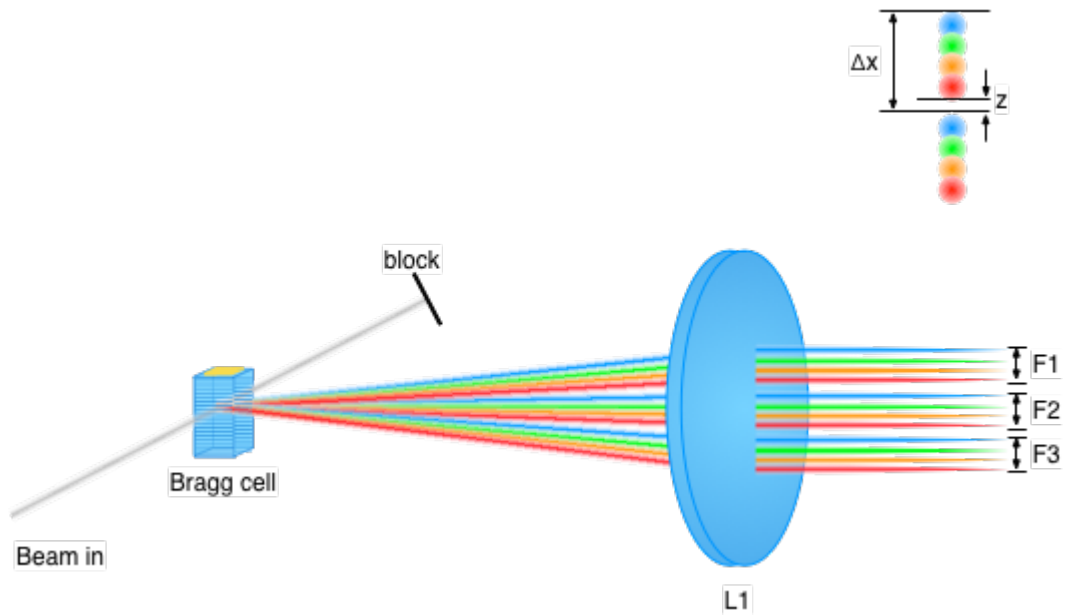


Figure 3.3: Illustration of a Bragg cell operating at three frequencies where the spectrum of the optical source is comprised of four distinct wavelengths, as illustrated by four different colors. F_1 , F_2 and F_3 are the distinct frequencies used to drive different channels, z is the gap from one channel to the next and Δx is the channel-to-channel spatial separation in the Fourier plane after the first lens.

3.2.2 Angular overlap of adjacent channels

To enable the insertion of phase control elements into each beam of the multiplexer, we need to ensure that the beams after diffraction do not overlap spatially. This condition is automatically satisfied for different carriers if the spectrum of the optical source has an infinitesimally small optical bandwidth. For OCT imaging however, it is commonly desirable to employ broadband light sources or wideband tunable lasers, that enable high axial resolution. Due to Bragg's law, different wavelengths are diffracted at different angles by the AODs, that leads to spatial extension of the beam footprint, as shown in Fig.(3.3).

The phase grating created by the acoustic wave in the acousto-optic crystal. According to Eq.(3.1), diffracts the incident beam in the first order diffraction at an angle:

$$\theta_D = \frac{\lambda f}{\nu}, \quad (3.1)$$

where λ is the wavelength, f is the frequency of the RF signal applied to the crystal and ν is the speed of sound in the acousto-optic crystal. Suppose that the frequencies of the signals used for excitation are spaced evenly at a step of Δf . If this is not large enough, beams diffracted by the two highest frequencies in the set, $f_{max} - \Delta f$ and f_{max} , will start overlapping. For simplicity, the beam diameter will be considered infinitesimally small. When the shortest wavelength of the higher frequency f_{max} beam reaches the same angle as the longest wavelength of the lower frequency $f_{max} - \Delta f$ beam, then the two adjacent diffracted beams will start overlapping. This condition can be written as:

$$\frac{f_{max}(\lambda_C - \Delta\lambda/2)}{\nu} = \frac{(f_{max} - \Delta f)(\lambda_C + \Delta\lambda/2)}{\nu}, \quad (3.2)$$

where λ_C is the central wavelength and $\Delta\lambda$ is an optical bandwidth of the optical source.

Eq.(3.2) can be used to determine the minimum RF step, Δf_{min} , to secure non-overlapping beams even in the set of the two largest frequencies:

$$\Delta f > f_{max} \cdot \left(1 - \frac{\lambda_C - \Delta\lambda/2}{\lambda_C + \Delta\lambda/2}\right), \quad (3.3)$$

We have calculated the overlap condition, Eq.(3.3), versus $\Delta\lambda$ for three most widespread wavelengths currently used for OCT imaging: 830 nm, 1050 nm and 1300 nm, and considering a typical modulator driving frequency $f_{max} = 100$ MHz. The results of such calculations are used to draw the graphs in Fig.(3.4).

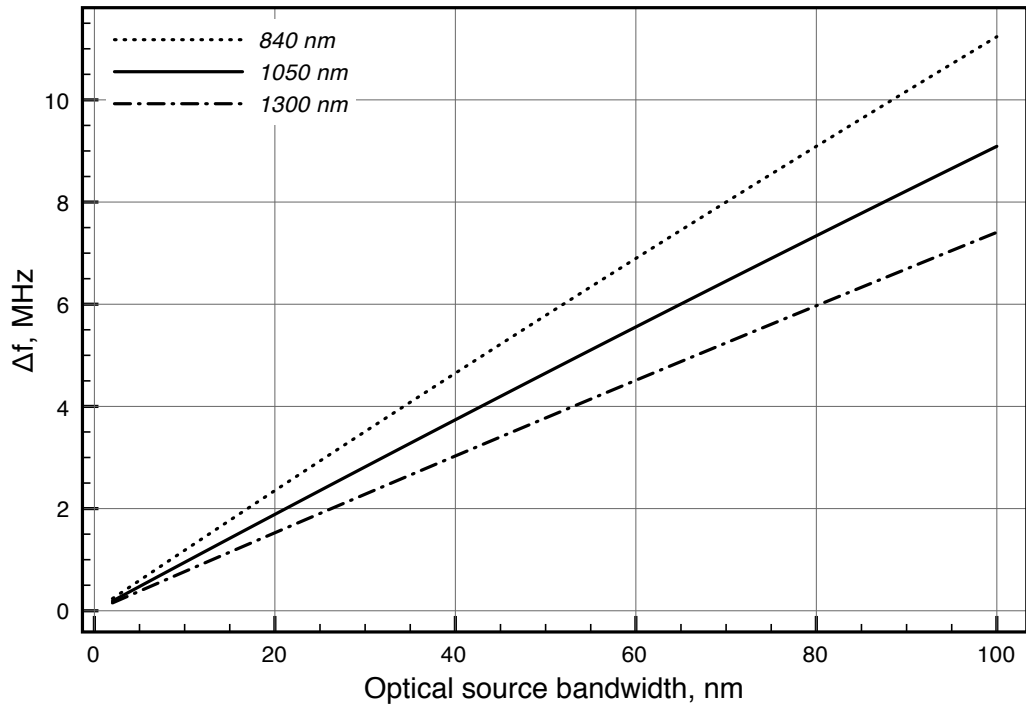


Figure 3.4: Angular overlap threshold for three cases of 830 nm, 1050 nm and 1300 nm for TeO_2 Bragg cell, limited by a driving signal of 100 MHz frequency.

As the optical bandwidth $\Delta\lambda$ is determined by the source or axial resolution requirement, the step between adjacent frequencies Δf should be minimised in order to reduce the necessary photodetector bandwidth, proportional with the detection noise.

3.2.3 Spatial overlap of adjacent channels

Figure (3.5) illustrates a multiplexer using a thick multiple phase control elements, of thickness D . From the initial beam of diameter p , several beams are diffracted by the Bragg cell. Inter-channel crosstalk may occur when light from more than one channel leaks through any given element in the multiple phase control element. To prevent such situation, the full thickness D of a multiple phase control element and the convergence of the individual beams, each of diameter p , must be considered.

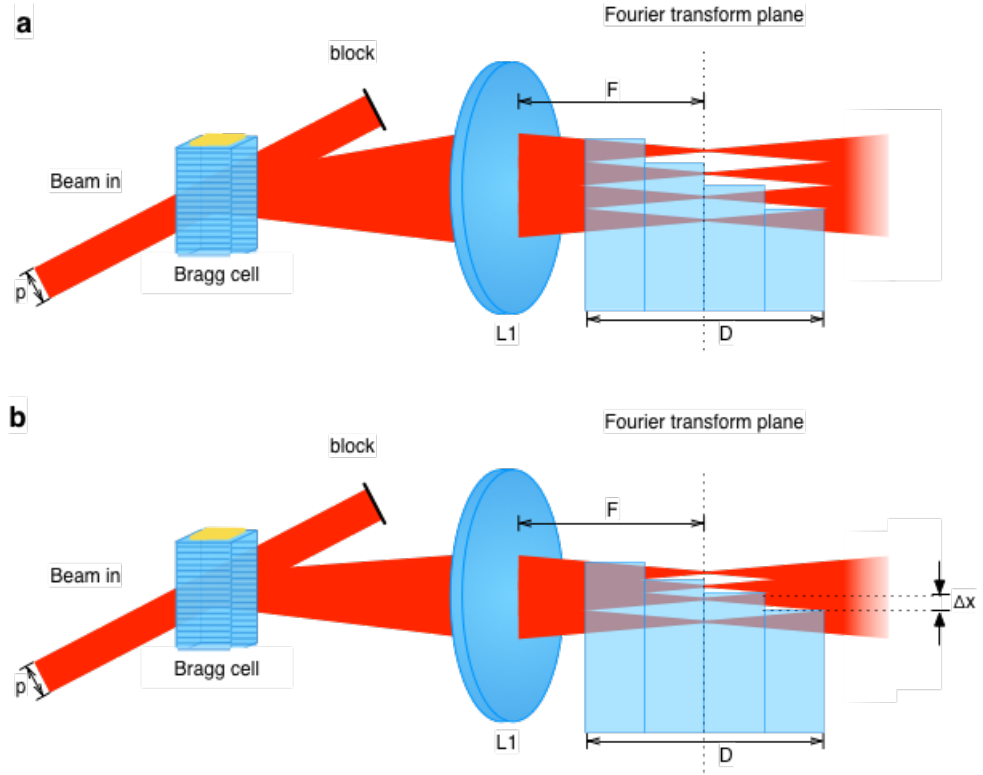


Figure 3.5: Illustration of non-overlapping beams with thick delay elements. (a) non-optimised regular period frequency distribution and (b) optimised frequency distribution in the multiplexer.

Satisfying angular overlap condition ensures that the beams, created from the initial collimated beam launched into the multiplexer, do not overlap spatially in the Fourier transform plane, which is located at the focal distance from the first lens. By using simple trigonometry, and Eq.(3.1) we can find the diameter of a clear aperture Δx needed for each beam, when lens with a focal length f is used.

$$\Delta x(p) = f \left(\tan \frac{(\lambda_0 + \frac{\Delta\lambda}{2}) f_p}{\nu} - \tan \frac{(\lambda_0 - \frac{\Delta\lambda}{2}) f_p}{\nu} \right) + \frac{p \cdot D}{2f}, \quad (3.4)$$

where p is the diameter of a collimated beam that was launched into the multiplexer and D is the full optical thickness of a multiple phase control element centred around the Fourier transform plane of the first lens depicted in Fig.(3.5a).

The waist of converging/diverging beam increases proportionally with the step facet distance from the Fourier plane. Therefore, for thicker delay elements, by increasing the step Δf between the frequencies of adjacent channels, from the central beam to periphery, more clearance between one beam to the next is created. The footprint of the system can be further reduced by selecting non-uniform distribution of frequencies over the set of channels as illustrated in Fig.(3.5a). The maximum optical bandwidth accepted in both **a** and **b** cases remains the same.

3.2.4 Multiplexer optical power budget

There are three main sources of power loss in the multiplexer: (1) creation of spurious beams due to intermodulation [44], (2) diffraction efficiency of Bragg cells and (3) recombination losses. The diffraction efficiency E of typical TeO_2 cells (*Gooch and Housego 46080-1-.85-LTD*) when operated under optimal conditions is $E \sim 60\%$. The amount of light in the first order of diffraction is maximised when the incident light is linearly polarised, with polarisation orientation perpendicular to the acoustic propagation axis. If random polarisation is used, the diffraction efficiency will be reduced by approximately 10% [135]. Additionally, the highest amount of light is diffracted into the first order beam, when the incident beam is launched through the crystal at the Bragg angle, however when more than one frequency is used to excite the acousto-optic crystal, different periodicity gratings require different angles. In the case when multiple frequencies are used, the angle is optimised for the mid-frequency and losses occur for the extreme frequencies.

The recombination losses occur due to the fact that only the beams diffracted by the conjugate frequency pairs are recombined, i.e. $(F1; F1$ and $F2; F2)$. For a system, operating with n channels, total recombination efficiency can be roughly estimated

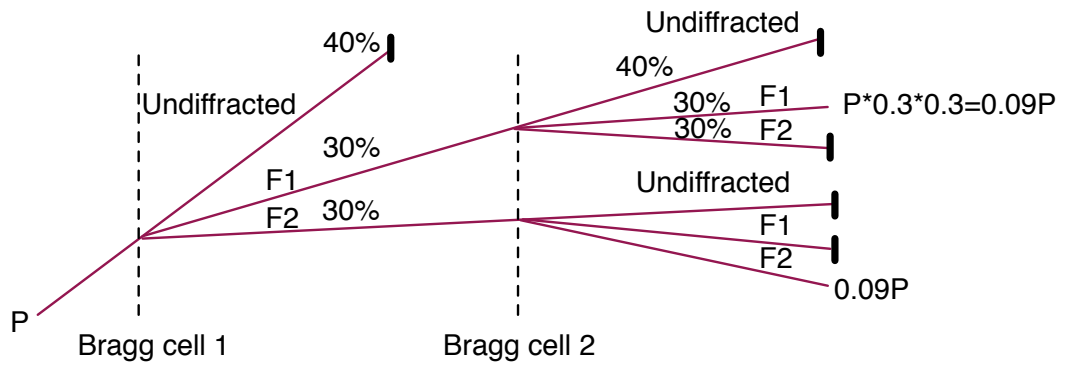


Figure 3.6: Diagram illustrating the distribution of optical power in the multiplexer operated with two driving signals of different frequency. P denotes the incident optical power. F_1 and F_2 indicate the respective optical power of the diffracted beams in the channels 1 and 2.

using formula $(E/n)^2$, where E is diffraction efficiency and n is the numbers of simultaneously applied signals. An example of a system operating with $n = 2$ channels and a diffraction efficiency $E = 60\%$ is depicted in Fig.(3.6). Further studies are necessary to estimate the impact of spurious frequency generation as the losses due to spurious frequencies depend on the RF power used to drive the crystals and on the number of simultaneous channels.

3.2.5 Operation in reflection

Good light use efficiency is achieved by a multiplexer design, which includes a pair of Bragg cells and two lenses in a $4f$ configuration (Fig.(3.7a)). However, on the expense of higher optical power losses (as explained later in the section), the footprint and cost of the multiplexer can be reduced by using a single Bragg cell only, employed twice for both creating and recombining the beams, as shown in Fig.(3.7b) and Fig.(3.6d). In this way, the RF shift is still maintained for different channels.

For multiplexer designs where an optical phase control element is used to modify OPD only, a solution which employs only one Bragg cell is depicted in Fig.(3.7b). Here, the

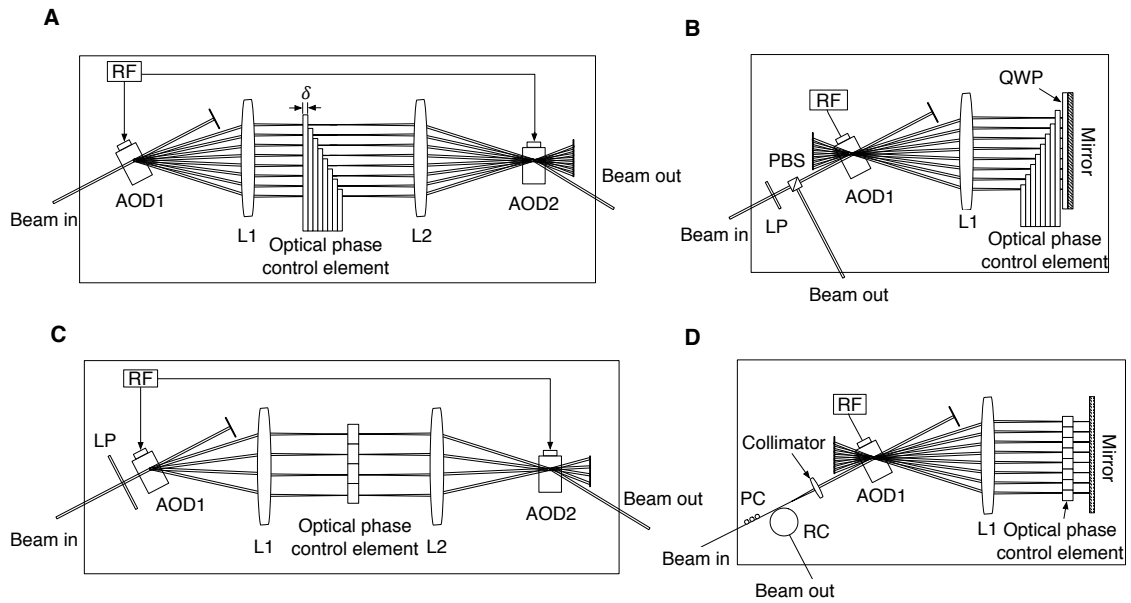


Figure 3.7: Proposed multiplexer set-up designs for interrogating: (A) OPD in transmission; (B) OPD in reflection; (C) polarisation in transmission (D) polarisation in reflection.

linear polarisation state of the beam is oriented by a linear polariser LP. The beam then passes polarisation beam splitter PBS and a fan of beams is diffracted as it passes through AODM1. Each diffracted beam then passes through a different zone in the phase control element and via a quarter wave plate (QWP), rotated at 45 degrees, then each channel is reflected from a mirror back up to the AODM1. Dual pass through the QWP, rotates the initial linear polarisation by 90 degrees, so the recombined beam can be efficiently reflected by PBS. The dual pass through the same Bragg cell imparts the same frequency shifts for different channels as in the transmission design (Fig.(3.7a)) so there is no difference in detection techniques required to de-multiplex and record the signal from different channel.

For the designs where the phase control element is used to control the polarisation state as well as the OPD, the QWP is eliminated and PBS is replaced by either a circulator RC (as depicted in Fig.(3.7d)) or a polarisation insensitive beam splitter. For

these configurations, the efficiency is less than in Fig.(3.7a), Fig.(3.7b) or Fig.(3.7c).

3.2.6 Channel quantity limitation

The possible number of channels in the multiplexer is fundamentally limited by several factors. The larger the deviation of the angle of incidence from the Bragg angle, the lower the diffraction efficiency. The Bragg angle of incidence depends on the grating periodicity. When several RF signals are applied to the Bragg cell, the optimal angle of incident beam is different for each grating, so a compromise must be found where the Bragg angle is optimised for a central frequency and the light is diffracted less efficiently for the outer channels.

The number of channels could be increased by integrating a multiplexer into a recirculation loop, as suggested in [114].

3.3 Application-related notes and discussion

3.3.1 Time domain *en face* multiple depth OCT

The multiplexer can be used for simultaneous imaging at different depths in a time domain OCT set-up. For this purpose a step-like phase control element is used to impart incrementally higher path lengths onto each subsequent channel. The main advantage of frequency multiplexed TD-OCT imaging is the possibility to perform simultaneous *en face* imaging at different depths of interest. Simultaneous imaging gives the confidence that even if the sample is subject to movement, the features from one frame to the next appear stationary due to the fact that all frames are simultaneously acquired. Independent control of light levels in different channels allows partial compensation of

sensitivity loss due to absorption in the sample and reduced light collection efficiency along the depth, thus potentially increasing the dynamic range of images.

3.3.2 Long range SS-OCT

The multiplexer can be used to perform different functionality for a long range swept source based OCT. Here optical path delays are introduced in several channels to capture different axial intervals in the sample using different channels. The images obtained from different channels can then be combined into a single image to compensate the drop in sensitivity also known as sensitivity “roll-off” [113]. Long range SS-OCT can be realised in two ways: (i) the carriers can be spaced at high RF intervals to ensure non-overlapping sensitivity ranges and then the images from different channels can be combined computationally to produce a long range image and (ii) setting the carrier frequencies and the differential delay in such a way that the sensitivity of the next channel would start increasing at the point where the previous channel begins to lose it [13]. In this way the addition of multiple channels takes place in the RF spectrum directly to produce the long sensitivity range B-Scan image.

Another significant benefit of using a multiplexer in conjunction with SS-OCT lies in the fact that high RF carriers are used for each imaging channel. The benefits are twofold. Firstly the multiplexer enables the elimination of the $1/f$ noise, secondly, high frequency carriers enable full range imaging by eliminating the mirror terms [8].

3.3.3 Polarisation sensitive imaging

Polarisation sensitive imaging is compatible with both time domain and swept source based OCT set-ups. The multiple phase element in Fig.(3.8) is a combination of OPD

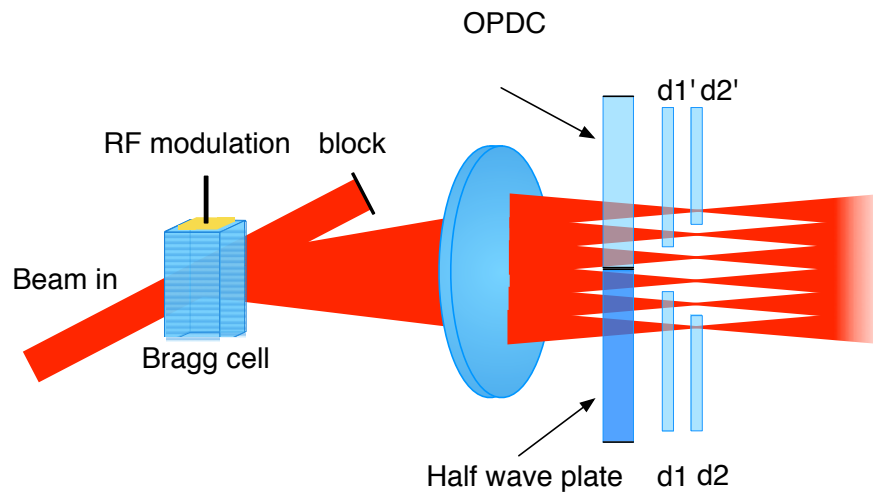


Figure 3.8: Schematic layout of the multiplexer design that can be used to interrogate the polarisation properties of the sample at three different depths.

steps and polarisation rotation steps. Multiplexer is compatible to record polarisation sensitive information from multiple channels when the multiplexer is driven at more frequencies and glass delay elements are used in conjunction with the HWP/OPDC pair as depicted. A half wave plate (HWP) intercepts 3 beams, while the other 3 are intercepted by an dispersion compensator (DC). This is used to compensate for the accumulated effect of OPD induced by the HWP and caused by the different refractive indexes along the ordinary and extraordinary axes of the acousto-optic crystal.

Two glass plates of different thickness, d_1 and d_2 in the first set of 3 beams and two glass plates of similar thickness, d_1' and d_2' are placed in the second set. The experimental cost and complexity in multiple depth polarisation sensitive imaging set-up, is similar to the multiple depth imaging set-up. To implement multiple depth imaging in PS set-up, only pairs of the optical delay elements ($d_1; d_1'$) and ($d_2; d_2'$) should be inserted in the path of conjugate H and V channels as depicted in Fig.(3.8).

A multiple channel multiplexer-based polarisation sensitive system can be used either for Jones matrix measurements using two orthogonally polarised channels in the

reference arm or for polarisation sensitive imaging at different depths (optical phase control element configuration depicted in Fig.(3.8)).

The multiplexers destined for PS-OCT are also compatible with both time domain and swept source based imaging configurations, in the same spirit of the example above at Fig.(3.8).

3.3.4 Structured interference

Sequential collection of images is performed in structured illumination microscopy. This principle was applied to OCT [163], where 10 frames of spectral OCT images were collected, for 10 different phase values of the sinusoidal modulation pattern created in the image by rotating an optical chopper wheel in the reference arm. The disadvantage of such method is that sequential collection of images takes time, which renders it inappropriate for moving targets. It would save time if all images were collected simultaneously.

The multiplexer technology presented in this chapter can be used to perform light efficient structured interference imaging. In this case the optical phase control element is eliminated and the signals in different multiplexer channels can be modulated in order to obtain specific illumination patterns. For example four channels can be used to project four sets of sinusoidal patterns where each pattern is phase shifted by 90 degrees.

Structured illumination algorithms have a general requirement to have a stable sample during the acquisition of subsequent phase-shifted images. The multiplexer presents the advantage that several phase-shifted illumination patterns are acquired at the same time. This idea has been presented in a patent application [114], but not implemented in this thesis.

3.4 Conclusions

This chapter various designs of a multiplexer that can be used in conjunction with either time domain or swept source based OCT set-ups were presented. We demonstrated how the selected optical bandwidth and the thickness of individual sections in the multiple phase control element determine the selection of carrier RF set values for all the simultaneous imaging channels. As well the relationship between the RF channel spacing, the optical bandwidth of the source and the thickness of the delays which allows minimisation of the footprint of a multiplexer, while avoiding the light from adjacent channels going through the same areas in the multiple phase control element, was determined. The chapter discussed how the multiplexer can be further simplified by using the same acousto-optic crystal for the creation and recombination of the first-order diffracted beam fan, but at the expense of slightly increased optical losses (as explained earlier in this chapter).

In the following chapters we will investigate how the multiplexer can be integrated into time domain based set-ups to perform simultaneous *en face* imaging at different depths as well as in swept source OCT set-ups for long axial range. The possibility of polarisation sensitive measurements in both time domain and swept source configurations will also be discussed.

Chapter 4

Simultaneous multiple-depths *en face* optical coherence tomography using multiple signal excitation of acousto-optic deflectors

4.1 Introduction

Optical coherence tomography (OCT) is a noninvasive, noncontact imaging modality that has the potential to produce high-resolution cross-sectional images of biological tissue [56, 150]. It has been reported that conventional Time Domain (TD)-OCT can provide high transversal resolution, real-time transverse (*en face*) constant depth images [116]. Although Spectral Domain (SD)-OCT is currently regarded as superior in terms of acquisition rate or signal to noise ratio, TD-OCT is better for providing real-time constant depth images [117]. To exploit this TD-OCT advantage to the higher

extent, techniques that allow simultaneous imaging at several depths have been proposed. In a first attempt, two *en face* images from a *post mortem* human eye were collected with a configuration that was based on two Michelson interferometers each equipped with a mirror vibrating at a different frequency [119]. However, even after some conceptual improvements [120] the number of imaging channels was limited by an increasingly larger dispersion in each additional channel. In a different approach, recirculating loops in both reference and sample arms of a low coherence interferometer were used [101]. More than 10 channels were obtained, however the sensitivity from one channel to the next decreased by more than 4 dB. In addition, it seemed inappropriate to create multiple delayed replicas of the signal from an object, that already contains multiple signals originating from different depths.

In this paper, a different approach is considered for the simultaneous imaging of a sample at multiple depths, that can ensure constant sensitivity amongst the channels. Multiple delays are created in the reference arm only, avoiding replication of the object beam. The optical configuration proposed is based on a combination of acousto-optic modulators with stepped optical delays. Such combinations of acousto-optic modulators with optical delays have been initially reportedly used in the practice of phased array antenna signals [125]. Acousto-optic modulators have also been reported in the practice of OCT [52] and low coherence interferometry [126], to create a stable, high frequency carrier for the interference signals. A combination of an acousto-optic modulator, operating as an Acousto-Optic Deflector (AOD), with a stepped mirror array was used to provide high speed stepped axial scanning [126]. A pair of AODs were also used in conjunction with optical delay lines, in a configuration originally developed for time-delay based photonic signal processing applications [124]. A similar principle has been used for space-division optical switching in telecommunications [53].

Novel functionality for pairs of AODs interleaved with optical delays is demonstrated here, by simultaneously driving the AODs with several radio frequency (RF) signals, of different frequency. The AODs and the optical delays are incorporated into a multiplexer block placed in the reference arm. The first AOD splits the incident beam into N directions and a different optical delay is introduced into each split beam. Then all the beams are recombined using the second AOD. To compensate for dispersion [126], a similar pair of AODs is used in the object arm, where no delays are used between the AODs. Such a configuration allows interrogation of N different OPD locations simultaneously. The configuration is equipped with a pair of transversal scanners, to achieve optical coherence tomography functionality. For each pixel in transversal section of an object investigated, pixel chosen by the pair of transversal scanners, interference signals are produced simultaneously from backscattered signals returned from N depths in the object.

4.2 Method

4.2.1 Set-up

The schematic drawing of a TD-OCT system capable of simultaneously acquiring several images from multiple depths is depicted in Fig.(4.1).

Light from a *Superlum SLD-371-HP-DIL-SM-PD* superluminescent diode emitting at 840 nm central wavelength with a 50 nm FWHM spectral bandwidth is amplified by an optical power booster *Superlum 850-50*. The resulting amplified optical power is 23 mW with a central wavelength of 850 nm and ~ 15 nm FWHM spectral bandwidth. The light from the booster is then inserted into a 50/50 single mode directional coupler that divides light into an object and a reference arm. The polarisation of light is

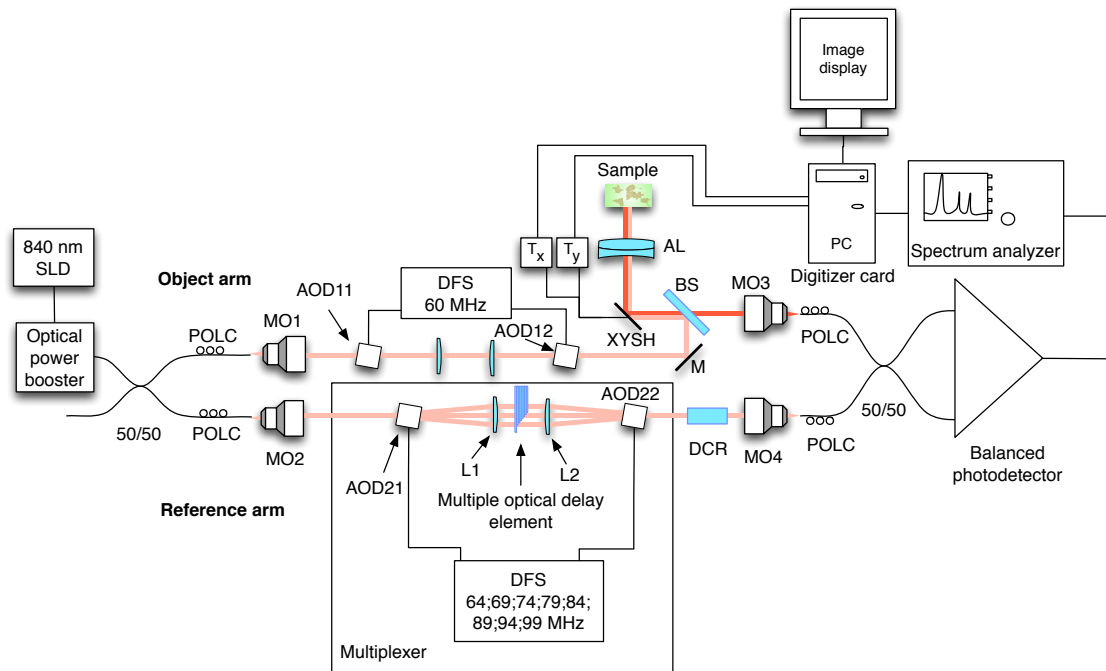


Figure 4.1: Schematic layout of the multiple-depths *en face* OCT system. MO1,2,3,4: microscope objectives; AOD11, 12, 21, 22: acousto-optic deflectors; POLC: polarisation controllers; XYSH: transversal scanning head equipped with mirrors to scan along X and Y; L1, L2: lenses; M: mirror; DFS: digital frequency synthesiser; DCR: dispersion compensator rod; AL: achromatic lens; BS: beamsplitter; PC: personal computer equipped with a digitiser to produce the image on the PC display.

controlled using *Newport F-POL-IL* polarization controllers, POLC. The light output of the first coupler is collimated with two microscope objectives MO1, MO2. All microscope objectives in Fig.(4.1) are 10x *OFR LLO-4-18-NIR*.

The light in the reference arm then passes through *Gooch and Housego 46080-1-.85-LTD* acousto-optic deflectors, AOD21 and AOD22. The deflectors are operated with a *Gooch and Housego* digital frequency synthesiser *MSD040-150-0.8ADS2-A5H-8X1*. The frequency synthesiser is controlled via a computer and can be tuned within 40 - 150 MHz range in 1 kHz increments. It can generate maximum $N = 8$ channels operating simultaneously with up to 200 mW of RF power delivered per channel. The light passing through the AOD21 can be diffracted into a number of beams, from 1 to

8. Two plano-convex BK7 singlet lenses L1 and L2 with focal length $f = 1$ m are placed at the focal length distance from the deflectors. A multiple optical delay element is inserted between the lenses so that each diffracted beam passes through a different glass step as depicted in Fig.(4.2). At the insertion point, all the beams are parallel and each beam is slightly converging. The lens L2 converges the fan of diffracted beams on the AOD22, driven by the same set of N RF signals, of identical frequencies as applied to AOD21. Light levels on each diffracted beam can be digitally controlled in each of the 8 channels. After AOD22, all beams in the first diffracted order are collinear and therefore they can be easily injected into a second 50/50 single mode optical fiber coupler using the MO4.

To match components for dispersion, the same combination of deflectors and lenses is used in the object arm, however both AOD11 and AOD12 are driven at a single frequency of 60 MHz. Additionally, after AOD22 in the reference arm, a dispersion compensator rod, DCR, made of SF6 glass is used to compensate for dispersion that is introduced by the lenses and beamsplitter in the object arm.

After the AODs in both arms, the first-order diffracted beam is selected by using a pin-hole conveniently placed (not shown). In the object arm, light is directed by a mirror M to a thick 50/50 beamsplitter plate, BS, which reflects the object beam to a pair of galvanometer scanners, in an XY scanning head, XYSH. The X-scanner determines the line in the final image and is driven with a triangular signal at 500 Hz, generated by a generator TX. The frame is completed by scanning the line vertically using the Y-scanner driven by a sawtooth signal at 2 Hz, provided by a generator TY. The beam is focused on the object using an achromatic doublet lens, AL of $f = 30$ mm. The reflected light propagates back along the same path till the BS, wherefrom it is launched via MO3 into the other input of the second 50/50 single mode fibre coupler, where it interferes with the light from the reference arm. The interference signal is pho-

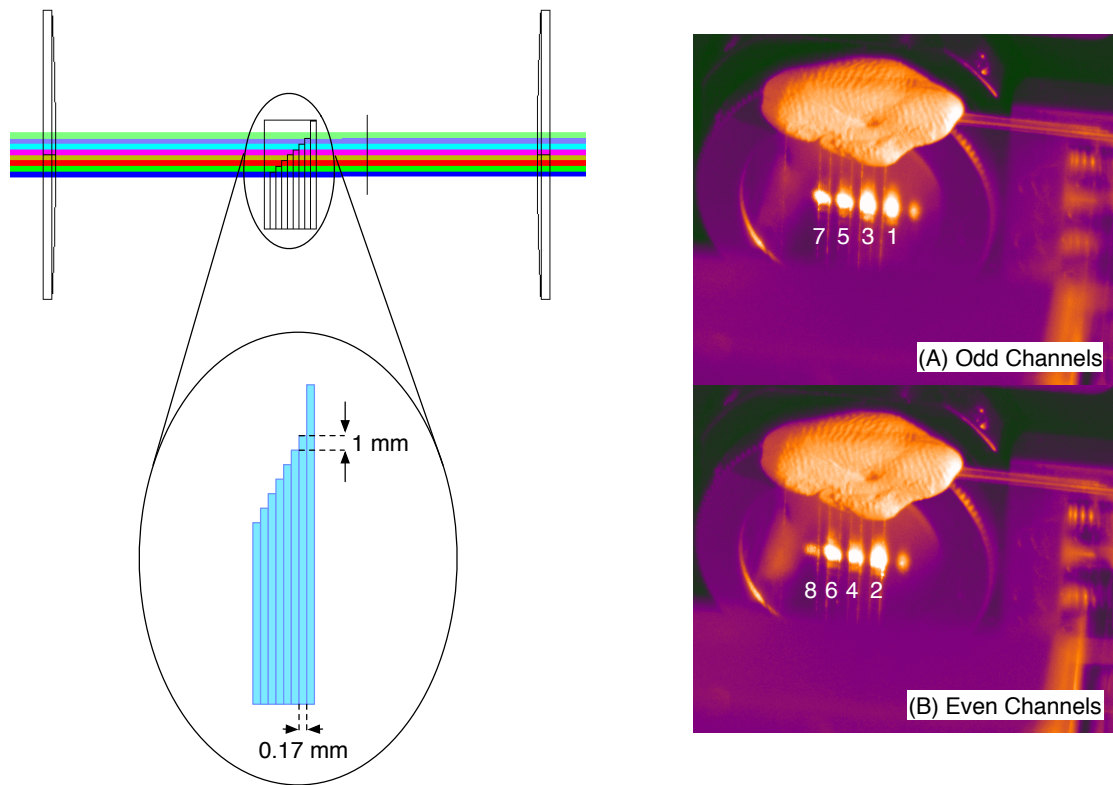


Figure 4.2: *Left*: schematic drawing depicting the structure of the multiple optical delay element and its positioning within the fan of diffracted beams, each considered collimated; *Right*: photos of a delay element with four odd (A) or four even (B) channels turned on simultaneously with the channel number p written below the corresponding light spot. The delay element is fogged with water vapours to enhance the visibility of the passing optical beams.

to detected with a 80 MHz *New Focus 1807* balanced photodetector receiver. The RF spectrum of the photodetected signal is analysed using an *HP 8590A* spectrum analyser. This is also used to sequentially produce an *en face* image for each depth. To this goal, the spectrum analyser is tuned on each carrier corresponding to each imaging channel, its span is set to zero and its detection bandwidth adjusted to the level of the image bandwidth, at 300 kHz. In this way, the spectrum analyser operates as a mixer followed by a low pass filter. The signal from the spectrum analyser is sent to a digitiser placed inside the PC, a card *NI PCI-5124*. This digitises the signal and in conjunction with the TTL signals from the signal generators, T_X , T_Y , driving the two

transversal scanners, synthesises an *en face* OCT image on the PC display. By tuning the *HP* spectrum analyser to each carrier, an *en face* OCT image is generated for each depth selected. The multiple carriers of different frequencies are produced simultaneously and are modulated in intensity with the interference signal corresponding to the depth selected by each individual delay step in the multiple optical delay element. The system presented is simultaneous in generation of multiple carriers for several optical delays, but due to the limitations in the display capability, only a single image can be displayed at any given time. Full functionality of simultaneous display of images can be accomplished with 8 similar spectrum analysers tuned each on a different frequency. Equivalently, 8 such RF filters can be assembled on a specialised digitiser.

All AODs used perform up-shifting the frequency of the incoming beam. The AODs in the object arm are driven at 60 MHz and the AODs in the reference arm are driven simultaneously at $f_p = 64 \text{ MHz} + 5 * (p - 1) \text{ MHz}$, with $p = 1$ to 8. This gives: 64, 69, 74, 79, 84, 89, 94 and 99 MHz. Then, the frequency of the beating photodetected signal, ν_p , results as $2 * (64, 69, 74, 79, 84, 89, 94, 99) - 2 * 60 = 8, 18, 28, 38, 48, 58, 68,$ and 78 MHz.

4.2.2 Delay method

If a laser beam is launched into an acousto-optic crystal at the Bragg angle, most of the incident light will be diffracted into the first order of diffraction, $m = 1$. The Bragg angle for the specific acoustic and optical wavelengths can be calculated using eq.(4.1).

$$\theta_{Bragg} = \frac{\lambda_0}{2\Lambda}, \quad (4.1)$$

where θ_{Bragg} denotes the Bragg angle in air, λ_0 is the wavelength of light in free space and Λ is the acoustic wavelength in the crystal. The first order diffracted laser beam

carrying most of the incident optical power will then exit the crystal at an angle that depends on the acoustic frequency and can be calculated using eq.(4.2).

$$\theta_D = 2\theta_{Bragg} = \frac{\lambda_0 f}{2\nu}, \quad (4.2)$$

where $\nu/f = \lambda$, ν denotes the speed of sound in the crystal, f is the frequency of the RF signal used to excite the piezoelectric transducer and θ_D is the angle of the diffracted light in air in respect to the incident beam.

Although equations(4.1) and (4.2) indicate that the direction of the diffracted beam can be easily manipulated by controlling the operating frequency, f , it is also obvious that they add certain restrictions on the laser bandwidth that can be used when operating the device on several frequencies simultaneously. Two important implications for the function implemented here will be examined: variation of optimal angle of incidence and diffraction angles for different operating frequencies and optical beam spectral bandwidths.

First, we will simplify the case by making a few assumptions to reduce the analysis to a case closer to that used in the experimental set-up. In this example we will operate an acousto-optic deflector at the eight acoustic frequencies mentioned above, starting from 64 MHz with a step of 5 MHz for each subsequent frequency. We will assume that the AOD is made of tellurium dioxide that exhibits a sound speed $\nu = 4260$ m/s [44]. As an additional constraint, the deflected beams should be spatially separated to avoid crosstalk between channels. This imposes restrictions in terms of the angle of diffraction for the first order diffracted beams.

After diffraction of the incident beam into multiple diffracted beams, it is important to secure non-overlapping diffracted optical beams, to allow insertion of different optical elements in the paths of the multiple diffracted beams. By using eq.(4.2) and simple

trigonometry, a formula that allows evaluation of the lateral distance between beams from two adjacent channels, produced by RF signals of frequency $f_p + 1$ and f_p , where $p = 1$ to $p = 7$ was derived and presented in eq.(4.3).

$$\Delta x = l \left(\tan \frac{(\lambda_0 - \frac{\Delta\lambda}{2}) f_{p+1}}{\nu} - \tan \frac{(\lambda_0 + \frac{\Delta\lambda}{2}) f_p}{\nu} \right) - d, \quad (4.3)$$

Here Δx denotes the lateral distance between the FWHM boundaries of the two adjacent beams, d is the FWHM of the incident beam, l is the distance from the AOD to the point of observation, λ_0 is the central wavelength of the source, $\Delta\lambda$ is the optical bandwidth of the source and ν is the speed of sound in the crystal.

For instance, using Eq.(4.3) for a typical 840 nm SLD and for two beams diffracted by signals of 94 MHz and 99 MHz, the two beams do not overlap as long as the optical bandwidth is less than 43 nm. It should be noticed that the bandwidth value for non-overlap depends on the central wavelength used and is larger for longer wavelengths. Special care should be taken when choosing the bandwidth of the light source. As the technique, requires having spatially non-overlapping beams, to maintain a reasonable footprint of a system, the diameter of the optical beam must be also considered.

Before applying all 8 signals simultaneously to the two AODs, the multiplexer is investigated for three cases, where in each case, two signals of different frequency are applied only. In the first case, the AODs are operated at 64 MHz and 69 MHz, ($p = 1$) in the second case at 79 and 84 MHz ($p = 4$) and in the third case at 94 MHz and 99 MHz ($p = 7$). All three cases are modelled for a FWHM of the optical bandwidth of the injected optical signal of 0 nm, 20 nm, 30 nm and 40 nm. The graphs in Fig.(4.3) are obtained using Eq.(4.3) and demonstrate the effect of optical bandwidth on the allowed lateral distance, Δx , between adjacent beams.

Figure (4.3) demonstrates that there is a tradeoff between source bandwidth and the

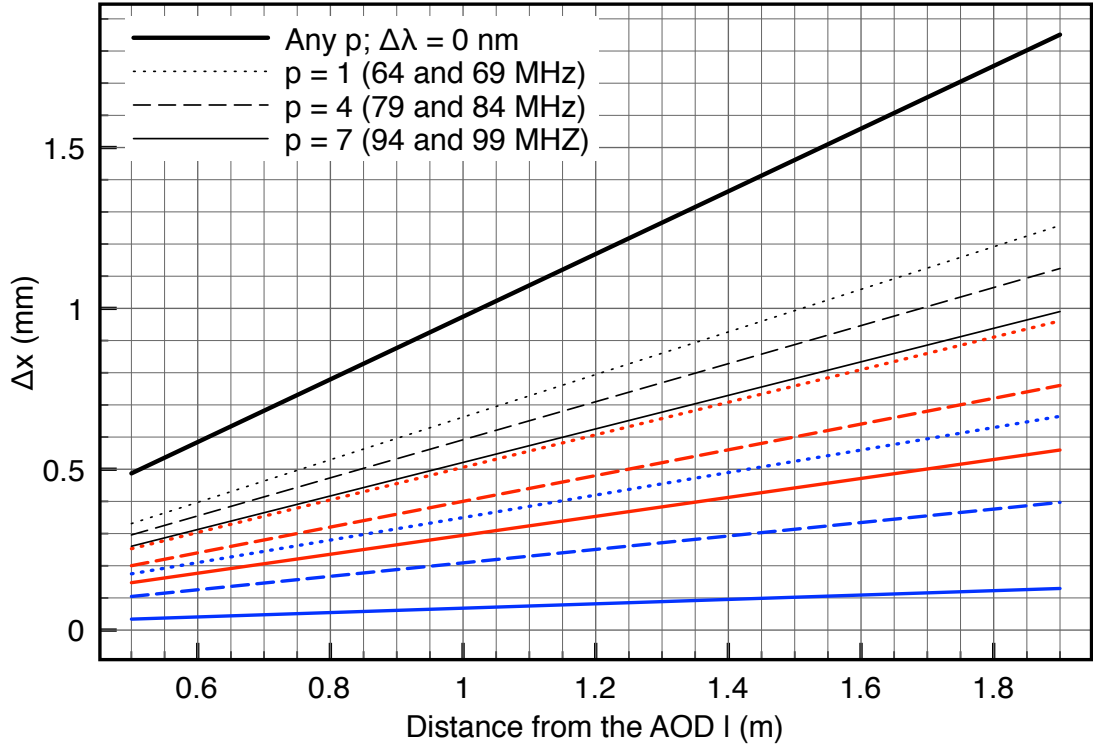


Figure 4.3: Distance Δx between the FWHM boundaries of two adjacent diffracted beams due to excitation of the AOD at the frequencies noted in the inset, (for different values of the index p in Eq.(4.3) and $d = 0$) as a function of distance l from the AOD. Central wavelength: 840 nm and four optical bandwidths, black bold: 0 nm, black fine: 20 nm, red: 30 nm, blue: 40 nm

footprint of the system. The larger the optical bandwidth, the wider the fan of diffraction, therefore, lower are the gaps Δx between adjacent channels, which can be only compensated by a larger l .

Figure (4.3) shows that for all the examples chosen there is no overlap of the beams. However, these graphs are obtained for $d = 0$ therefore for a given l , Δx from the graph in Fig.(4.3) should be interpreted as determining the maximum value d allowed for the beam diameter. The top black bold line, in Fig.(4.3), for an optical source with an infinitesimally small bandwidth shows the distance between the beam centres of the two adjacent beams. In this case the beam retains the same diameter when diffracted

by Bragg gratings of different periods.

The delay element requires an adequate spacing between beam centres (larger than the beam diameter of the diffracted beams, which depends on both the incident beam diameter and the combined effect of diffraction with the bandwidth of the optical source). Additionally, the edges of the individual delay elements are not perfectly cut and therefore some extra clearance is required between the beam FWHM boundaries (of at least 0.1 mm). A trade-off obviously exists between the separation of the diffracted beams and the footprint of the overall system layout.

Figure (4.3) shows for example that at $l = 1$ m distance from the deflector, for an optical bandwidth of 30 nm, Δx varies from 0.3 mm to 0.5 mm depending on the set of frequencies used. This suggests that the incident beam diameter can be increased up to the same value, of 0.3 – 0.45 mm. For the same $l = 1$ m, the bold dark curve which represents the distance between the beam centres, gives 1mm. These numerical values are compatible with delay elements of 1 mm width.

In order to be able to generate well separated *en face* OCT slices, the differential delay to be introduced should be equal or larger than the coherence length of the optical source used. Multiple optical delays can be implemented by stacking several glass plates in a stair like fashion as depicted in Fig.(4.2). In order to achieve small delays, thin borosilicate glass BK7 microscope coverslips of average thickness $\sim 170 \mu\text{m}$ are used. Counting on an refractive index $n = 1.51$, each such coverslip exhibits a differential optical delay of $\delta = 43 \mu\text{m}$.

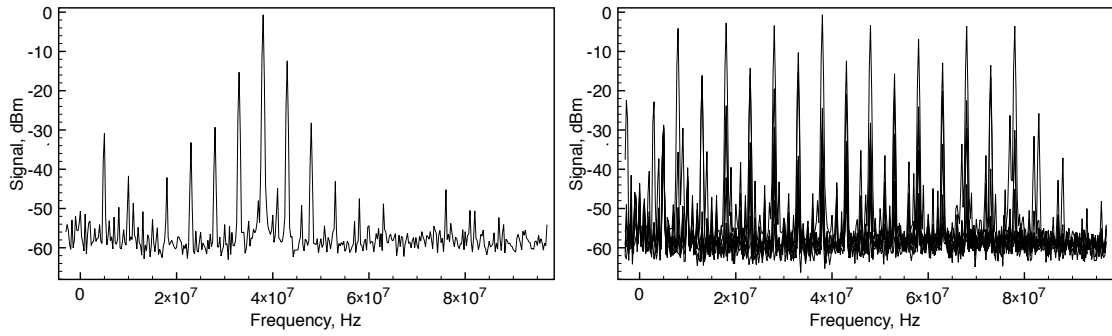


Figure 4.4: Typical frequency spectrum of the photodetected signal when all eight RF signals are applied simultaneously to the pair of AODs in the reference path. Left: reference arm length adjusted for the 4th (79 MHz) channel; Right: the reference arm length was subsequently adjusted in steps of $(p-1)\delta$, where $\delta = 43\mu\text{m}$, obtaining each time, a photodetected interference signal pulsating at $\nu_p = 8, 18, 28, 38, 48, 58, 68$ and 78 MHz and then superimposing the RF spectra from all eight channels.

4.3 Results

4.3.1 RF spectrum of the photodetected signal

In the following, results are presented that have been obtained by driving the two AODs in the object arm at 60 MHz. The AOD21 and AOD22 in the reference arm were driven at $64\text{ MHz} + (p-1)5\text{ MHz}$, with $p = 1$ to 8, the channel order. The interference information from different depths is carried by signal of frequencies equal to: $\nu_p = 8\text{ MHz} + (p-1)10\text{ MHz}$, as shown above.

To evaluate the performance of the configuration, a mirror was initially used as the object. Figure (4.4) presents the RF spectrum of the photodetected signal. The AOD21 and AOD22 are driven with all 8 RF signals simultaneously. The RF modulation power applied to each channel is then empirically adjusted so that the peak amplitude of the interference signal would be approximately the same for each individual imaging channel from optical path differences stepped by $(p-1)\delta$, with $p = 1$ to 8, where δ is the optical thickness of a single step in the multiple optical delay element. In

the left in Fig.(4.4 left), the RF signal analyser spectrum is shown when the optical path difference is adjusted to 3δ , in which case the carrier frequency is $\nu_p = 38$ MHz. In addition to the main peak at 38 MHz, intermodulation products either side of it exist, however they do not deteriorate image quality. Apart from electrical crosstalk originating from the frequency synthesisers and elastic crosstalk occurring in the Bragg cell crystal lattice, there is also optical crosstalk. This is due to light from the adjacent channels that goes through the same optical delay segment. For a single channel, the sensitivity was evaluated using a mirror behind a round trip attenuator of 34 dB and a single RF signal applied to the multiplexer. 22 dB signal over the noise level was measured. With a bandwidth of 100 kHz in the low pass filter of the analyser, this corresponds to a sensitivity of 106 dB in 1 Hz band centered around the carrier frequency. By applying 8 signals to the AOD21 and AOD22, the sensitivity is expected to reduce, as the reference power in each channel decreases by $N^2 = 8^2 = 64$ times in comparison to the power when only a single RF signal was applied.

Then, spectra for each $p\delta$ were obtained, by adjusting the reference path length using a translation stage to move the launcher holding the fibre input after AOD22. In this way, individual spectra for all 8 channels were obtained and presented in Fig.(4.4 right). The compound spectrum in Fig.(4.4 right) is equivalent to that obtained from a volumetric sample consisting of 8 parallel layers interspaced by $\delta/2$ and each returns the same amount of light.

4.3.2 *En face* OCT imaging

Figure (4.5 shows the autocorrelation function of the system, measured using a mirror as object, by axially displacing the launcher holding the fibre input after AOD22. For a spectral FWHM of 15 nm, the autocorrelation function FWHM should have been

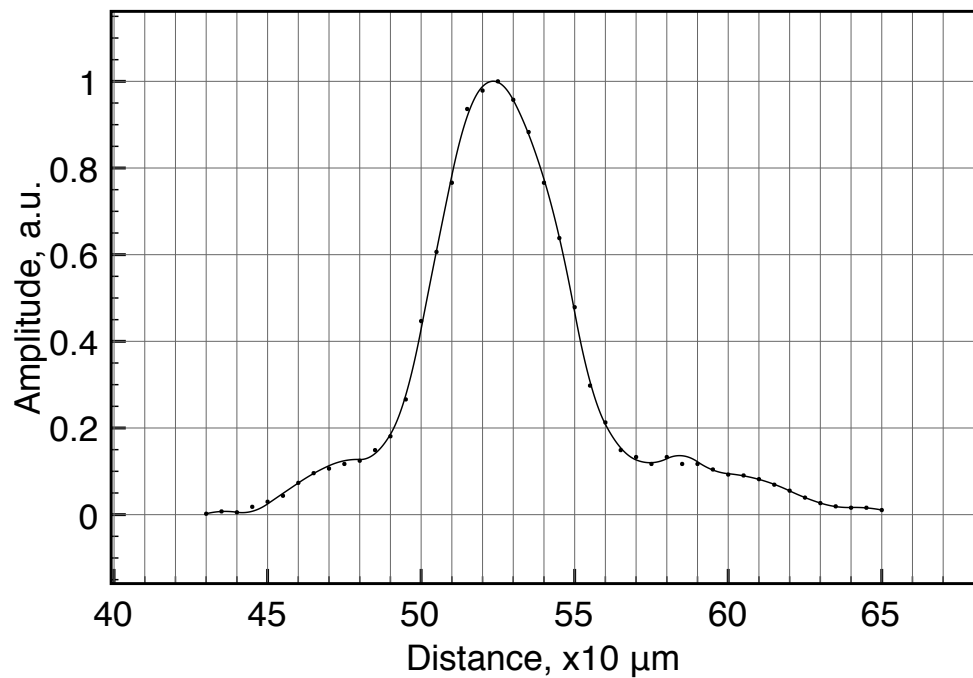


Figure 4.5: Normalised autocorrelation function for the compound source used in the experiments. The dots show measured values and the solid line is obtained by spline fitting them.

40 μm , however 47 μm was obtained (the depth resolution is half of these values, as moving the input fibre to the balanced coupler modifies a single trip of the wave along the reference path). This shows that the system still retains some uncompensated dispersion.

The system with 5 channels simultaneously driven (at 64, 69, 74, 79, 84 MHz) was used to image a sample of *Armadillidium vulgare*, also known as a common pill woodlouse. The RF modulation intensity in each channel in the reference arm was adjusted so that OCT image intensities from all depths exhibited similar strength.

The images in Fig.(4.6) are presented on logarithmic scale. The imaged area (width * height) in Fig. 6(A) is 1.7 * 1.9(0.1) mm^2 . Each original image consists in 500 * 500 pixels (500 pixels along 500 lines in the frame). Elimination of flyback at the line

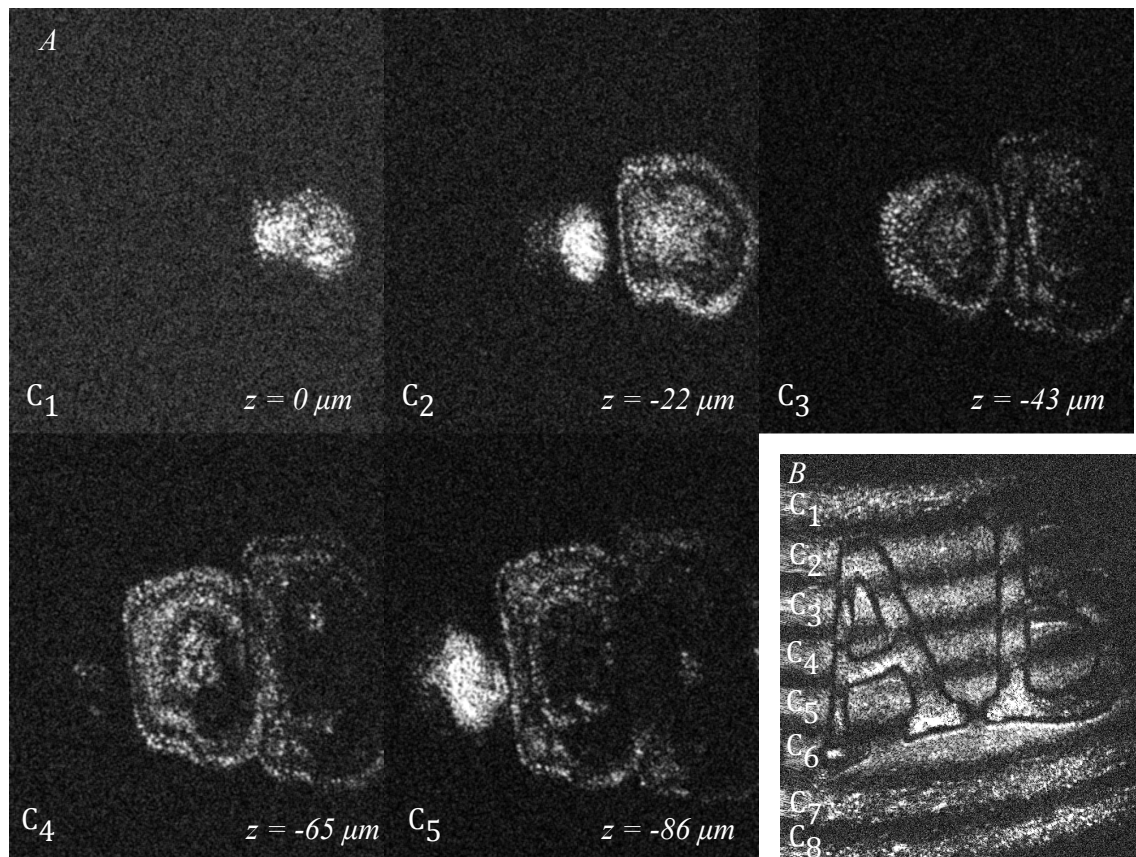


Figure 4.6: A) A montage of *en face* OCT images of *Armadillidium vulgare* dorsal side simultaneously acquired with five imaging channels operating at 69, 74, 79, 84 and 89 MHz. B). Superimposed maximum values of eight simultaneously generated *en face* images of a tilted 10 pence coin with all eight imaging channels operating simultaneously. z values represent depths of the *en face* OCT images in relation to the depth of the first image, arbitrarily set at $z = 0$, and where the steps in depth are set by the multiple delay element, as measured in air.

edges reduced the images to 441 pixels laterally. For a line scan of 500 Hz triangular excitation made from two ramps, each of 1 ms, an exposure time for each pixel in transversal section of $2 \mu\text{s}$ results. This is the time interval for acquiring simultaneously all N pixels in all N *en face* OCT images for each position of the object beam, as controlled by the signals applied to the X, Y galvoscaners. The incident optical power on the sample was 3 mW.

Figure (4.6A) shows up to three adjacent body segments of *Armadillidium vulgare* and

its shell structure. To reduce the image noise, an averaging filter that replaces the signal for each pixel with the average signal of its 3x3 neighbours is applied.

Then, the system with all 8 channels driven at (64, 69, 74, 79, 84, 89, 94, 99 MHz) was used to image a tilted 10 pence coin. Figure (4.6B), of $2.3 * 2.6(0.1)$ mm² shows the compound image obtained by superposing all 8 images. Due to the tilt of the coin, the image in each channel collects signal from a different part of the coin. The strength of the signal in the 94 and 99 MHz channels (given by the two bottom stripes) are multiplied by a factor 1.4 and 1.7 respectively to compensate for the responsivity loss of the photodetector at higher frequency signals.

4.4 Discussion

The combinations of an AOD and of pairs of AODs with delays have been suggested before as discussed in the introduction. Two different solutions have been reported: (i) a configuration using a single AOD and employing the zero and 1st order of diffraction to produce a bulk interferometer [126] and (ii) a configuration with two AODs [126, 124]. Here the solution with two AODs, (ii), has been adapted, more amenable to be used in transmission, which was implemented by incorporating two such AODs in each interferometer arm of a hybrid interferometer. The second configuration, (ii), is also compatible with balance detection. Such a configuration also allows separation of the path where optical signal processing takes place from the object path, where the signal is weak. In Fig.(4.1), the losses due to the AODs in the object arm can in principle be compensated by increasing the optical power from the source and the weak signal from the object does not need to traverse the AOD, as required by configuration (i). Securing low losses in the object arm when imaging biological subjects, especially the eye, is crucial for good signal to noise ratio.

In contrast to [125], [126, 124, 53], where a single signal of a varying frequency was applied sequentially at any given time, here multiple RF signals are applied simultaneously to drive the pair of AODs placed in the reference arm. Applying a single driving signal to the AOD presents the advantage that all optical power is diffracted by a single diffraction grating. Applying several signals of different frequencies to the AOD leads to division of optical power into multiple gratings, with a grating created by each applied RF signal. Therefore, the sensitivity drops with the increase in the number of channels. However, in principle, the same sensitivity value can be targeted with this configuration for all channels, as a major improvement from [101]. The sensitivity was evaluated using a mirror behind a round trip attenuator of 34 dB and a single RF signal applied to the multiplexer, in which case 22 dB signal over the noise level was obtained, for the optimum RF excitation. With a bandwidth of 100 kHz in the low pass filter of the analyser, this corresponds to a sensitivity of 106 dB in 1 Hz band centered around the carrier frequency. By applying 8 signals to the AOD21 and AOD22, the sensitivity is expected to be reduced, as the reference power in each channel decreases by $N^2 = 8^2 = 64$ times in comparison to the power when only a single RF signal was applied. Consequently, the interference strength on each channel is expected to decrease by $N = 8$. Additionally, the simultaneous application of N signals, creates the acousto-optic Bragg cell intermodulation products. Minimising the optical power losses due to intermodulation products requires the reduction of the amplitudes of the signals driving the AODs. As a further complication, the AODs responded differently to different frequency of the driving signal. Therefore, taking these criteria into consideration, the optimum set of RF powers when exciting all 8 channels, was experimentally found at each RF frequency, as follows, at 64MHz: 0.089W, at 69MHz: 0.098W, at 74 MHz: 0.069W, at 79MHz: 0.053W, at 84MHz: 0.020W, at 89MHz: 0.018W, at 94 MHz: 0.052 and at 99 MHz: 0.14W.

Further improvement of this multiplexing technology will be only possible by refinement of the crystal technology, and electrode excitation to allow significant RF driving powers while still maintaining spurious-free dynamic range suitable for imaging.

The method presented exhibits similarities to the SD-OCT, where the depth is encoded on the frequency of the photodetected signal. The larger the optical path difference (OPD) in the interferometer, the larger the number of peaks and troughs in the channeled spectrum at the interferometer output. By performing an FFT of the read-out signal of the channeled spectrum, the frequency of the output signal is proportional to the OPD, i.e. the OPD is encoded on frequency. A main difference is that SD-OCT can easily achieve more than 250 pixels in depth (for instance, when using a linear camera spectrometer with 500 pixels covered by the channeled spectrum, 250 cycles modulation are resolvable and each cycle in the number of cycles in the channeled spectrum corresponds to a coherence length). Here, the number of pixels in depth is limited to 8 only. It is expected that further work on the multiplexing technology will allow the application of more RF signals to AODs, with less crosstalk amongst the adjacent channels and optimised efficiency in using the light, enabling the imaging with more than 8 channels. Even after aforementioned developments, the method presented here will exhibit the same disadvantage as SD-OCT in terms of acquiring all depth under the same focus. However, this method does not exhibit the other two disadvantages of the SD-OCT, namely the decay of sensitivity with depth and mirror terms. The sensitivity here was almost the same on each channel and is expected to be the same even for an increase in the number of channels to larger numbers than 8. This is because each channel still operates like a TD-OCT, whose sensitivity does not depend on the OPD.

Regarding the mirror terms, SD-OCT suffers from OPD sign ambiguity. Therefore, in SD-OCT, the top of the object needs to be placed slightly away from the position where

OPD = 0, otherwise, if OPD = 0 is placed inside the object, the same modulation is produced in the channeled spectrum for scattering points placed symmetrically around OPD = 0 and the part of the image corresponding to positive OPD is superposed to the part of the image corresponding to negative OPD.

The method presented here does not suffer from this phenomenon. The frequency of carriers is strictly dependent on the diffracted beam used on each delay step, hence, each depth in the object determines a unique frequency value.

This property, of unique allocation of frequency to an OPD value illustrates the potential of the method to be extended to SD-OCT, where it could ensure mirror terms free demodulation and an extension of the axial range [13]. This possibility is the subject of a future research, where a swept source would replace the broadband optical source used here. In such a case, the demand for a high number of channels is significantly reduced, as two or three carriers may suffice to cover the most objects that are currently being investigated in practice of OCT as they usually do not exceed the thickness of a few millimetres.

When compared with the current level of SD-OCT technology, this method is sufficiently competitive in terms of the time required to produce an *en face* image. The *en face* images presented here are made from 500 lines of 500 pixels, acquired in 0.5 s. Considering a commercial swept source at 100 kHz or a linear camera at 100 kHz, the collection of 500 * 500 A-scans would require 2.5 s, without considering the time for data calibration and computational slicing of the volume created.

This method is only outperformed in terms of the time required to produce an *en face* image by extremely fast spectral OCT systems operating over 1 MHz line rate [70], which can acquire the same volume as in the example above in 0.25 s. However, the method presented here exhibits the advantage that any movement of the object

while it is being imaged, distorts all the *en face* images originating from all the depths collected, at the same time. This is not the case for SD-OCT, based on collection of A-scans. Dealing with a similar distortion in all *en face* images may allow a simpler correction procedure for movement effects.

4.5 Conclusions

A system capable of performing *en face* OCT imaging at eight depths simultaneously has been presented. The system was used to generate five OCT images from an *Armadillidium vulgare* specimen and eight simultaneous images of a metal surface of a tilted 10 pence coin. RF encoding of optical path difference allows simultaneous imaging and decoding of interference signals from different depths by using a single photodetector receiver. The main advantage of such an approach is the possibility to secure similar sensitivity across all channels by adjusting the RF powers of the driving signals applied to the AODs. As an additional advantage, low differential dispersion between adjacent channels is achievable by fabricating the optical delays in the multiplexer using a similar material to that of the object investigated.

Because the division of power amongst channels is confined to the reference arm only, higher number of channels may be possible with future improvements in the power of white light spatially coherent sources. If such high power optical sources become available, then the increase in optical source power can be compensated by decreasing the efficiency of the 1st coupler towards the object arm, to maintain the same safety power level on the object, while transferring more proportion of the power towards the reference beam, subject of division to an increased number of channels.

A further more immediate improvement should be in displaying all N images simulta-

neously. For the moment, all $N = 8$ channels are acquired in parallel, but a single RF filter was available, made from a spectrum analyser which needed to be sequentially tuned to each carrier to obtain the corresponding *en face* OCT image. Procedures are currently devised to store a full frame of the RF compounded photodetected signal, which will allow digital filtering of all N carriers in parallel and by doing so, enabling the technology to be used for imaging moving organs.

Chapter 5

Multiplexing based polarisation sensitive *en face* optical coherence tomography

5.1 Introduction

Optical coherence tomography (OCT) [56] is a high-resolution non-invasive imaging technique that allows imaging of translucent structures [117]. Originally developed for applications in the field of ophthalmology, OCT has been extended to imaging a wide variety of other biological tissues. It has been observed that many tissues such as muscle, teeth, nerve, bone, and cartilage and various ocular tissues [36, 112] as well as composite structures in material science [145] exhibit birefringence. For such tissues polarisation sensitive (PS) OCT [51, 26, 29] can be used to obtain additional structural information. PS-OCT allows measuring the polarisation properties of the object being imaged as well as its reflectivity. Making the OCT sensitive to the po-

larisation properties of the object increases the contrast in the image as well as open avenues to perform quantitative measurements [36].

Applications of PS-OCT are diverse such as material strain field mapping [144], burn depth estimation [68] and retinal fibre layer assessment [43]. Most of the early work on PS-OCT was done by sequentially illuminating the sample with polarised light and then calculating its polarisation properties. The sequential approaches offered sufficient polarisation data [162] but the sequential nature of the measurements slowed down the acquisition process. Other approaches relied on using two separated optical imaging channels of vertically and horizontally polarised light and then detecting each channel with different detectors [29, 144]. This approach required two complete OCT imaging channels with separate optical splitters and electronics, including a photodetector unit. If balance detection was to be implemented, such schemes required 4 photodetectors. Moreover, the conventional approaches require the division of an already weak object signal, in order to record several channels at the same time.

Other solutions applied electro-optic modulators and achieved stable signal carrier creation and increased speed in the sequential measurement of the polarisation states [133], Another paper considered a dual electro-optic modulator, and demonstrated Stokes vector measurements at up to 0.5 MHz, effectively decreasing the adverse impact of sample movement induced alignment errors in polarisation calculations [141].

Configurations employing acousto-optic deflectors (AOD)s were previously demonstrated as a tool for stable carrier creation in OCT [52] and low coherence interferometry [126]. Also, pairs of Bragg cells were combined with a multiple delay element for simultaneous depth time domain (TD) OCT imaging and for long range swept source imaging, presented in chapters 1 and 3. This chapter extends the applicability of multiple path OCT channels configurations based on AODs towards demonstrating polarisation sensitive functionality. This chapter presents a novel configuration, which

employs a multiplexer configuration based on two acousto-optic modulators (AOD)s that can allow a diversity of polarisation states being detected simultaneously. Such a multiplexer is used here to create two simultaneous imaging channels. Both imaging channels carry information about the amplitudes of interference that arise from vertically and horizontally oriented polarised light in two separate channels, V and H respectively. The same balanced photodetector unit is used for both V and H channels and the amplitude and the polarisation information is coded on the modulation of carriers of different frequency for the two polarisation channels. One of the main advantages of our set-up is that it allows multiple channel imaging without imposing any requirement for division of the light backscattered from the object to be shared by different OCT channels.

5.2 Methods

5.2.1 Experimental set-up

Figure (5.1) shows a sketch of the assembled instrument. A broadband SLD light source (*Superlum S840-B-I-20*) emits a beam with a centre wavelength $\lambda_0 = 830$ nm and a bandwidth $\Delta\lambda \approx 50$ nm. The light is further amplified by an Optical power booster *SOA-840-30* up to 25 mW, while the optical bandwidth is reduced to ~ 15 nm. The optical power is equally divided by an optical fibre beam splitter into object and reference arms. Both object and reference arms employ acousto-optic deflectors (AOD)s, that serve multiple purposes: (1) up-shift optical beam frequencies, (2) create multiple beams in the reference arm and (3) equalise the dispersion in both arms. After each AOD in the system, only the first-order diffracted beams are selected using pinholes (pinholes and blocked beams are not shown in the figure). Bare fibre polar-

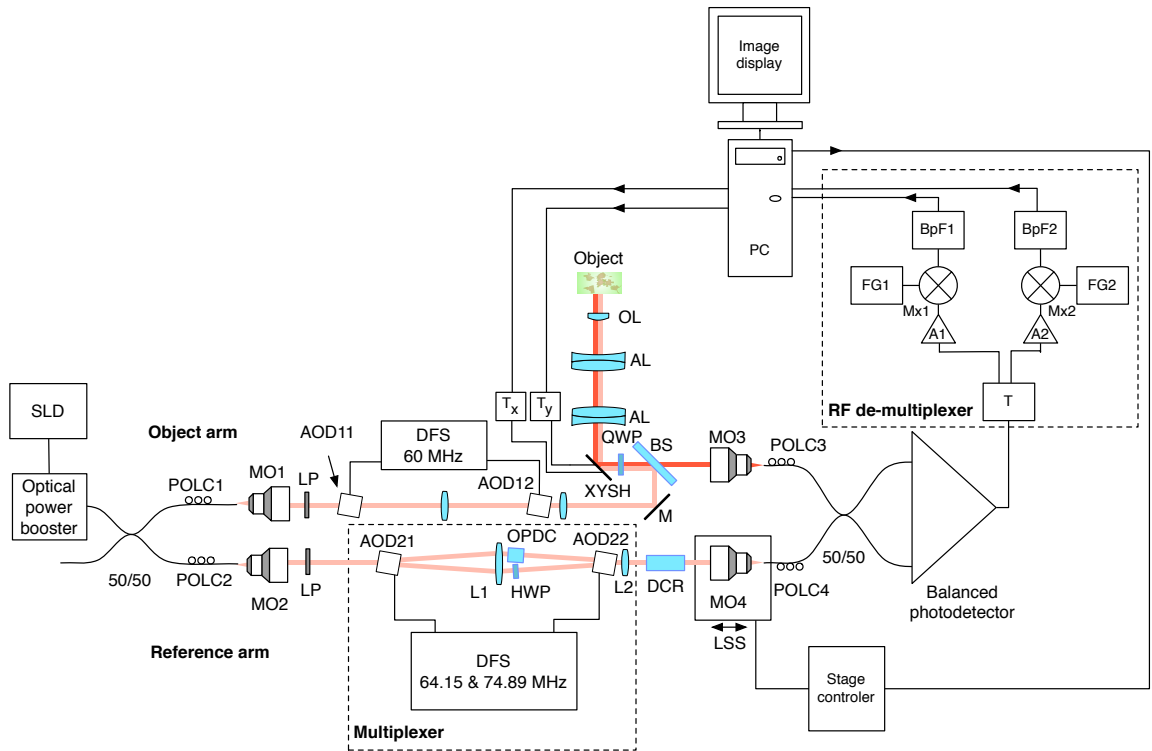


Figure 5.1: Schematic layout of the RF encoded polarisation OCT system. MO1, 2, 3, 4: microscope objectives; AOD11, 12, 21, 22: acousto-optic deflectors; POLC1, 2, 3, 4: polarisation controllers; LP: linear polarisers; OPDC: optical path difference compensator; HWP: half wave plate; QWP: quarter wave plate; XYSH: transversal scanning head equipped with mirrors to scan along X and Y; L1, L2: lenses; M: mirror; DFS: digital frequency synthesiser; DCR: dispersion compensator rod; LSS: linear scanning stage; T_x , T_y : scanner controllers; AL: achromatic doublet lens; OL objective lens; BS: beamsplitter; T: electrical signal splitter; A1, 2 signal amplifiers, Mx1, 2 frequency mixers; FG1, 2: frequency generators; BpF1, 2: bandpass filters; PC: personal computer equipped with a digitiser to produce the image on the PC display.

isation controllers POLC1 and POLC2 are used to maximise the amount of vertically polarised light, which is launched into AOD11 and AOD21. Immediately after AOD11 and AOD21 the light in the object and reference arms passes through linear polarisers LP (*Thorlabs LPNIR050-MP*) to eliminate any residual horizontally polarised light.

Four AODs (*Gooch and Housego 46080-1-.85-LTD*) are used that are excited by signals delivered by digital frequency synthesisers (*Gooch and Housego MSD040-150-0.8ADS2-A5H-8X1*). In the object arm, AOD11 and AOD12 are operated at a fre-

quency $f_R = 60$ MHz and so the light which propagates through AOD11 and AOD12 is upshifted by $60 + 60 = 120$ MHz. After AOD12, the vertically polarised light passes through a zero order quarter wave plate (QWP) rotated at 45 degrees to produce circularly polarised light. Returning light, backscattered from the sample, passes the same QWP once again and is injected into a single mode 50/50 fibre coupler.

In the reference arm, both AOD21 and AOD22 are simultaneously operated at $f_1 = 64.15$ MHz and $f_2 = 74.89$ MHz frequencies. This helps to create and later recombine two first-order diffracted beams that are respectively upshifted by $64.15 * 2 = 128.3$ MHz (V imaging channel) and $74.89 * 2 = 149.78$ MHz (H imaging channel). After being diffracted by AOD21, one of the diffracted beams (H channel) passes through a zero-order half wave plate (HWP) rotated at 45 degrees, which rotates the polarisation by 45 degrees, ensuring the horizontal polarisation of the beam. In the optical path of the second beam (V channel) a glass optical path difference compensator OPDC is inserted which has an optical thickness equivalent to the sum of the optical thickness of the HWP plus the optical path difference due to TeO_2 crystal birefringence in the AOD22. The OPD induced by the TeO_2 crystal is due to the different values of the refraction index along X and Y axis. At 830 nm, the birefringence is $\Delta n = n_e - n_o = 2.369 - 2.223 = 0.146$. Experimentally measured OPD in air of 3.66 mm is in agreement with the result calculated using the crystal length of 22.5 ± 3 mm, specified by manufacturer. The two deflected beams are recombined by AOD22 and then injected into the 50/50 single mode fibre coupler. At this point we have two orthogonally polarised beams travelling similar paths. The light from the fibre coupler is detected with a balanced detector *New Focus 1807*, bandwidth 80 MHz. The beating between the object and reference arm signals leads to two radio frequency encoded channels, operating at 8.3 and 29.78 MHz, frequencies present in the RF spectrum of the photodetected signal.

Images are obtained by raster scanning the object using a pair of closely spaced galvanometer scanners XYSH, controlled by a ramp generator T_X and a sawtooth generator T_Y . Axial scanning is obtained by moving the linear stage LSS equipped with actuator (*Newport LTA-HS*). The position of the LSS stage is digitally controlled via a *Newport universal motion controller ESP300* through a RS232 PC interface. The set-up can support two imaging modes: (1) 3D volume imaging where the LSS is moved in between the acquisition of subsequent *en face* images and (2) B-scan imaging where the slow scanner, Y is kept stationary while continuously scanning the LSS in conjunction with fast X-scanning. In both cases the system is controlled using the *LabView*[®] interface on the personal computer PC.

The light in both object and reference arms is launched from fibers using lenses MO1 and MO2 (*New Focus 5724-B-H*), the FWHM of the transversal power distribution profile of collimated beams after the launchers is 0.8 mm. In the reference arm, the light is reinjected into fiber using the same *New Focus 5724-B-H* MO4 lens. In the object arm we have chosen to use a lens MO3 (*10x OFR LLO-4-18-NIR*) to increase the object light collection efficiency. The images are obtained using an aspheric $f = 25.6$ mm objective lens OL. The resulting NA of the interface optics towards the object is 0.02 that determines an Airy disk diameter of $\sim 25\mu\text{m}$ of the beam focused on the object.

Both arms of the second fibre coupler are equipped with polarisation controllers POLC3 and POLC4. These enable the control of the polarisation with the aim to ensure that the relative polarisation of the light from the object and reference arms before being injected into the 50/50 fibre coupler is the same as in free space. The condition of having the same relative polarisation is ensured by observing the interference peaks and adjusting fiber polarisation controllers POLC3 and POLC4 in such a way that when a silver mirror is used as an object, maximum interference is obtained in channel H,

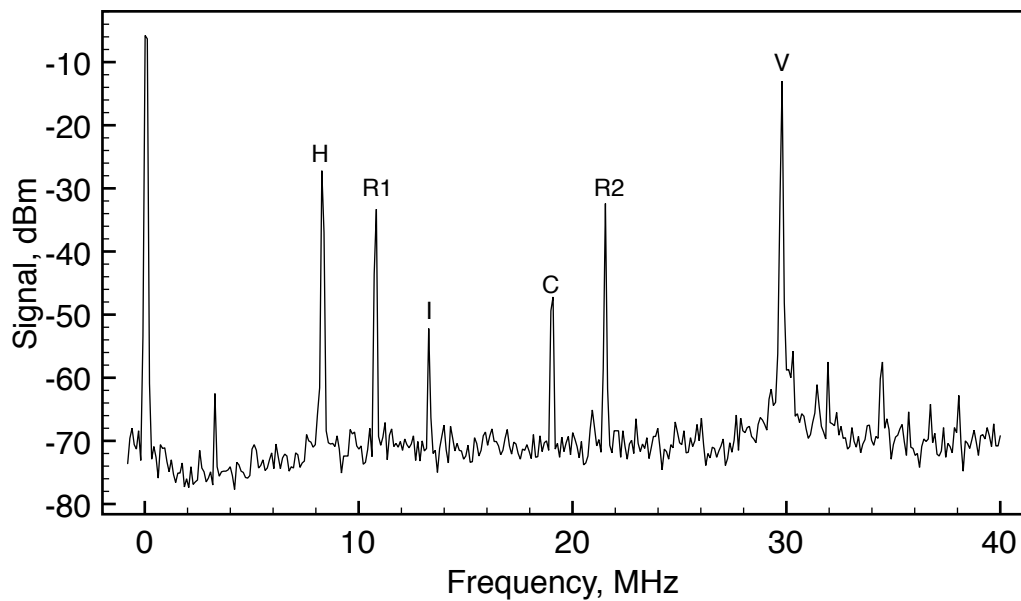


Figure 5.2: Typical photodetected RF spectrum when two signals are applied simultaneously to the AODs pair in the reference arm of the interferometer. Letters V and H denote two channels carrying the imaging information.

while minimum interference is obtained in channel V.

5.2.2 De-multiplexing of RF spectrum of the photodetected signal

The RF spectrum of the photodetected signal contains multiple carrier signals that are created by beating of the object and reference arm beams. This section presents how multiple carriers, carrying the interference information from different channels created by multiplexer, are extracted from the photodetected spectrum and then recorded for further digital processing to extract birefringence information.

Figure (5.2) illustrates a typical RF spectrum of the photodetected signal that was obtained by using a combination of an aluminium mirror and a sheet of birefringent plastic as an object and registering the spectrum by connecting the photodetector directly to the *HP 8590A* spectrum analyser. The photodetected signal contained peaks

from both V and H channels. The two AODs in the object arm were driven at $f_R = 60$ MHz, whilst the AOD21 and AOD22 in the reference arm were driven at $f_1 = 64.15$ MHz and $f_2 = 74.89$ MHz respectively. The interference information from the light with different polarisation states is carried by signals of frequencies of 8.3 MHz and 29.78 MHz.

When two sinusoidal signals of frequency f_2 and f_1 propagate through the acousto-optic crystal, several harmonics are generated, including harmonics pulsating at multiples of each frequency, as well as at the sums and differences of these harmonics, known as elastic two-tone third order intermodulation frequencies, for the full discussion please see ref. [44]. As a result, in addition to main peaks, third order intermodulation peaks arise and care has to be taken for such intermodulation products not to fall within the photodetected RF spectrum window.

The peaks R1 and R2 in Fig.(5.2) are due to the interference of the light in the reference arm and remains even if the light from the object arm is blocked. The reference arm crosstalk components can be found at $R1 = f_2 - f_1$ and $R2 = 2(f_2 - f_1)$ Hz, and if necessary can be easily eliminated by background subtraction techniques. The peak I is one of the third order intermodulation peaks that occur due to crystal lattice interactions and it is always present at $I_1 = 2f_R - (2f_1 - f_2)$ the other significant third order intermodulation product appears at $I_2 = 2f_R - (2f_2 - f_1)$. Third order intermodulation products can be reduced by applying lower RF power to the acousto-optic crystal. The last significant peak C1 appears due to the light being diffracted first by the grating produced by signal at f_2 and then by signal at f_1 or vice versa. The light, producing peak C1 propagates at a different angle than a multiplexed beam, however some of it is still injected into the fibre. Peak C1 can be minimised and eventually eliminated by: (1) increasing the difference in frequency Δf between the frequencies of signals applied to adjacent channels and (2) reducing the numerical aperture of MO2 and

MO4. However, additional peaks present in the spectrum do not deteriorate image quality, as they are outside the bandwidth of the RF de-multiplexer.

In this chapter, the system was used to create *en face* OCT images of up to 5 mm lateral size, determining approximately 200 pixels along the lateral coordinate. The bandwidth required when laterally scanning the beam at 500 Hz (1 ms for each ramp) over 200 pixels is approximately 400 kHz. The technology of AODs however allows larger carrier frequencies in order to accommodate larger bandwidths for faster *en face* scanning. In this case a resonant scanner at 8 kHz was used, scanning laterally at 16 kHz line rate [52], would determine a 16 times increase in the bandwidth necessary in comparison with what reported in this paper, i.e. 6.4 MHz. Such bandwidth can be accommodated by AODs operating at several hundreds of MHz and there are already commercial devices operating at over 300 MHz.

The carrier signals for channels V and H are extracted from the photodetected signal RF spectrum using the RF de-multiplexer. In the de-multiplexer, the signal is split equally into two channels using a signal splitter T (*HP 15104A*). The resulting signals are then amplified with low noise amplifiers (*Mini Circuits ZFL-1000LN*). The amplifiers act as electrical isolators that reduce crosstalk between the channels. The signals for both channels are downshifted using a combination of mixers Mx1 (*Mini Circuits ZAD-8+*), Mx2 (*Mini Circuits ZAD-1-1*) and signal generators FG1 (*Stanford Research DS335*) and FG2 (*Stanford Research DS345*) operating at frequencies equal to the signal carrier frequencies of both channels. The resulting signal from the mixer now contains both products of subtraction and summation of the photodetected and generated frequencies applied to the mixer inputs. The carrier signal, centred at 0 Hz is subsequently extracted and separated from the rest of the spectrum using a 300 kHz low pass filter (*Stanford Research SR560*). (The next setting of the low pass filter was 1 MHz, the increase in sharpness from the 300 kHz setting was insignificant in

comparison with the increase in noise, therefore some compromise of the transversal resolution was accepted). The two resulting channels are sent to a *NI 6110* card via a *NI SCB-68* interface, where they are digitised and registered in the PC.

5.2.3 Method of calculating the sample reflectivity and birefringence parameters

The polarisation states of the light traveling through the interferometer can be described by the Jones formalism [64, 65]. Here we present a simplified explanation of the model for the light propagation through reference and object arms. A more complete mathematical treatment of the polarisation states of the light passing through a similar system can be found in [134].

In both object and reference arms the beams after exiting the AOD11 and AOD21 are polarised vertically with linear polarisers. In the reference arm, the vertically polarised beam E_V remains vertically polarised. After passing through the HWP with its fast axis rotated at 45° , the polarisation state of the beam E_H , is rotated by 90 degrees. Both beams are recombined into a single beam by AOD22, however the orthogonal polarisation states components are now modulated at different frequencies.

The Jones matrix of an object can be described as of a general retarder. In the object arm, at the point where the light is injected into MO3, its Jones vector can be described as a product of initial vertical polarisation state propagated in reflection through QWP sample, as well considering the reflectance R of the observed point in the sample. It is broadly known that the interference resulting from the V and H channels in the reference arm and the object beam can be calculated using the formula (5.1),

$$I_k(z) = I_{r,k} + I_{o,k} + 2\sqrt{I_{r,k}I_{o,k}} \cdot |\gamma(z - z_0)| \cdot \cos(\Phi_k), \quad (5.1)$$

where $I_{r,k} \propto E_{r,k}^2$ and $I_{o,k} \propto E_{o,k}^2$ are the intensities of the object and reference beams respectively for $k = 1, 2$ for the V and H channel, $|\gamma(z-z_0)|$ is the modulus of the complex degree of coherence and Φ_k is the phase term of the interference signal. Eventually, using a Jones vector describing the object arm light at the injection point MO4, Eq.(5.1), and the known Jones vectors for both channels in the reference arm, the phase retardation $\phi(z)$ and reflectivity $R(z)$ parameters can be shown [51, 106] to be obtained using the following equations:

$$\phi(z) = \arctan \left[\left(\frac{I_V(z)}{I_H(z)} \right)^{1/2} \right], \quad (5.2)$$

$$R(z) \sim I_V(z) + I_H(z). \quad (5.3)$$

5.3 Results

Figure (5.3) shows the autocorrelation function of the system, measured using a phantom, consisting of a combination of a mirror and a thin birefringent plastic plate as an object (injection molded clear polystyrene Petri dish). For this measurement, the XYSH scanning mirrors were kept stationary and the plastic plate was moved laterally along X and Y directions until both interference peaks V and H reached the same amplitude. The autocorrelation function was measured by axially scanning the LSS on which the launcher holding the fibre input after AOD22 was mounted. For a spectral FWHM of 15 nm, the autocorrelation function FWHM should have been 40 μm , however a value of $\sim 50 - 60 \mu\text{m}$ was obtained (the depth resolution is half of these values, as moving the input fibre to the balanced coupler modifies a single trip of the wave along the reference path). This shows that the system still retains some uncompensated dispersion. Additionally, it can be seen that the FWHM for the V-channel is higher by $\sim 5 \mu\text{m}$. This indicates that although optical path was compensated using the

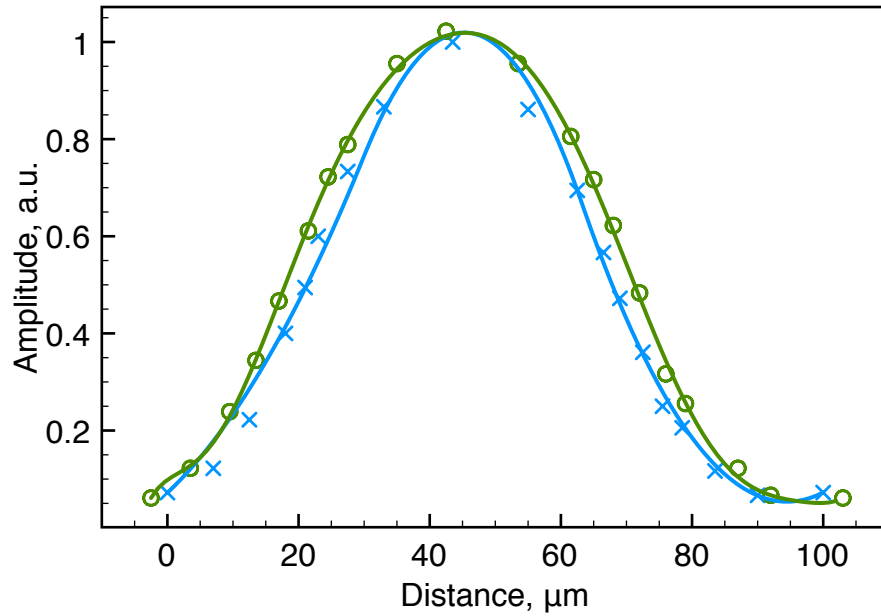


Figure 5.3: Normalized autocorrelation function for the compound source used in the experiments. The blue crosses and green circles show measured values for Channels H and V respectively, the solid lines are obtained by spline fitting.

OPDC glass rod, due to mismatch of optical materials Abbe numbers, the differential dispersion between two channels still remained. The signal to noise ratio for polarisation insensitive imaging, when using a silver mirror in conjunction with a 30000 times attenuator as a sample, was measured to be 47 dB in $2 \mu\text{s}$. The sensitivity of an instrument can be found by using the two values, $47 \text{ dB} * 30000 = 92 \text{ dB}$.

The increased FWHM of the autocorrelation function may be due to uncompensated dispersion between the object and the reference arm as only a glass rod DCR was used in the reference arm to partially compensate for the dispersion induced by beamsplitter BS, quarter wave plate QWP, two achromatic lenses AL and objective lens OL. The most straightforward way to improve the autocorrelation function would be to include matching optics in the reference arm, just after L2. We did not find it necessary to resort to a more increased complexity of the dispersion compensation system due to the narrow band of 15 nm of the compounded light source employed.

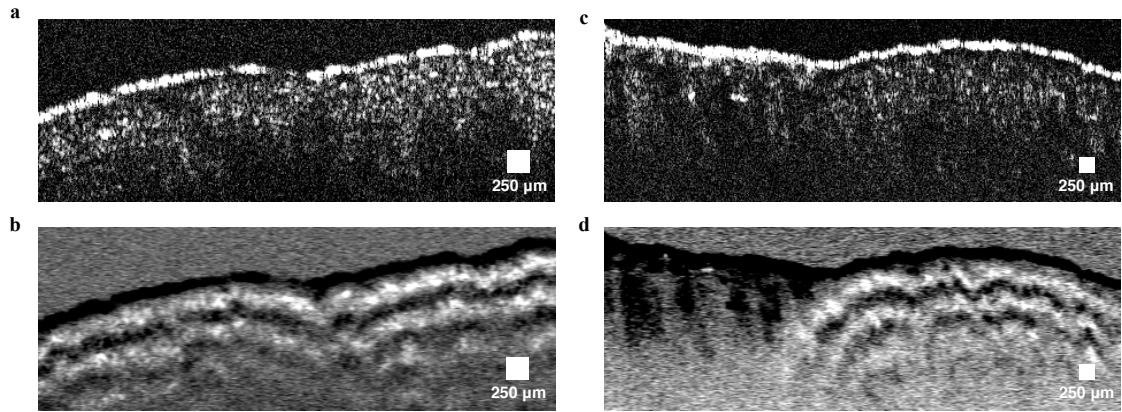


Figure 5.4: *In vitro* images of intact (a, b) and thermally damaged (c, d) muscle tissue. Top images show reflectivity of the sample while bottom images show the phase retardation as a function of depth $\phi(z)$. The reflectivity images are presented in a logarithmic scale. A low pass Fourier filter was applied on birefringence images to enhance the visibility of the birefringence bands.

To demonstrate the performance of the set-up in biological tissue, *in vitro* imaging of two samples of a chicken breast muscle tissue was performed. A raw sample and another thermally damaged sample by a short contact with a hotplate were compared. Both samples were cut from adjacent areas of a same muscle. For the intact sample, 131 C-scans were recorded with an increment of $13 \mu\text{m}$. For the thermally damaged sample imaging the scanning range of a fast scanner, T_x , was increased by 50% and 159 C-scans were recorded with an increment of $19 \mu\text{m}$. Reconstructed pseudo B-scan images consist of 450×131 and 450×159 pixels respectively, where any single pixel was exposed for $2 \mu\text{s}$ with a radiant flux on the sample of about 3 mW. The whole 32 Mega voxel volume was acquired in 1 minute. The reflectivity and birefringence images that were calculated using Eq.(5.2) and Eq.(5.3) are presented in Fig.(5.4).

The images that show phase retardation were additionally Fourier-filtered to remove the high frequency components. A low pass filter was applied to remove features smaller than 3 pixels in the collected *en face* images and B-scans were constructed from filtered images. In this way, the resolution along the axial direction, which determines

the contrast of birefringence bands, was not affected. Filtering has reduced noise while conserving the birefringence information carried by lower spatial frequencies, in this way allowing easier visual interpretation and potentially simplified automated segmentation of the birefringence image.

The pseudo B-scans in Fig.(5.4) present the two pairs of polarisation insensitive and the birefringence images acquired from a sample of chicken muscle tissue. First, the images of intact tissue were acquired (Fig.(5.4a) and (5.4b)), then the collagenous matrix of the tissue was altered by a short contact with a hotplate and the imaging was repeated. While the difference between the polarisation insensitive images (5.4a) and (5.4c) is not obvious, clear distinction of birefringence maps is visible in Fig.(5.4b) and (5.4d), where in Fig.(5.4d) the vanishing bands on the right indicate thermal damage.

5.4 Discussion

The method presented in this article demonstrates the versatility of frequency domain multiplexed TD-OCT, employing the pairs of Bragg cells to create multiple imaging channels. Two orthogonal polarisation states are processed to produce birefringence maps and polarisation insensitive images. The configuration presented has the potential to also achieve a multiple depth imaging capability (as in chapter 4). The method may be used to provide birefringence information from several depths simultaneously if the other channels available in the set of synthesisers are used. Although this looks possible, extra care and more research is required in reducing the cross talk between channels and increasing the sensitivity. This may be made possible if a larger power broadband source is used to allow for higher order splitting of power in the reference path. This information could be used to predict the birefringence maps over the whole volume of the sample, enabling fast screening of multiple areas and pinpointing

of problematic zones where further investigation is needed.

Due to birefringence of TeO_2 used for the acousto-optic crystals, with the current system design only two orthogonal polarisation states could propagate unaltered through the recombining AOD22 in the reference arm. Further work on the optical design of the system is needed to compensate for the birefringence of AOD22, so that any polarisation state could pass through it without being altered. In this way the multichannel capability could be used to the full extent to perform simultaneous measurements needed to calculate a Mueller matrix. This would help to interrogate the unpolarised light returned from samples with complex birefringent structures.

The frequency multiplexing method presented here enables the imaging of several channels simultaneously, without any added penalty of dividing the object signal. Our studies show that with more refinement, the multiplexer architecture can be implemented in reflection, reducing the cost and complexity of the system. The operation of a multiplexer in the reflection mode could be achieved by adapting one of the configurations used for optical delay lines [124] and using a recirculator instead of a polarisation beam splitter to achieve a polarisation sensitive operation. Reducing the number of Bragg cells required for the operation of a multiplexer would simplify the set-up while driving down its cost. A further study is needed to determine the feasibility of reflection approach.

The unique ability of the frequency multiplexing approach to provide multiple *en face* polarisation sensitive images from different depths simultaneously creates further opportunities for novel clinical applications. If the material is known, then the periodicity of bands can be estimated. Therefore the required OPD between sparsely selected T-scan lines can be calculated. For instance, in Fig.(5.4), where 4 bands exist, a minimum number of 8 T-scans are needed selected at axial depths of periodicity bands/2. Acquisition of several independently sparsely spaced polarisation sensitive images can

allow quick segmentation of volumetric images of tissue into areas displaying expected birefringence patterns and areas displaying unconventional patterns, due to disease or external damage. If movement takes place, then all *en face* images are disturbed similarly. Therefore, this method presents the potential to provide volumetric images at high frame rates, with extra capability in defining three-dimensional boundaries of abnormal zones in tissue based on their polarisation properties.

Another avenue where the strength of acquiring the polarisation sensitive measurements from multiple axial points could be exploited is the retinal imaging. Due to the fact that the acquisition of multiple pixels happens at the same time, this frequency multiplexing approach ensures that all the axial points acquired in simultaneous multiple *en face* images are perfectly overlapped laterally even in the presence of movement. Consequently, it can be guaranteed that the two signals contributing to the two orthogonally polarised channels originate from the same OPD value, unaffected by the movement of the tissue.

The multiple simultaneous measurements can thus be useful to reduce the effect of micro saccades. Additionally, frequency multiplexing may be suitable for fast volumetric polarisation sensitive imaging with sparse sampling along the axial direction [160].

5.5 Conclusions

The method presented in this chapter is able to perform simultaneous collection of polarisation information using the same photodetector receiver. For the moment, acquisition and processing was performed by using a spectrum analyser tuned sequentially on the two carrier frequencies. The *Gooch and Housego 46080-1-.85-LTD* drivers can

synthesise up to eight frequencies. In this way, the method is potentially expandable to simultaneously collecting several coefficients of Mueller matrices, or collecting two polarisation channels from up to four different depths, without splitting the object beam into 8.

Chapter 6

Frequency multiplexed long range swept source optical coherence tomography

6.1 Introduction

Optical coherence tomography (OCT) [56] is a non invasive imaging technique that has the potential to provide fast and high resolution depth-resolved information of the scattering properties of biological samples. To obtain an axial scan, time domain (TD)-OCT systems rely on the slow reference arm scanning [117]. Later developed spectral domain (SD)-OCT systems enabled fast acquisition [155] of axial scans within a range of several millimetres. One of the major limitation of the SD-OCT technology remains its depth dependent sensitivity drop, an effect commonly called as the sensitivity “roll-off”. In swept source (SS)-OCT systems, the sensitivity roll-off is due to the limited coherence length of the swept source used, while in spectrometer based (SB)-OCT

systems, the limited resolution of the spectrometer causes the roll-off [117].

Recent progress in the development of tunable lasers for SS-OCT have lead to swept sources with coherence length longer than 1 cm [156, 61]. However, when increasing the tuning speed, their coherence length diminishes [121]. There is an interest in imaging objects with an axial extension larger than 1 cm such as the human eye [156], or to perform topography of objects with variation in height larger than 1 cm. Therefore, there is a need for optical sources of longer coherence length, or equivalently, of methods that can compensate the sensitivity roll-off with depth.

In typical OCT biomedical applications, such as intravascular and gastrointestinal imaging, the light cannot penetrate biological tissue deeper than few millimetres [150] and the loss of backscattered light is a limiting factor, not the roll-off. However, in several biomedical applications such as balloon based endoscopic OCT [67] or gastrointestinal imaging [14], the distance to the sample can vary by few tenths of millimetres and the high imaging range is desired to obtain consistent quality scans.

Various approaches to increase the imaging range have already been reported. Several techniques have been developed to remove the mirror terms [115, 54, 79] and effectively double the imaging range by giving access to full axial range. A different approach, consisted in using a pair of recirculation loops in the object and reference arms [13] with a differential optical path difference comparable with the axial range given by the inverse of the line width of the swept source and using radio frequency shifts imprinted at each recirculation through the secondary loops, by frequency shifters.

This Chapter present a technique which allows substantial extension in the imaging range by: (i) elimination of mirror terms [8] and (ii) simultaneous acquisition of multiple axially shifted A-scans, by employing a frequency domain multiplexing method described in previous hapters. The multiple A-scans are encoded at different radiofre-

quencies (RF) employing the same approach as in frequency multiplexed time domain OCT. The use of a multiplexer, comprising of two lenses and a pair of a Bragg cells [125, 53] in conjunction with a multiple delay element, allows the production several conventional A-scans at different depths to be performed simultaneously. Each channel provides a full axial range A-scan, as it is free from mirror terms. It is also possible to adjust the differential depth difference in the multiple delay element, δ , that allows superimposing of several adjacent A-scans. In this way, dropping sensitivity in an A-scan is compensated by the increase in sensitivity in the adjacent channel.

6.2 Method

6.2.1 Set-up

The schematic diagram of a long axial range SS-OCT system is depicted in Fig.(6.1).

The swept source (*Superlum, Cork, Ireland, model Broad-sweeper 840*) is a tunable semiconductor light source, operating at 100000 nm/s sweeping speed, with a 828.0 – 873.0 nm spectral range. This corresponds to scanning $\delta\lambda = 45$ nm in 0.45 ms at a rate $4\gamma = 2.24$ kHz, with an equivalent repetition rate of 2 kHz. The light is amplified by an Optical Power Booster (*Superlum, Cork, Ireland, model 850–50*) to achieve more than 23 mW in a single mode fibre. The light from the booster is then injected into a 50/50 single mode directional coupler that divides light into an object and a reference arm. The polarisation of light is controlled using *Newport F-POL-IL* polarisation controllers, POLC. The light output of the first coupler is collimated with two microscope objectives MO1 (*New Focus 5724-B-H*) and MO2 (*10x OFR LLO-4-18-NIR*).

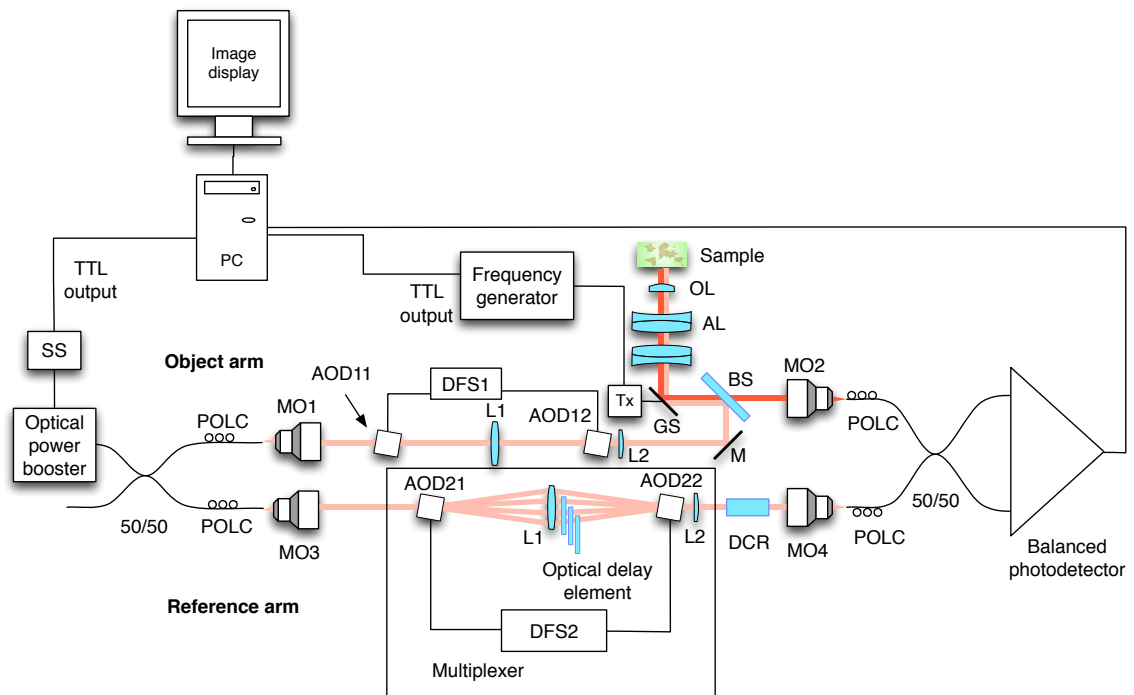


Figure 6.1: Schematic layout of the long range SS-OCT system. SS: swept source; MO1, 2, 3, 4: microscope objectives; AOD11, 12, 21, 22: acousto-optic deflectors; POLC: polarisation controllers; GS: galvanometer scanner equipped with a mirror to scan along X direction; T_x : scanner controller; L1, L2: lenses; M: mirror; DFS1,2: digital frequency synthesiser; DCR: dispersion compensator rod; AL: achromatic lens; OL: Objective lens; BS: beam-splitter; PC: personal computer equipped with a NI-5124 digitiser to decode each axial scan and produce the image on the PC display.

The light in the reference arm then traverses two acousto-optic deflectors, AOD21 and AOD22, from *Gooch and Housego*. The deflectors are operated with a *Gooch and Housego* digital frequency synthesiser *MSD040-150-0.8ADS2-A5H-8X1*. The frequency synthesiser is controlled via a computer and can be tuned within 40 – 150 MHz range in 1 kHz increments. It can generate a maximum of $P = 8$ channels operating simultaneously with up to 200 mW of RF power delivered per channel. The light passing through the AOD21 can be diffracted into a number of beams, from 1 to 8.

Lens L1 ($f = 500$ mm) is assembled from two closely spaced plano-convex BK7 singlet lenses, both with focal length 1 m, and placed at $2f$ distance from the deflectors. The multiple optical delays are inserted immediately after the L1 so that each diffracted

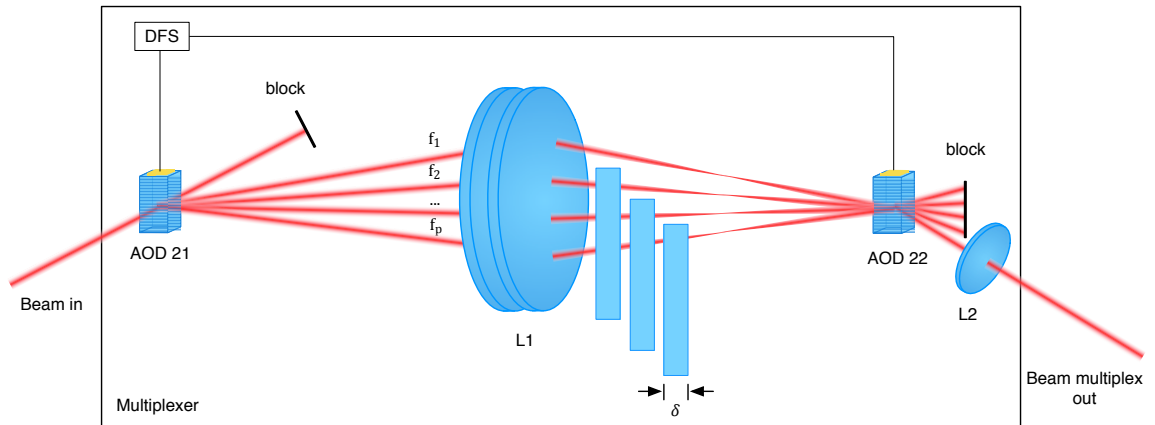


Figure 6.2: Frequency division multiplexer, where each diffracted beam traverses a different delay step. The steps are made from glass plates of optical thickness δ .

beam passes through a different glass block as depicted in Fig.(6.2).

The lens L1 converges the fan of diffracted beams on the AOD22, driven by the same set of P RF signals, of identical frequencies as applied to AOD21. Light levels on each diffracted beam can be digitally controlled in each of the P channels. A lens L2 ($f = 500$ mm) is placed immediately after the AOD22 to collimate the multiplexed beam. After passing the AOD22 and L2, all beams in the first diffracted order are collimated and collinear, therefore they can be easily injected into one of the inputs of a second 50/50 single mode optical fibre coupler, using the MO4.

The object arm is equipped with the same set of Bragg cells and lenses to compensate for dispersion, however a single RF signal of 60 MHz is applied on both AOD11 and AOD12.

In the object arm, light is directed by a mirror M to a thick 50/50 beam-splitter plate, BS, which reflects the object beam to a galvanometer X-scanner equipped with a mirror, GS. The X-scanner determines the line in the final image and is driven by a generator T_x with a sawtooth signal, generated by a *Thurlby Thandar Instruments TG210* frequency generator. The TTL output from the frequency generator is connected to the

PC via a *NI-5124* digitiser. The beam is focused on the object using a pair of achromatic doublet lenses, AL of focal length 75 mm, and an objective lens OL of focal length 40 mm. The lenses are arranged in a $4f$ configuration, which re-images the pupil plane on the galvo-scanner mirror with magnification equal to 1. The reflected light from the object propagates back along the same path up to the BS, wherefrom it is launched via MO3 into the other input of the second 50/50 single mode fibre coupler, where it interferes with the light from the reference arm. M3 and M4 use aspheric lenses *New Focus 5723-B-H*. An asymmetric choice of microscope objective and lenses was made to (i) minimise the diameter of the beams travelling through the acousto-optic deflectors and (ii) increase the clearance between the beams in the reference arm at the point where the multiple delay element is inserted.

To compensate for the dispersion due to lenses AL and OL and the beam splitter BS, a Dispersion Compensation Rod DCR is inserted in the beam after the lens L2 in the reference arm. After the AODs in both arms, only the first-order diffracted beams are selected by using pinholes placed conveniently, to block all the other orders (not shown).

The interference signal is photo-detected with a *New Focus 1807* balanced photo-detector of 80 MHz electrical bandwidth. The RF spectrum of the photodetected signal is digitised and analysed using a *National Instruments PCI-5124* card, which is installed in a PC.

6.2.2 Choice of excitation frequencies

All AODs are used to simultaneously create multiple signal carriers by upshifting the frequency of each deflected beam. Sufficient separation of diffracted beams by AOD21, comparable to the size of the beam diameters of a few mm requires a difference of

frequency in the signals applied to the AOD larger than several MHz, chosen here as 9.376 MHz. This simplifies the construction of a delay element by relaxing the step edge quality requirements and making the delay elements compatible with a beam diameter of up to 2 mm. The AODs in the object arm are driven at 60 MHz and the AODs in the reference arm are driven simultaneously at $f_p = 65.247 \text{ MHz} + (p - 1) * 9.376 \text{ MHz}$, with $p = 1$ to P . The drivers can drive up to $P = 8$ signals. In the experiments which follow, the maximum value for P was 4. The resulting carriers in the photo-detected signal therefore pulsate at $2f_p - 120 \text{ MHz}$, i.e. at frequencies:

$$C_p = C_0 + (p - 1) * \Delta F, \quad (6.1)$$

where $C_0 = 130.494 - 120 = 10.494 \text{ MHz}$ and $\Delta F = 2 * 9.376 = 18.752 \text{ MHz}$ as depicted in Fig.(4.3).

6.2.3 Data processing

The data acquired by the photo-detector, is digitised by the *NI PCI-5124* card, whose acquisition is triggered by the TTL sweeping signal provided by the SS and by TTL signal associated to the signal produced by the frequency generator used to drive the galvo-scanner. Thus a B-scan image is created.

First, the RF spectra representing single sweeps are extracted from the photo-detected signal using the TTL signal provided by the SS. The SS is driven in a saw-tooth fashion, therefore the signal due to the return of the frequency to the initial value (50 microseconds) is eliminated. Each packet extracted in this way is processed to produce an A-scan. The packets then are resampled to place the data in equal frequency slots. Then a fast Fourier transform (FFT) is performed on each sweep to produce a 1D array, containing the A-scan interference signal amplitude data for each of the carriers

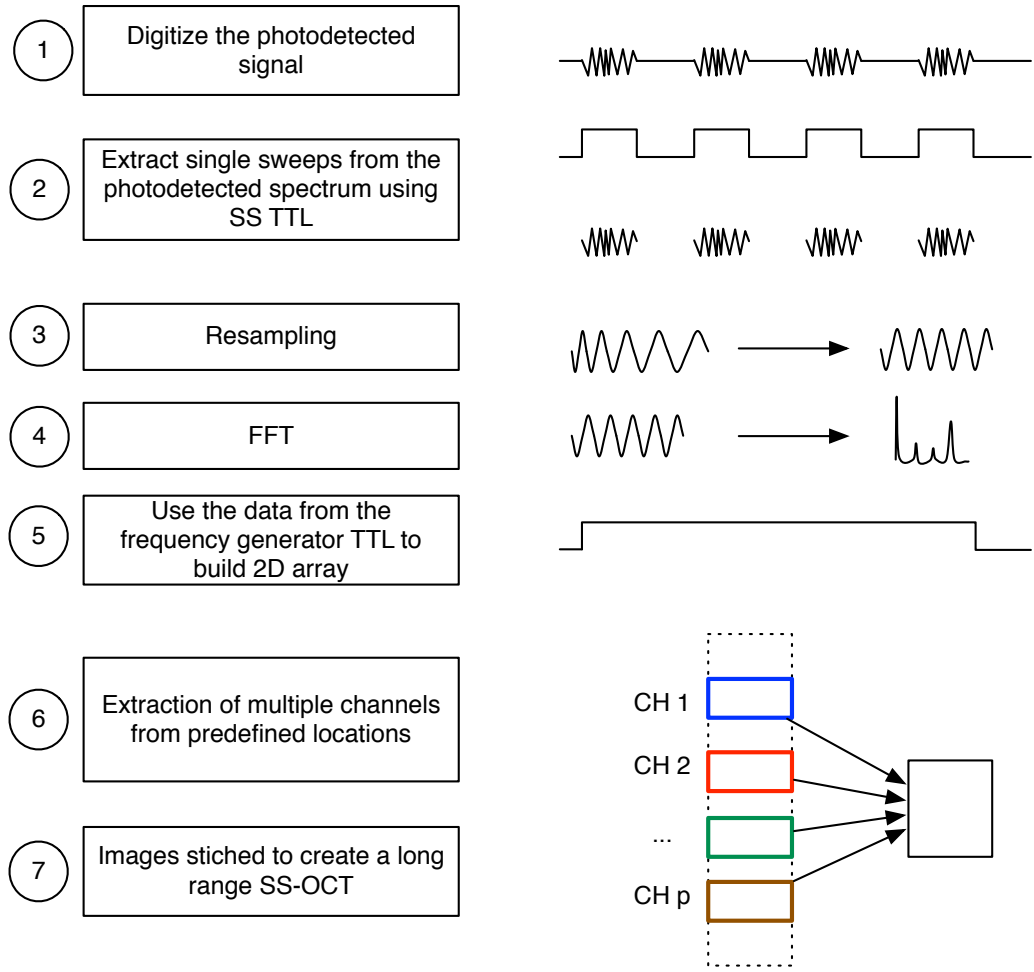


Figure 6.3: Data processing algorithm.

C_p , as illustrated in Fig.(6.3). Using the data provided by the frequency generator TTL signal, multiple A-scans are assembled into a continuous A-scan. Then the A-scans are assembled into a 2D array to produce a B-scan OCT image.

The frequency F_p of the photo-detected signal in each channel p , due to sweeping the optical frequency at a rate γ [Hz], for a given value of the OPD in the interferometer is:

$$F_p = \frac{\Delta k}{2\pi} * \gamma * [OPD - (p - 1) \delta] + C_p = S * [OPD - (p - 1) \delta] + C_p, \quad (6.2)$$

where Δk is the tuning bandwidth in wave numbers, C_p the carrier frequency imprinted by frequency shifting on each channel p and S is the conversion efficiency of the swept source interferometer, which converts OPD into RF frequency. Using the numerical values above, $S = 137$ kHz/mm. Using eq.(6.1) in eq.(6.2),

$$F_p = C_0 = S * OPD + (p - 1)[\Delta F - S\delta] \quad (6.3)$$

Equation (6.3), shows that different channels p determine different frequency for the photodetected signal depending on p .

6.2.4 Choice of differential delay δ

As shown by Eq.(6.3), the same OPD determines different frequency components in the photo-detected signal. In a different configuration applying a similar concept [13], the dependence on p was eliminated by making the last bracket in Eq.(6.3) zero. Here however, this cannot be achieved, given the need to separate the diffracted beams out of the AOD sufficiently laterally to allow introduction of different delay elements, as explained above, which justified the choice of a step increase from one carrier to the next of 9.376 MHz. With $S = 137$ kHz/mm and $\Delta F = 18.752$ MHz, these would determine a value δ_i too large for the differential step in OPD between channels of:

$$\delta_i = \frac{\Delta F}{S} = 20cm \quad (6.4)$$

The value of δ_i is too large in comparison with the axial range of each channel p . Measurement of the axial range of each channel p , as shown below leads to a range of a few mm. The differential delay between channels, δ , should be comparable with the maximum axial range achievable per channel in order to obtain, by combination of

channels, an overall constant sensitivity over an extended axial range. For instance, if a constant overall sensitivity is targeted, then sensitivity curves of spectrally adjacent channels should be shifted axially to each other until superposed over their FWHM points. This means a differential delay $\delta_c = \text{FWHM}$, where FWHM is the OPD value of the sensitivity curve versus depth where sensitivity drops to half. The measurements show that FWHM is approximately 2 mm. An alternative strategy would be to accept a non-constant sensitivity with depth, but over an extended range. This strategy is adapted here and the curves of sensitivity shifted laterally by twice more than the FWHM of each individual channel. Three slabs of glass giving a delay $\delta = 4.2$ mm were found which satisfy this requirement. With this value in Eq.(6.4), the last bracket cannot be made zero (as in [54]), as $\delta \ll \delta_i$. This means that each channel will occupy a restricted bandwidth in a spectral window around each carrier C_p , to a range determined by multiplying S with the axial range per channel, Δ . Using a value $\Delta = 2 - 4$ mm, this gives a bandwidth of plus minus $B \approx 0.5 - 1$ MHz (an exact calculation of bandwidth is presented in the next paragraph), much less than the frequency difference between adjacent carriers, $\Delta F = 18.7524$ MHz, as shown schematically in Fig.(6.4a). Fig.(6.4b) shows a simplified sketch of superposition of sensitivity profiles versus OPD, where $\delta \approx 2$ FWHM. This means that in order to obtain the final long range B-scan, each spectral window needs to be cropped from the photo-detected signal and shifted down in frequency by:

$$\delta F = (p - 1)[\Delta F - S\delta] \quad (6.5)$$

Using a differential delay of 4.2 mm, this gives

$$\delta F = (p - 1)(18.75 - 0.57) = (p - 1)18.18 \text{ MHz} \quad (6.6)$$

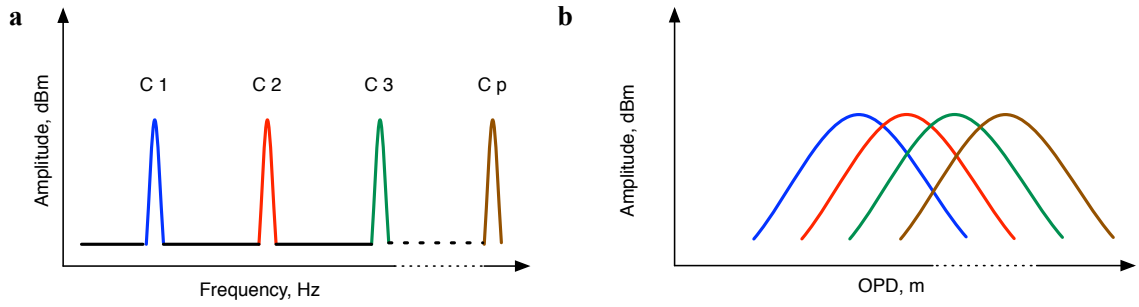


Figure 6.4: a: Sensitivity curves in each channel versus optical path difference, each centred around a different carrier frequency, C_p ; b: schematic illustration of combining the sensitivity of several channels versus OPD to obtain a more constant variation of sensitivity.

In this way, the frequency generated by each channel after being shifted becomes independent on p , giving in all cases the same value:

$$F_p = C_0 + S * OPD \quad (6.7)$$

The final long range B-scan of the curves in Fig.(6.4b) is obtained by adding the intensity values of each overlapping spectral window. The frequency values in the resulting long scan can be recalculated in OPD values using an equation derived from Eq.(6.5):

$$OPD = \frac{F_p - C_0}{S} \quad (6.8)$$

6.3 Results

6.3.1 Spectrum

Figure (6.5) shows the sensitivity curves for 4 delayed channels and the overall cumulated curve obtained by their summation. A multiple delay element consisting of

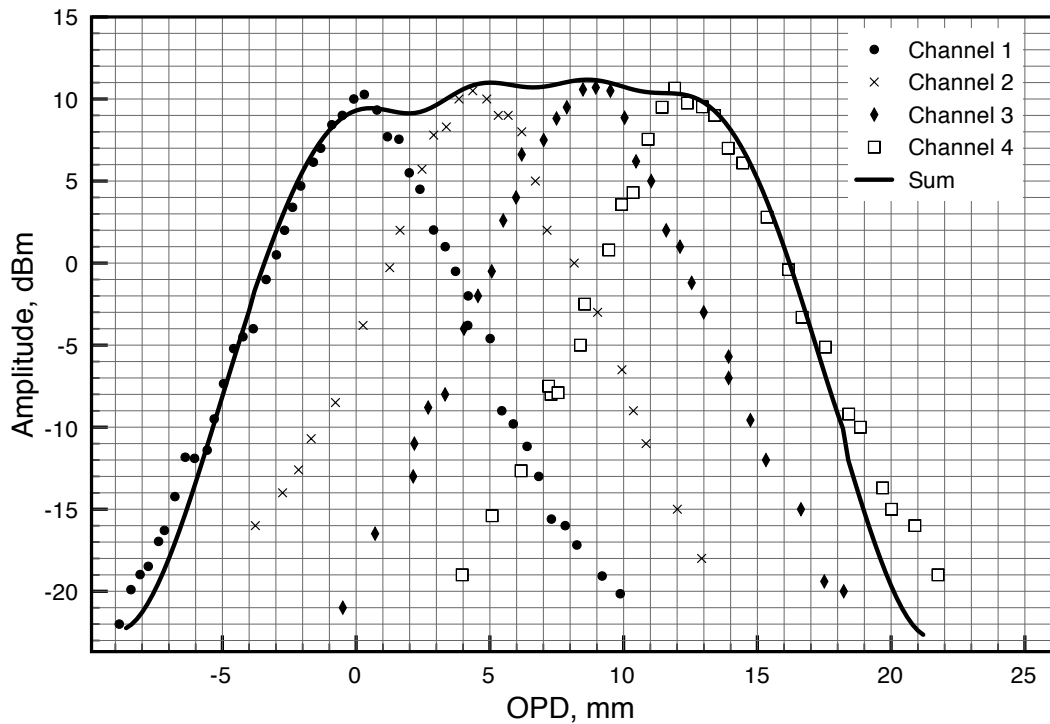


Figure 6.5: Sensitivity curve for $P = 4$ channels delayed relatively by $\delta = 4.2$ mm.

3 steps of $\delta = 4.2$ mm and a mirror as object are used in Fig.(6.1). The set carrier frequencies of the four channels for $OPD = 0$ is $f_1 = 10.494$ MHz, $f_2 = 19.87$ MHz, $f_3 = 29.246$ MHz and $f_4 = 38.622$ MHz. The multiple curves are raised by varying the reference arm length by moving the fibre launcher holding the MO4.

The data points for each sensitivity curve were measured using a *HP 8590A* spectrum analyser. The data collected were then fitted with a 4th order polynomial spline. A curve representing the long range A-Scan sensitivity was calculated as a sum of fitted curves for the single A-scan sensitivities.

Figure (6.5) shows that the sensitivity of each individual channel drops by more than 6 dB for an $OPD = 2$ mm away from the maximum, giving less than 4 mm usable range for a single channel. However, combining the data from all 4 carriers extends

the axial range of near constant sensitivity to more than 16 mm imaging range.

The regime of operation utilised here is of $P = 4$ channels with independent demodulation. The axial range is multiplied by an approximate factor of $P = 4$. If a swept source with 4 times longer coherence length was used, the bandwidth of the photodetector unit would have needed to accommodate a bandwidth of $4B$, where B can be evaluated by considering the maximum number of axial pixels within the axial range $\delta = 4.2$ mm. Using a bandwidth of 45 nm and a central wavelength of 850 nm, the number of pixels is $M = 594$. Using a scanning time of 0.5 ms, this gives a value $B = 1.19$ MHz. However, because here independent demodulation is implemented, the frequency of each carrier shifts from $C_p - B$ to $C_p + B$, i.e. a $2B$ bandwidth is needed on each channel. In total, the bandwidth is not P times larger, but $2P$ larger, ie $2PB = 8B$. This is a disadvantage of this configuration when compared to the swept source configuration with a 4 times longer coherence length employed in a conventional single path configuration.

However, if a denser packing of carriers is employed, according to Fig.(6.4b) and satisfying Eq.(6.4) as in [13], then the bandwidth needed is only PB .

6.3.2 Imaging

To illustrate the capability of the system to produce a long range B-scan, *in vitro* imaging of a formalin fixed C57BL/J mouse tissue sample was performed. A mouse head (Fig.(6.6e)) was positioned in front of OL and rotated in a way that the image would span through the major part of the sensitivity range. For this demonstration, the AODs were operated using a set of two frequencies C_1 and C_2 . Only two channels were used for imaging because the 8 mm sensitivity range (where variation of sensitivity due to roll-off is less than 6 dB) already exceeds the focal depth of the lens OL.

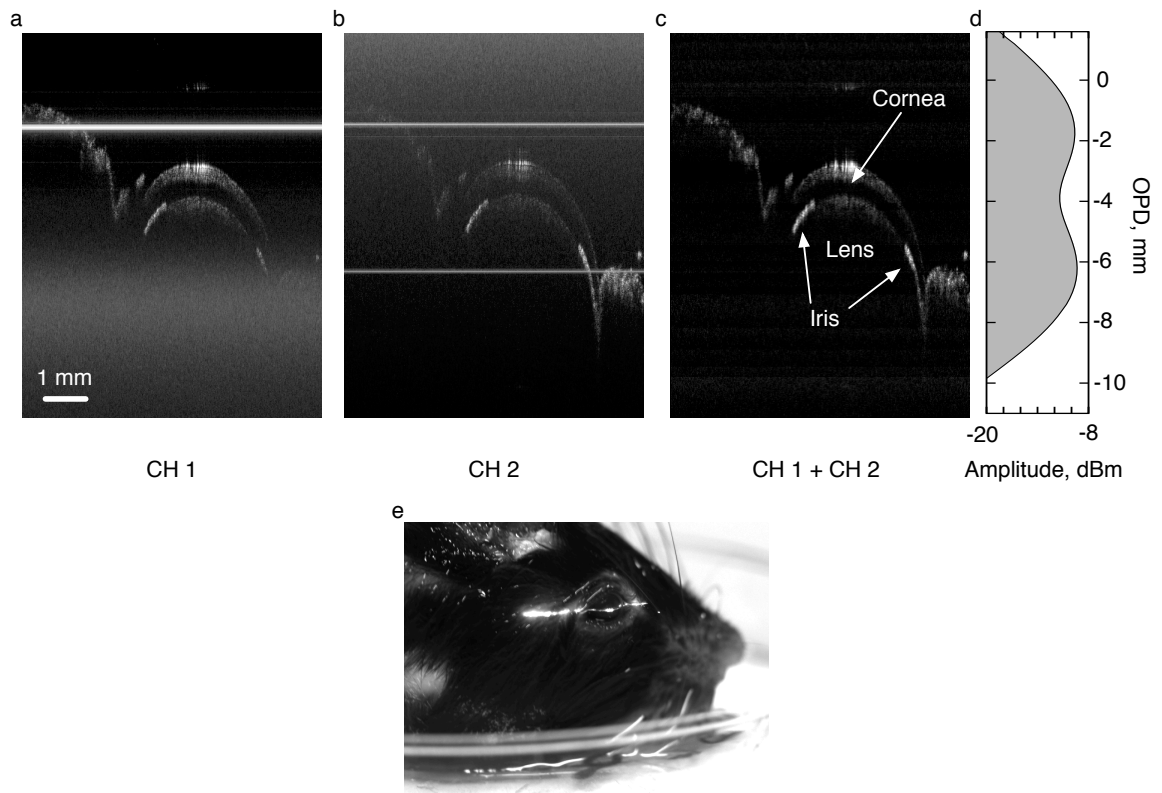


Figure 6.6: B-scan images of a tilted mouse head obtained with a long-range constant sensitivity SS-OCT system. a): Conventional B-scan carried by C_1 ; b): Conventional B-scan carried by C_2 ; c): A long range B-scan produced by the long range imaging software; d): experimentally measured sensitivity curve in air representing the system sensitivity variation as a function of reference OPD. The curve is positioned so that OPD in the graph corresponds to the OPD in a, b and c; e) a photo of the sample. The distance z in the object is $OPD/2$. Due to a long exposure time the scanning beam is visible as a white line across the eye and surrounding tissues.

Figure (6.6) shows two regular B-scans in Fig.(6.6a) and in Fig.(6.6b) that are obtained simultaneously. Each is delivered by a separate channel, CH1 and CH2 respectively, that are tuned on the carriers C_1 and C_2 respectively. The B-scans recorded from both channels are stitched by the imaging software to produce a long range B-scan, as presented in Fig.(6.6c).

Figures (6.6a) and (6.6b) illustrate an additional challenge raised by this configuration. The images present several white lines due to Bragg cell intermodulation prod-

ucts [44]. The lines are always present at the same spectral locations when the same set of RF frequencies is applied to the Bragg cells. They are present even without interference. Therefore, these lines are removed by acquiring reference images with no object present, which subsequently are used for background subtraction from the current images before stitching them to form the final image in Fig.(6.6c).

Possibly, the intensity of intermodulation peaks that are present in the RF spectrum may be significantly reduced by careful selection of acousto-optic materials and excitation RFs. The sensitivity versus OPD curve presented in Fig.(6.6d) is aligned to the images so that the graph represents the system sensitivity when acquiring the data from corresponding lines in the B-scan shown in Fig.(6.6c). The position of the scanning object beam, while acquiring the long range B-scan, is visible in Fig.(6.6e) as a line across the eye and surrounding tissues.

6.4 Discussion

The method implemented here is different from that reported in [13], where the differential delay between OCT channels was adjusted to match the value obtained from the difference of frequency between the channels divided by the conversion constant. S , between the OPD and the RF frequency generated when tuning the SS. Such a matching was not possible here as explained above. The method presented can be applied to up to $P = 8$ carriers, number limited here by the AOD drivers. However, in theory there should be a correlation between the compounded axial range achievable and the confocal axial range determined by the interface optics. This is why the images produced by two carriers only were compounded, as the confocal depth range limited by the interface optics was below 5 mm. Further research into long axial range OCT images should go hand in hand with methods to alleviate the limitation of sensitivity

due to the confocal gate. Such methods may involve for example digital focusing [86] or use of non-conventional objective lenses [159, 32, 87].

Frequency multiplexing could be combined with recently developed emerging swept source technologies such as micro-electro-mechanical systems (MEMs) tunable vertical cavity surface emitting lasers (VCSEL) [61] to offer an even further increased axial range. Such a long axial range may find applications in sensing, profiling or tracking of objects.

The method presented is especially suitable for the swept sources where increased tuning speed leads to diminished coherence length. In combining such sources with multiple path configurations, as described here, to increase the axial range of the OCT system beyond the limit set by the source coherence length, the bandwidth of the photodetection unit should also be taken into account. In this paper the principle of extending the axial range was demonstrated using a configuration with $P = 4$ delays in 4 independent channels and using a low rate tunable swept source, where the bandwidth due to tuning was small. If the line rate is increased to the frequency of fast commercially available swept sources of 200 kHz (100 times larger than the tuning rate used here), then a bandwidth $B = 119$ MHz would be needed. If non superposition of frequencies generated in the four channels is pursued, as illustrated in Fig.(6.4a) and employed here, this would require values for the frequency of the first 4 carriers of at least $f_1 = B$, $f_2 = f_1 + 2B$, $f_3 = f_2 + 2B$ and $f_4 = f_3 + 2B$, and so on, i.e. of at least 119, 337, 575 and 813 MHz respectively. The total photodetection bandwidth would be $2PB = 952$ MHz. However, if the swept source is faster, then the adjustment used in [13] becomes achievable, in which case a more compact frequency space is achievable, as implemented in [13]. In this case, the bandwidth required is exactly that for 4 times more axial pixels, i.e. 476 MHz only.

Swept sources with tuning frequencies of over 1 MHz [155] have also been reported,

which would require acousto-optic modulators and photodetecting units operating at frequencies over several GHz.

In our experiment, the set-up presented was optimised to offer a long sensitivity range at the expense of some allowed variation in sensitivity within the measurement range. The ripples in the overall sensitivity curve are less than 2 dB. Reduced rippling can be obtained by choosing a differential delay element δ so that the imaging channels would come even closer together, in terms of OPD, providing a relatively flat top sensitivity curve when combined, as suggested by the profile in Fig.(6.4b).

6.5 Conclusions

A system capable of performing long range SS-OCT imaging by combining several mirror terms free B-scans acquired simultaneously at different depths is presented. The system uses AOM frequency shifters to implement a multiple delay element with P delays in the reference arm, each traversed by a deflected beam at a different angle and with a different frequency shift as imprinted by the AOMs. The part of the reference beam traversing a particular delay in the multiple delay element is coded in the RF frequency of the photo-detected signal. In this way, A-scans and B-scans corresponding to different axial ranges can be identified.

The system is demonstrated for $P = 4$ delays which covers more than 17 mm OPD axial range measured at 6 dB, with a variation of less than 2 dB inside this axial range. The capability of producing long-range B-scan images was proven by imaging a part of a mouse head extended over 1 cm. The method presented acts on the interferometer configuration and not on the source and therefore can be combined with any method acting on the swept source.

Part II

Tracking

Chapter 7

Review of methods for sample tracking and image stabilisation in optical coherence tomography

7.1 Introduction

Stabilised images are advantageous in optical coherence tomography (OCT) because they can be used to extend the capabilities of various OCT imaging modalities. Motion artefact free OCT images are crucial for accurate segmentation and automated measurement of various biological structures in the images. Tracked retinal imaging is particularly desirable in targeted stimulus delivery and accurate delivery of therapeutic laser pulses to the retina. Stable images also allow averaging to be used to increase the visibility of tissue interfaces and improve signal to noise ratio. Over the years, various tracking modalities have been developed to stabilise the sequences of SLO and OCT images using post-processing or, more recently, to observe the sample

movements in real time and to reduce or eliminate motion artefacts using closed-loop tracked OCT imaging systems.

Even in fast OCT systems, the image quality in the retinal imaging is degraded by effects of involuntary movements (e.g. eye drifts and micro saccades [96, 130]), which cause motion artefacts and poor inter-frame registration. Eye stabilisation using fixation targets stabilises the eye to some extent only, in addition, fixation performance progressively decrease with age [108]. Although the tracking functionality is mostly sought after to stabilise retinal images, similar techniques are applicable to OCT modalities that require hand held scanning to compensate for sample movement and hand tremors.

Eye motion stabilisation can be easily achieved invasively, using suction cups, or the movement can be quantified accurately [69] by using a scleral search coils integrated into the contact lens [127, 22]. However, such stabilisation methods are uncomfortable to patients and may impede the imaging. Other methods such as dual Purkinje [23], infrared oculography [74], electrooculography [7], and camera based pupil tracking [131] are specifically designed to monitor the position of the anterior segment, therefore they cannot deliver an accurate estimate of the retinal position.

Generally, the current tracking methods can be divided into three categories: (1) Computational methods that employ post-processing algorithms to examine a sequences of images from the same location and then correct the images to remove motion artefacts. The majority of the algorithms in this category are patch-based cross-correlation techniques. Other algorithms employ probabilistic approaches [99] and multiple feature tracking Kanade-Lucas-Tomasi algorithm [83]. (2) Methods that use a fast imaging modality witness channel to monitor the sample movements and then apply the information to remove the motion artefacts from a slower, primary imaging channel either by post processing or in real time. (3) Closed loop tracking methods that lock

Cross-correlation based techniques

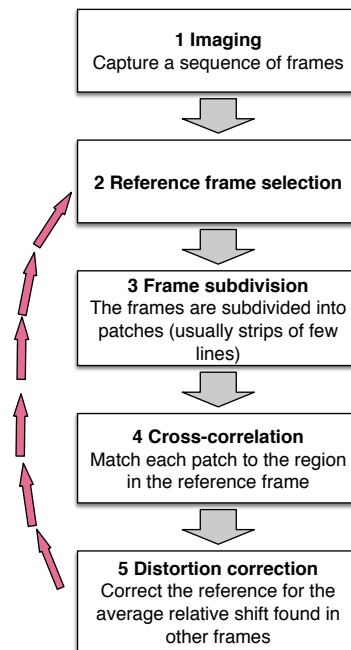


Figure 7.1: Most common motion artefact correction techniques are patch-based cross-correlation image registration algorithms. Such algorithms were shown to correct for both axial and lateral motion.

onto a small area of the sample using a witness modality such as a circular dithering beam reflectometer that monitors the lateral movement of a single reflective feature for movement correction, or a single high reflectivity peak in the A-scan to monitor the position of the maximum intensity point at constant distance for axial tracking. The methods in this category are usually the fastest and enable robust, hardware-based image stabilisation.

7.2 Computational post-processing video stabilisation methods

Probably the first use of cross-correlation to compensate motion during post-processing was demonstrated in TD-OCT, however only axial motion was tackled [147]. For lateral correction, motion was extracted using two dimensional correlation from series of *en-face* scans [142] and [143] by splitting the frames into several patches, and comparing the reference regions in each frame to other frames in the video and then correcting the regions in the reference frame by the average shift found from the similar regions in other frames, as depicted in Fig.(7.1). Such patch based cross-correlation image processing algorithms can be extended to reducing axial motion artefacts in TD-OCT of laterally stable samples [78]. The extended mathematical model describing cross-correlation based techniques is presented in [34]. Cross-correlation based techniques were applied to produce true 3D morphology of the retina [165]. As an improvement over traditional Fourier based cross-correlation techniques, map-seeking circuit algorithms [5] were explored as a way to improve the movement artefact correction in a sequence of SLO [152] and AOSLO images [94]and [97]. A majority of cross-correlation techniques require patches at least a couple lines thick to increase signal to noise ratio, however some work has been done to enhance saccadic motion correction by correcting on per-line basis [35].

Although patch-based cross-correlation techniques were originally intended to be used in post processing, with increasing computing power now available, some instruments, such as *Heidelberg Spectralis* [129] integrate the simplified algorithms to produce stabilised image at video rates, however some of the advanced motion correction techniques still rely on manual input. A demonstration where the cones were imaged over the period of time was presented in [72]. The experiment relied on a feature based

registration/de-warping algorithm scaling in the slow scan direction and shearing in the fast scan direction to ensure the match of manually selected features in the subsequent frames.

The Kanade-Lucas-Tomasi [138] Scale-Invariant Feature Transform [92] (KLT-SIFT) algorithm [83] is used for automated selection and tracking of stable features in a AOSLO video sequence. This algorithm is more robust in correcting scale and rotation distortions than patch-based cross-correlation algorithms. This was demonstrated to increase the image quality in small retinal vessel AOSLO imaging [84].

A probabilistic approach was investigated for compensation of axial shifts in SD-OCT [99], where the motion estimation is performed by treating the motion function as the energy function in a energy minimisation problem using a conditional random field (CRF) notation. The approach was demonstrated to significantly reduce the motion artefacts while preserving the geometry of the tissue. The method can work on a per single image basis.

7.3 Dithering reflectometer based real time tracking

Dithering beam reflectometer based tracking set-up [50, 40, 107, 47, 39] has been demonstrated to stabilise various retinal imaging modalities such as AOSLO [49], AO-TD-OCT [16], FDOCT [98] as well as multimodal systems [41, 48]. A tracking bandwidth up to 1 kHz was achieved depending on the tracker tuning conditions and gain. The closed-loop tracking based system is depicted in Fig.(7.2) It compensates for the lateral displacements of the retina by feeding the error signals generated by reflectometer to a pair of tracking galvoscaners, positioned at the eye centre of rotation conjugate plane.

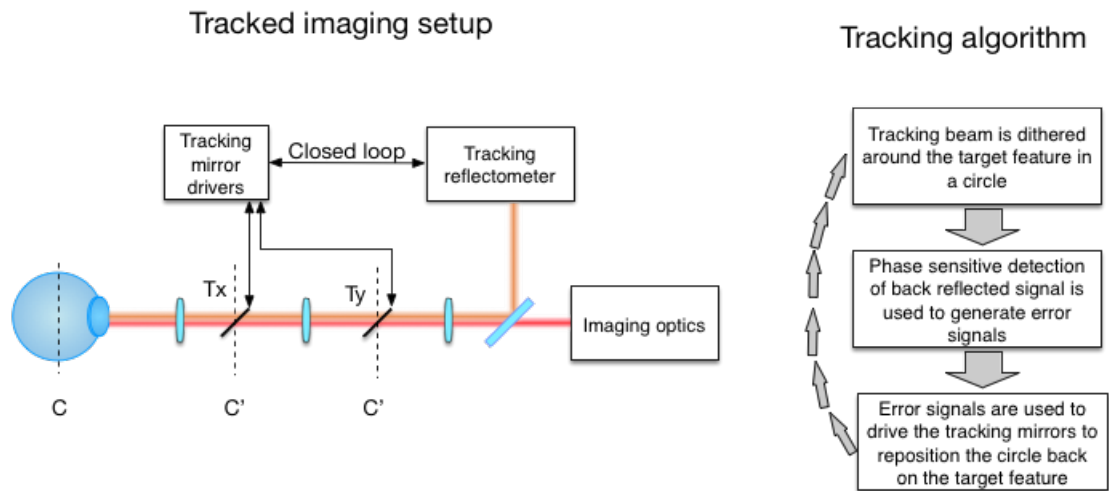


Figure 7.2: (left) The schematic of a dithering circle reflectometer guided tracking set-up and (right) tracking algorithm. C is the plane at center of rotation of the eye. C' indicate conjugate planes.

7.4 Post processing using a witness channel

One of the first methods that used an SLO witness channel [123] was employed to correct for smooth movements and abrupt micro-saccades in simultaneously acquired SD-OCT images. An SLO image is captured immediately after OCT acquisition and treated as distortion-free reference. The method corrects for the tremor and drift by using elastic image registration [109] and the dynamic time warping [132] is employed to correct for micro saccades. Unfortunately this method could correct only for transverse motion only.

In [17] a common path AO(SLO/OCT) system has been demonstrated, where the SLO and OCT systems share the vertical scanner, but have separate horizontal scanners, as depicted in Fig.(7.3). The shared vertical scanner operates as a fast (line) scanner for OCT and as a slow (frame) scanner for the SLO, as illustrated in Fig.(7.3 right). The retinal motion was estimated from a sequence of SLO images using methods described in [152] and [6]. The axial motion was estimated by translating adjacent B-scans to

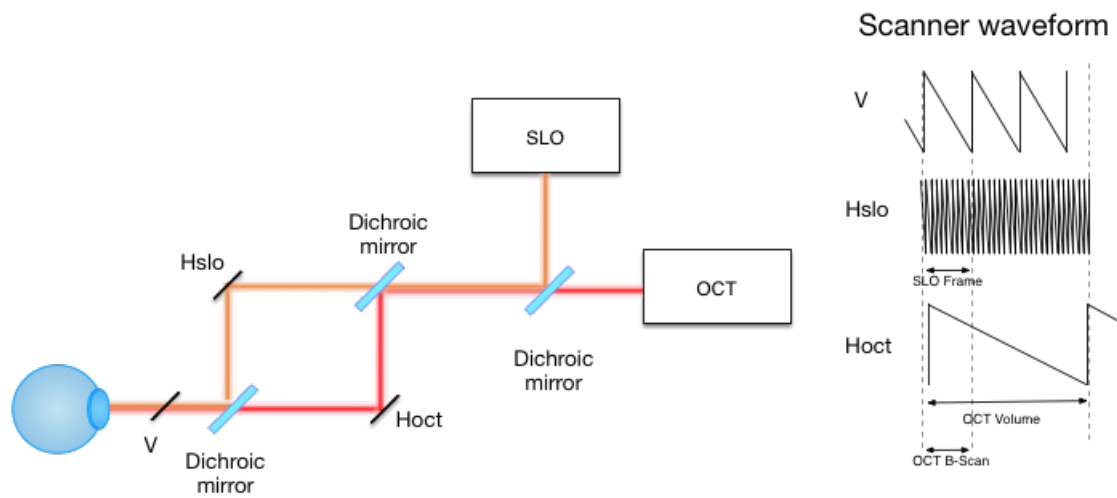


Figure 7.3: (Left) Schematic of a tracked OCT set-up employing fast SLO witness channel, where the vertical scanner is shared by both channels. (Right) Schematic of the waveforms that are used to drive the galvo-mirrors.

maximise their cross-correlation [148]. A similar method with improved gaze tracking is presented in [164].

An AO(SLO/OCT) system with pixel to pixel correspondence was used to perform 3D imaging human photoreceptors where AOSLO acts as the witness channel [38] for calculating translational movements with the method described in [142].

Early systems that employed orthogonal fast scans [165] and [122] used to obtain information on the retinal structure in the raster scanned 3D-OCT data along the slow-axis by acquiring additional B-scans along the slow axis and then used this as the reference retinal profile to realign the volume. This method registers axial position and corrects axial shifts in post-processing, but does not correct for transverse motion.

Advanced methods [73] employ orthogonal scanning to correct the movements in XYZ using at least two datasets (Xfast and Yfast) that were acquired first by running the X-scanner as a fast scanner and then by running the Y-scanner as a fast scanner as depicted in Fig.(7.4). Multiple orthogonal OCT volumes are acquired in succession

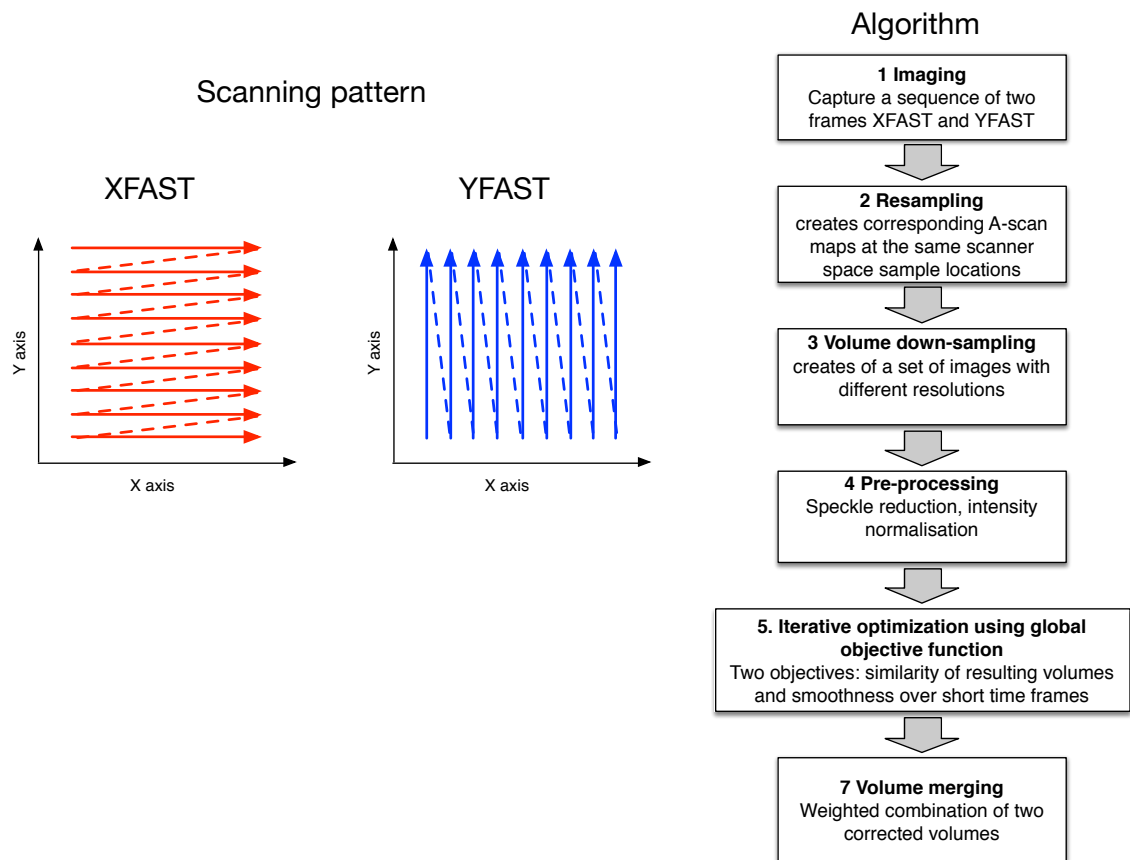


Figure 7.4: Orthogonal scanning based motion artefact mitigation method where at least one image is taken for each of the scenarios: Xfast, Yslow and Yfast, Xslow. (Left) scanning strategy. (Right) The image correction algorithm.

and displacement maps are generated by performing optimisation on a global objective function, which seeks to find similarity between the two volumes while penalising the abrupt shifts. The volumes are then undistorted and merged to obtain motion corrected image.

To compensate for the axial eye movements on the handheld SLO-OCT system [76], an algorithm was devised that uses pairs of Xfast and Yfast 3D OCT volumes and segmentation of the internal limiting membrane of the retina. The lateral shifts in the OCT image were corrected using displacement maps created by applying cross-correlation based techniques on the simultaneously registered SLO image.

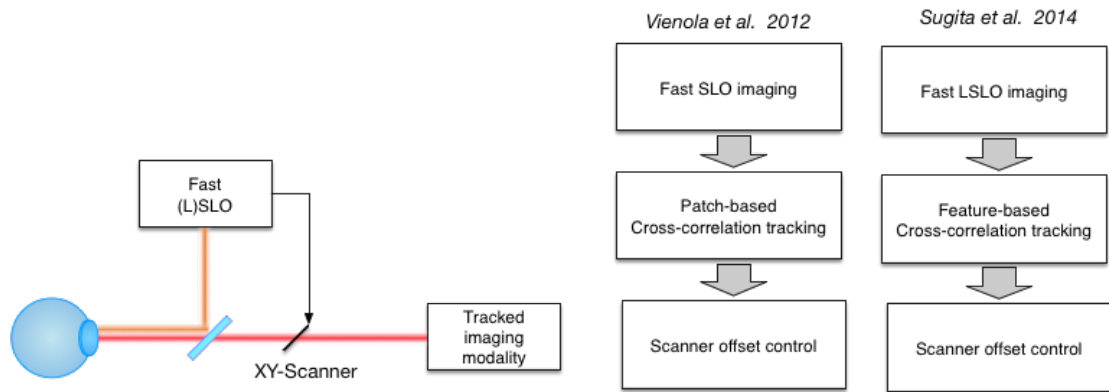


Figure 7.5: (Left) Schematic of a fast SLO witness channel based tracking imaging set-up. (Right) two different approaches for eye motion extraction and image correction.

7.5 Real time correction with fast witness channel

A fast SLO system was demonstrated to trace the eye movements in real time [137]. The SLO image consisting of 512x512 pixels was performed at 30 fps. Each image in the sequence was divided into 32 strips and each strip was then realigned to the reference frame using the methods described in [100, 6, 161]. This resulted in a 960 Hz position reporting rate, with a latency of 2.5 ± 0.5 msec. Initially eye motion feedback was used only to stabilise the image on the screen and to enable targeted stimulus delivery.

Figure (7.5) illustrates the operation principle of a system, where an SLO tracker was used to stabilise SS-OCT [151], and phase-stabilised optical frequency domain imaging (OFDI) system [12]. The error signals generated by the fast SLO system were added to the Waveform signals used to drive galvanometric scanners in the OCT set-up. The resulting OCT images had reduced distortions from drifts and micro saccades.

A similar approach employed 60 Hz LSLO witness channel to track retinal image feature and used the feedback to track slower PS-SDOCT [146]. The lateral shift information was obtained by comparing each LSLO image to the reference image using

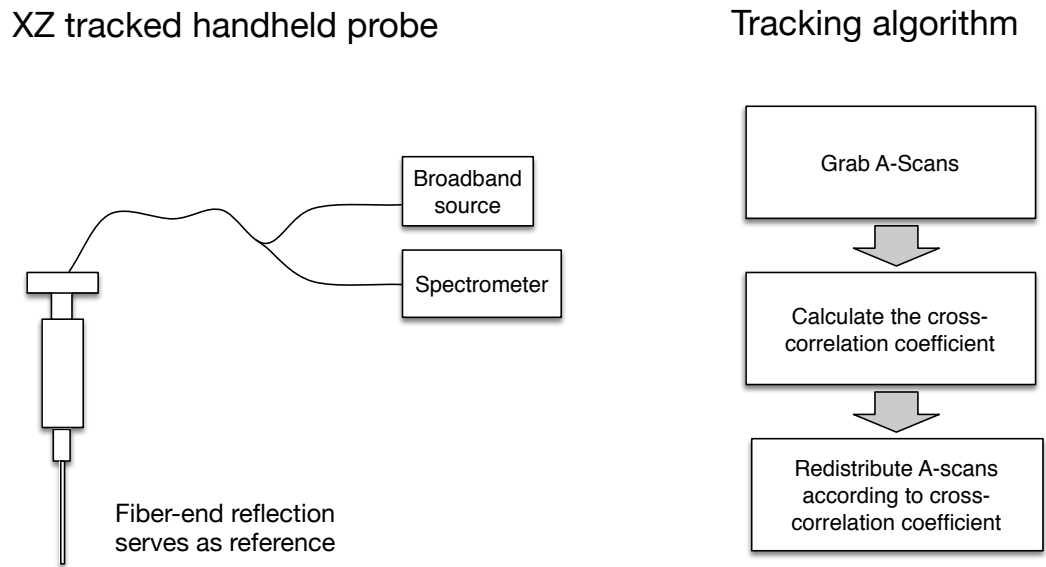


Figure 7.6: (Left) Handheld probe for the freehand sample scanning, (Right) simplified diagram of an image construction algorithm.

cross-correlation. The lateral retinal position feedback was provided after the acquisition of each LSLO frame at 60 Hz with a 10 ms latency.

7.6 Speckle informed tracking

Speckle de-correlation based motion detection techniques, have explored extensively in ultrasound [18] and [75] and were recently adopted in OCT [3] for estimation of the motion that occurs either from sample movement [90] or from the manual scanning of the probe [3, 88, 89].

Speckle de-correlation technique was demonstrated to permit real-time scanning motion correction in a freehand OCT probe as illustrated in Fig.(7.6). The system was demonstrated to reliably correct the displacements in X and Z planes with scanning speed limited by Nyquist sampling criterion, (to kHz A-scan imaging rate permitting the scanning at 420 mm/s) [88, 89]. The drawback of the aforementioned techniques

is that because they are working on a per-axial scan basis, they are not capable to determine the scan direction.

A fast, circularly scanned OCT beam was shown to enable the extraction of the motion speed and direction [91]. This method is based on the principle that each subsequent circular scan has two intersection points with the previous scan and in this way, probe/sample displacement can be monitored as long as the displacement is significantly slower than the speed of circular scanning.

Another approach for manually scanned OCT is Doppler-based lateral motion tracking [154]. The method estimates the lateral motion by analysing the phase changes between sequential A-scans however it was used to track in one dimension only and could not provide the orientation information.

7.7 Axial, hardware-based tracking

The majority of current active axial tracking systems employ a single point A-scan to monitor the axial position of the eye as depicted in Fig.(7.7). First demonstrations of such systems employed a spectral OCT A-scan to monitor the corneal reflection to provide the feedback to the fast voice coil which controlled the length of the reference arm in *en-face* TD-OCT set-up with the loop speed of 200 Hz [110] and [25]. The performance of such systems was limited by the inertia of the translation stage that was used for depth tracking. An improved version of this approach employed a rapid scanning optical delay line [66], which is based on a galvanometric mirror and diffraction grating. This allowed the speed of the tracking loop to increase up to 1 kHz [111, 38]. However the axial movements of the cornea do not always correspond to the retinal movements. Although corneal position tracking can be used for mitigation

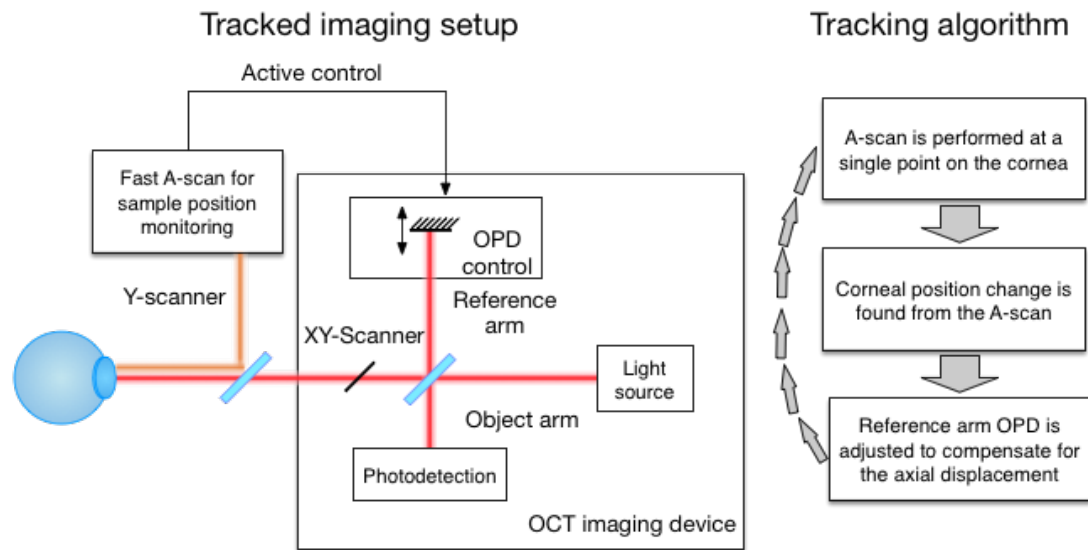


Figure 7.7: (Left) Single A-scan based axial tracking approach. Axial displacement of the eye is measured by observing the corneal reflection in the A-scan, the displacement can be compensated by changing length of the reference arm in the main OCT imaging system. (Right) Tracking algorithm.

of certain movements such as head position shifts, it cannot reliably compensate for heartbeat induced low amplitude retinal movements.

Alternative approaches of axial tracking have been used to compensate for hand tremors and track surface topology when using a handheld manual-scanning OCT probe [57]. Active motion compensation has been performed by peak detection in the A-scan at 460 Hz RMS error of $2.93 \mu\text{m}$. The error signals generated by peak detection were used to drive the motor controlling the axial position of the probe. The peak-detection based motion compensation algorithm results in distorted topology information. To compensate for this drawback, topology correction was performed in post-processing using a cross-correlation maximisation-based shift correction algorithm.

In addition to tracking position, methods are also needed to track the velocity of a sample. Tracking instantaneous velocity was demonstrated by a heterodyne Doppler interferometer method in catheter-based optical frequency domain imaging [46]. Mo-

tion of the sample was acquired by measuring the frequency shift of the backscattered light, caused by the Doppler effect.

7.8 Conclusion

In this review, the state of the art of sample tracking algorithms have been reviewed with a particular focus on their compatibility with the retinal tracking. As it was demonstrated there are many ways of distinguishing and grouping the methods for OCT/SLO image stabilisation. In this review we have followed the logic where the tracking methods were mentioned starting with the slowest tracking speed, such as post-processing based image stabilisation. the review continued with faster tracking methods such as to fast witness channel based and single feature monitoring.

The image post processing based methods were historically the first methods to provide stabilisation for image sequences. As easily available computing power increased, it became possible to adapt and employ post processing based methods on the images provided by the fast witness channel to achieve video rate active stabilisation for the primary imaging modality (usually OCT).

Currently the fastest methods for image stabilisation are the methods that observe a position single feature in real time, such as dithering circle reflectometer to track lateral movements developed by PSI and single A-scan based axial displacement tracker.

Chapter 8

Closed loop tracked Doppler optical coherence tomography based heart monitor for the *Drosophila melanogaster* larvae

8.1 Introduction

The *Drosophila melanogaster* can serve as a model for the cardiovascular systems of the vertebrates, including humans [20, 158]. However it remains poorly understood because of the lack of proper tools for assessing the cardiovascular system dynamics of small animal embryos [62]. Invasive methods such as multi-electrode array systems [104] and multiple sensor electrocardiography [140] are being replaced by non-invasive contactless optical monitoring methods, that allow accurate *in vivo* observations [105]. Two main types of time-resolved optical based measurements can

be distinguished: motion mode (M-mode) recording based methods and Doppler frequency shift based methods.

The M-mode monitoring methods were originally developed for use in conjunction with ultrasound instruments in echocardiography [37]. For *Drosophila* imaging such methods rely on data provided either by a high speed camera [102, 103] or by an OCT setup [149, 81, 45, 85], to measure cardiac functions. Such methods rely on recording series of two-dimensional images and subsequently mapping and measuring the heart diameter over time to calculate various parameters such as heart rate, heart period, diastolic and systolic intervals, and end-diastolic and end-systolic areas [45]. M-mode recording based methods reflect volumetric blood flow.

Doppler sensing methods provide further information about blood velocity by measuring the motion induced frequency shift. Swept source based Doppler SS-OCT imaging setup [21] can provide cross-section images at the video rates. However the time domain OCT can provide higher frequency sampling rates [95] that are beneficial for either instantaneous audio feedback [93] or for the signal visualisation in the Fourier space. By observing only a single volumetric pixel in the heart, TD-OCT based Doppler monitoring setups provide a continuous heartbeat data, however in practice this is possible only for short periods of time due to larva crawling away from the probe beam. So far, only two solutions have been implemented to prevent larva from moving and allow such measurements to be performed *in vivo*: anaesthetising the larva or restricting its movements by applying glue or physical restrains to it.

However, several studies have emphasised that that stress caused by various factors can alter the cardiovascular dynamics of larvae [136]. It was demonstrated that the use of the anaesthetising chemical agents such as CO₂ gas or *Flynap* anaesthetic mixture, affects the heart function of the *Drosophila* and cause an irregular heartbeat [149]. On the other hand, the physical restraining methods such as gluing or other-

wise physically restricting the larvae movements may as well induce stress and alter the dynamics of the cardiovascular system, as opposed to stress free environment. Therefore there is an interest in devising methods that allow monitoring of the unrestrained and non-anaesthetized larvae, to ensure collection of data with enhanced accuracy in terms of the heart mechanism.

In this paper we investigate a system where a closed-loop tracking [40] is applied for Doppler based OCT sensing. Such a setup enables long term *in vivo* monitoring of a single point in the heart of a *Drosophila* larva. With no need of anaesthesia or physical restraint, the proposed method reduces the stress caused to the animal and allows recording of Doppler data less affected by movement.

8.2 Experimental setup

The schematic diagram of the OCT based tracked Doppler monitoring system is depicted in Fig.(8.1).

For the Doppler sensing we have used a compound source BBS composed of an SLD (*Superlum SLD-531*) and a semiconductor optical gain and amplifier module (*Superlum SOA-522*). The compound source has the total power of 26 mW and an optical bandwidth of 35 nm with a central wavelength of 1050 nm.

The light from the source is injected into a fiber coupler array (*AFW, FOBCM-2-1064-50-20-B-SSSS-2*) as depicted in Fig.(8.1). 20% of the total optical power is sent to the object arm and 80% of the power is diverted to the reference arm. In the reference arm, the light is collimated and launched into free space using a launcher L (*New focus, 5726-B-H, 10x*) and injected back into the fibre array to interfere with the object light. The length of the object arm is adjusted to match the round trip in the object arm, of

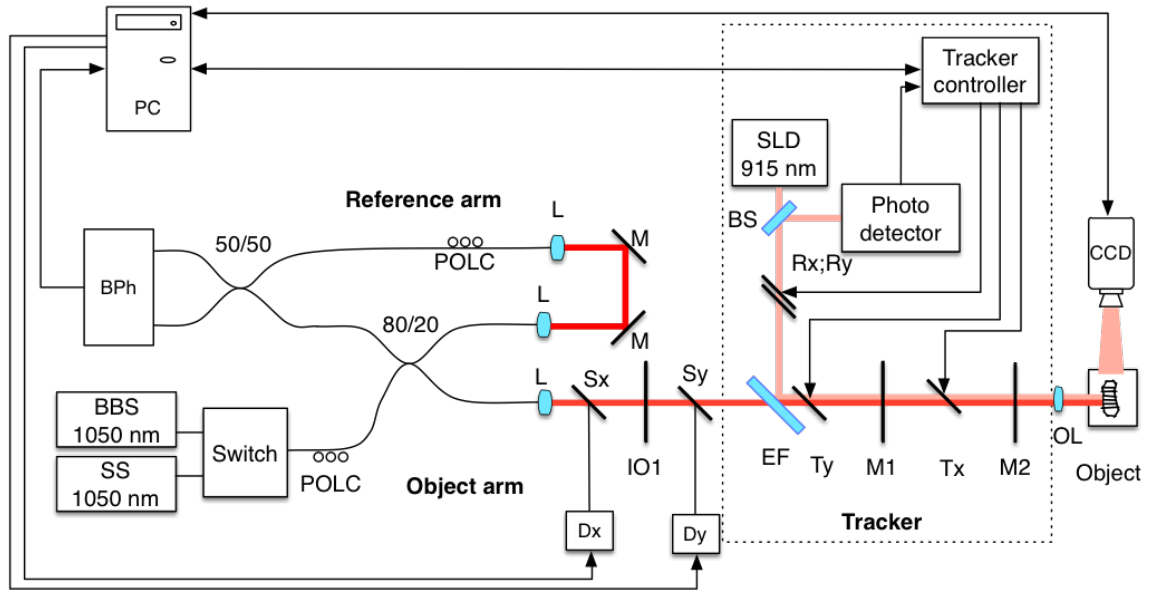


Figure 8.1: Schematic layout of tracked Doppler OCT monitor. BBS: Broadband light source; SS: swept source; S_X , S_Y : galvanometer scanners equipped with mirrors to steer the Doppler beam along X and Y direction; T_X , T_Y : galvanometer scanners equipped with mirrors to track the object along X and Y direction; R_X , R_Y : pair of resonant scanners; BS: mirror with thru-hole beam splitter; EF: edge filter; M1, M2: concave mirrors; OL: objective lens, POLC: polarisation controller; L: launcher/collimator; M: flat folding mirror; IO1: mirror based interf optics to re-image S_X onto S_Y . BPh: balanced photodetector; CCD: a full field CCD camera for the object position monitoring.

~ 6.4 m. A pinhole is used to control the total optical power in the reference arm.

In the object arm the light is launched with a similar launcher L onto a mirror mounted on the galvo-scanner S_X . The galvo-scanner S_X is re-imaged onto a second mirror mounted on the galvo-scanner S_Y . This pair of scanners is used to either steer the Doppler beam across the object plane, or to create the line and frame scans when performing OCT imaging. The OCT beam is then combined with a tracking beam using an edge filter EF (*Andover Corporation, 100FL07-50S*) and re-imaged onto an objective lens OL (*Melles Griot, f = 22.5 mm*), through the tracker optics (tracker optical layout will be described further in the text). The light backscattered from the object is returned back through the object arm and re-injected into the fibre array

to interfere with the reference light. The signal is photodetected using a 125 kHz balanced photodetector (*Nirvana model 2007*). The signal can either be recorded using a PC or sent through the amplifier to the loudspeakers to provide instantaneous audio feedback to the user.

A superluminescent diode with a centre wavelength at 915 nm is used as a light source for the tracker. The light is launched onto the closely positioned resonant scanners R_X and R_Y . The resonant scanners are dithered in synchronism, at 16kHz, with a phase difference of 90 degrees, to create a toroidal shaped beam. The tracking beam is combined with an OCT beam using an edge filter EF and launched onto the tracking galvoscaner T_Y mirror M_Y (mirrors M_X and M_Y are not shown in the diagram). The mirror M_Y is then re-imaged onto the mirror M_X fixed to the scanner T_X , and the lens OL using the large concave $f = 152$ mm spherical mirrors (*Edmund optics, 32-837*). The construction and the principles of operation of the tracker was already described in other papers [40, 47].

For a swept source based OCT imaging, the source is replaced with an *Axsun 1060* nm swept source SS and as photodetector, a 200 MHz *Thorlabs PDB460C* balanced photodetector is used for the detection.

8.3 System characterisation using a vibrating phantom

To test the impact of tracking on the Doppler signal frequency, we assembled a vibrating phantom, made from a two-dimensional vibrator, using a magnetic coil based laser pickup mechanism from a CD drive. A paper target with features that the tracker can easily lock onto (bright circles on the dark background), was attached to the vibrator, as depicted in Fig.(8.2). The vibrator can be used to independently vary the position

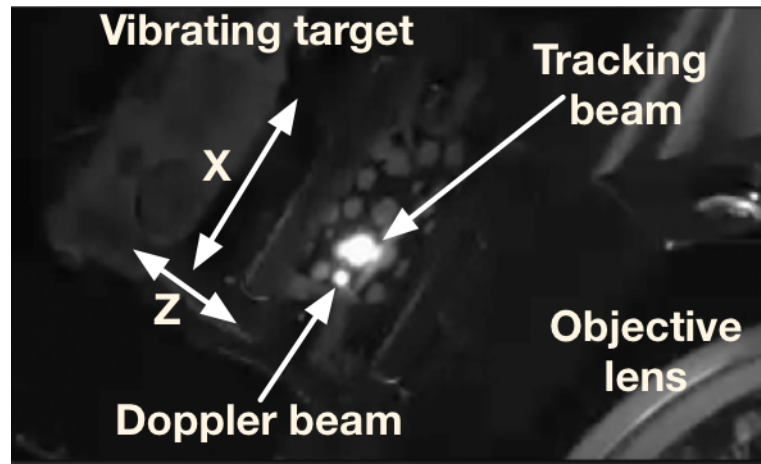


Figure 8.2: Photograph showing the vibrating target mounted in front of the objective lens, OL. The tracking and the Doppler beams are visible as bright white spots on a target.

of the reflecting target in both, lateral and axial, direction by applying voltage on two sets of coils. The vibrator with the paper target was then mounted in the object plane in such a way as to ensure that the flat paper sits almost perpendicularly to the optical axis of the system.

The two sets of the coils in the vibrator were then connected to two *Stanford research systems DS335* function generators for independent control of the object position in axial and lateral directions.

In Fig.(8.3) we present the recorded signal for different experimental conditions. In cases c and d the object was vibrated laterally at 5Hz sinusoidal frequency, to simulate the axial movement of the target, generating the useful Doppler signal to be measured. A lateral oscillation was applied, representing the disturbance due to random lateral movement, whose effect is aimed to be attenuated by tracking. This was simulated by applying a sinusoidal signal at 5 Hz, that was either turned on (c and d) or off (a and b). The representative 10 second recordings of the photodetected signal were performed by connecting the output from the balanced photodetector to a PC microphone input.

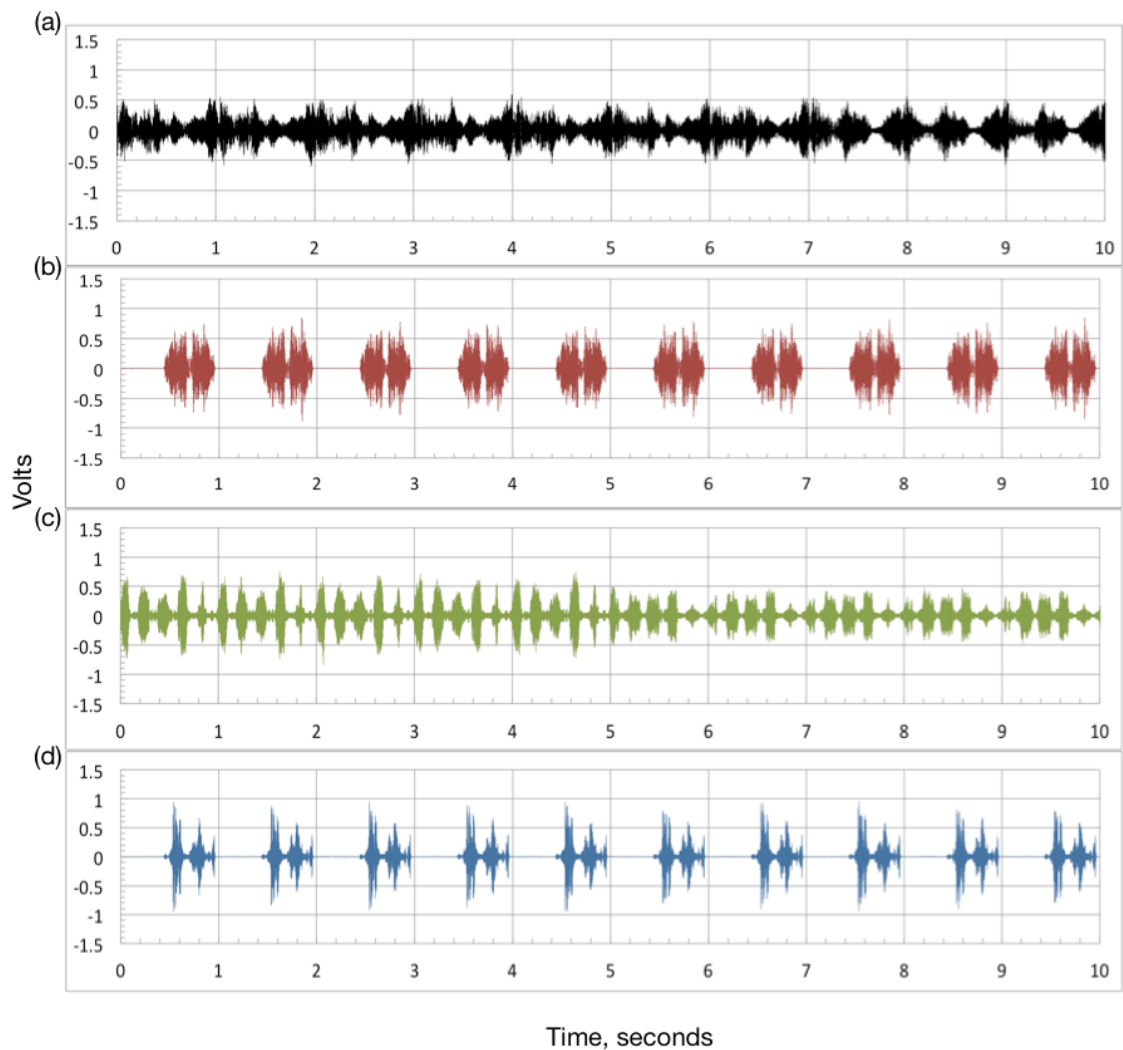


Figure 8.3: Oscilloscope trace of the Doppler signal acquired from a phantom under four different conditions. In all cases, the paper target was sinusoidally oscillated at 1 Hz in the lateral plane. The target was vibrated sinusoidally axially at 5 Hz in c and d and no axial vibration was applied in a and b. Tracking was ON in a and c and OFF in b and d.

The signal was sampled at 44.1 kHz, 16 bits per sample and recorded using a lossless waveform file format (wav).

As expected, the main improvement in the signal quality comes from the fact that the tracking ensures enhanced continuity in the periodicity of the photodetected signal. From Fig.(8.3), it is clear that the tracking enables continuous monitoring of the

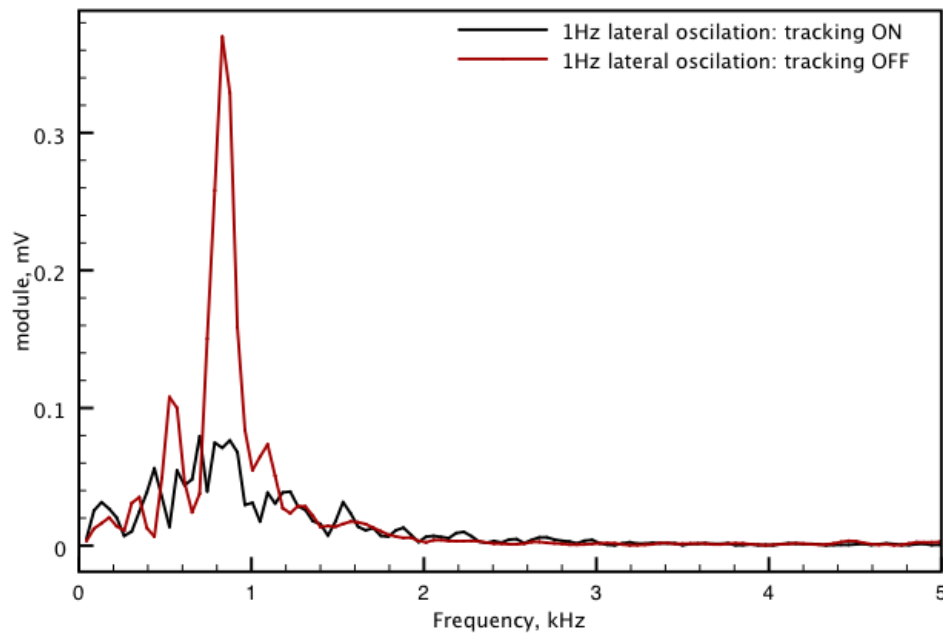


Figure 8.4: Frequency analysis of a typical frequency content of photodetected Doppler signal with and without tracking. In both cases the paper target was oscillating in a lateral plane at 1 Hz frequency. No axial vibration was applied.

Doppler shift originating from a single point in the object and record a continuous signal from a chosen point. In cases presented in Fig.(8.3a) and Fig.(8.3c), the tracking is turned on. This results in continuous recording of a Doppler signal as opposed to the cases presented in Fig.(8.3b) and Fig.(8.3d) where the signal is interrupted due to the object shifting laterally away from the coherence gated Doppler beam sensitivity range.

In the cases presented in Fig.(8.3c) and Fig.(8.3d), the paper target was vibrated laterally. Here, again once the tracker locked onto a suitable feature, a regular Doppler signal was recorded as Fig.(8.3c) shows. Once the tracker was deactivated, due to object movement some vibration cycles were not recorded due to the signal interruptions caused by the object movement.

Additionally, we have examined the frequency contents of a photodetected signal in

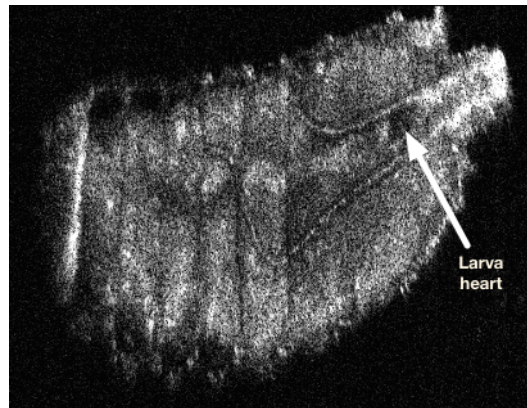


Figure 8.5: *En face* OCT slice of a *Drosophila* larva. The *en face* slice was extracted from a 3D volume acquired with the SS-OCT imaging system. The heart of the larva is located at the posterior part of the body.

cases, where object was oscillating in the lateral plane. A typical frequency spectrum is presented in Fig.(8.4). The spectrum was obtained by calculating a fast Fourier transform (FFT) of a short sample from a recorded signal (512 data points corresponding to 11.6 milliseconds). After comparing the frequency spectrum of the signal obtained either with or without tracking, it is visible that the tracking dampens the peak that is otherwise well defined in the non-tracked Doppler recording. Furthermore we notice that the tracking significantly reduces the stray signal affecting the Doppler signal monitoring beam scanning across the paper object surface. With active tracking, the only remaining noise is due to the OPD changes induced by the tracked object beam movement across the objective lens and tracker optics.

8.4 Tracked monitoring of the *Drosophila* larva

For the experiments the larva was extracted from the feeding container and gently positioned on the glass plate with a thin layer of food applied to cover a small patch on a plate. The plate was then positioned in front of objective lens ensuring that the



Figure 8.6: Images of the *Drosophila* larva illuminated by the tracking beam, collected using the camera C. As the larva moves around the glass slide it remains illuminated by the tracking beam locked onto a feature just above its heart.

patch of food with the larva sit in the centre of the field of view of the objective OL. Then the larva was left to relax about a minute before any measurements were taken to ensure that it positions itself with the mouth down to reach the food and the dorsal side up. Once the tracker is reliably locked onto a suitable feature, the Doppler beam position is fine-tuned by applying offsets to the X and Y beam steering mirrors and the coherence gate is adjusted by changing the length of the reference arm.

To allow continuous monitoring of the cardiac dynamics it is important to ensure that the tracker is locked on a feature just above the heart chamber. In this way, even as the larva rotates on the image plane due to its movement, as illustrated in Fig.(8.6), the Doppler beam remains positioned on the heart and provides uninterrupted measurement.

The current technology allows lateral tracking only. Therefore if the larva moves the monitored part of its body axially, the heart chamber moves away from the available sensitivity range and the signal is interrupted. Additionally, such movements may result in losing the lock on the tracked feature. We have found that the larva tends not to perform such movements when the thin layer of food is provided on the microscope slide. We have observed that it prefers to remain on the patch of food provided, therefore a layer of food as well reduces the likelihood of larva crawling away, out of the instrument field of view.

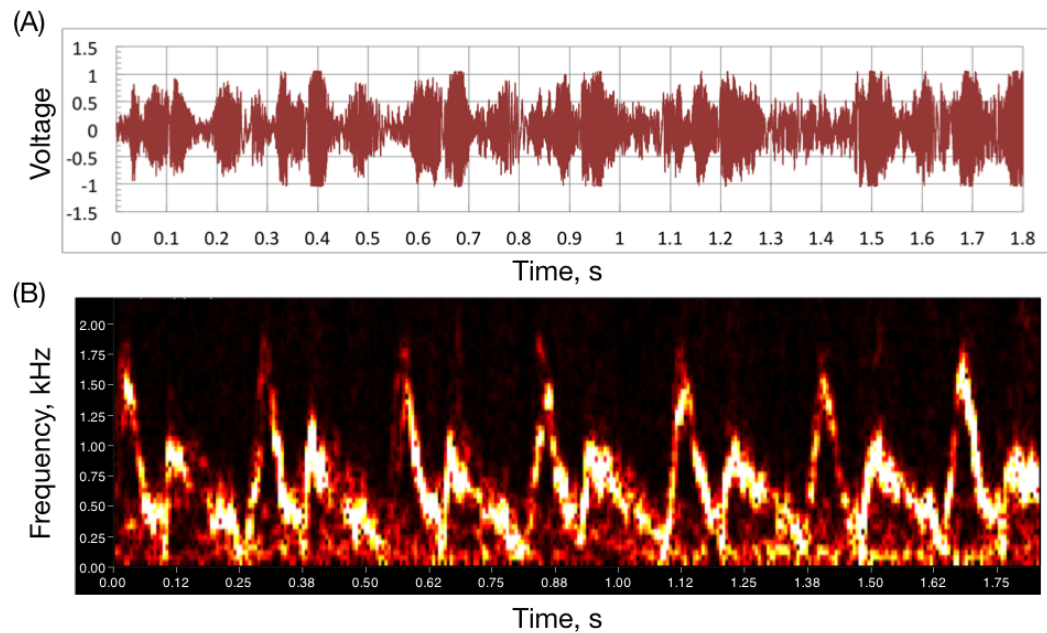


Figure 8.7: Signal from the Doppler OCT based larval heart rate monitor. (A) Typical recording of the photodetected signal using the BBS and the low frequency photodetector, displaying rapid oscillations due to the Doppler signal from the *Drosophila* larva heart. (B) Long sonogram of the Doppler recording obtained by performing FFT on several 1024 points sliding windows with 256 points offset. Signal was apodized using a Hanning window.

To facilitate the locking on fine features, we have reduced the size of the tracking beam circle to a diameter of ~ 0.5 mm, by reducing the amplitude of signals applied to the two resonant scanners, R_X , R_Y . Additionally, we have adjusted the gain settings of the tracker software to ensure that the tracker locks onto the dark features in the bright background, as this proved to provide more reliable lock.

We have recorded the Doppler signal from the larva heart using the same procedure that was used to record the signal from the phantom as described in Section 3. Figure (8.7a) represents a typical 1.8 second excerpt from the continuous 10 minute recording. We have visualised the frequency content of the signal using a sonogram depicted in Fig.(8.7b). The sonogram was constructed by calculating a FFT of the recorded signal, using several 1024 points long sliding windows with Hanning apodization. An

offset of 256 points was used between each successive window measurement.

The long term recording provides an almost uninterrupted recording of the cardiac dynamics of the *Drosophila* larvae. There are some occasional short spikes caused by what authors believe are a minor axial movements of the larva body or minor changes in the tracker lock-in position on the larval body. Nevertheless, the heartbeat can be monitored and analysed throughout the whole length of the recording.

The most common factors that can cause the loss of the lock-in and interrupt the recording is (1) larva leaving the field of view of the system and (2) large movements due to larva lifting and tilting its posterior body part by more than several degrees.

8.5 Discussion and conclusions

The signal obtained from the Doppler OCT system can be used for both qualitative and quantitative real time observations of the cardiac dynamics. The sonogram of a signal can be measured in real time, therefore it allows to observe the response of the larva to changing conditions.

The functionality of the set-up can be extended by combining it with the frequency multiplexer described in the first part of this thesis. In this way, simultaneous measurements of several axial points can be observed in real time and recorded.

One of the remaining challenges is the loss of signal due to the larva shifting axially, away from the coherence gated sensitivity range. This can be alleviated by applying similar strategy as in [24] and including an active axial tracking module to observe the axial position of the object and adjust the length of the reference arm proportionally to maintain the continuous signal.

Future work includes adding the simultaneous SS-OCT imaging functionality to simultaneously provide B-scans and enable M-mode recording of the larval heart in addition to Doppler monitoring. This could be achieved by combining the existing Doppler imaging set-up with an OCT system operating at a different wavelength, such as 1550. Such a set-up could be implemented by combining the Doppler and imaging channels using a dichroic filter at the back-end of the tracker.

Chapter 9

Conclusions

9.1 Thesis achievements

In this thesis we have presented several methods and devices that facilitate the collection of multiple OCT parameters or improve the reliability of OCT data. A first set of experimental set-ups presented here was based on a novel method for multiplexing in the OCT. The multiplexing approach presented relies on dividing the light in the reference arm into several frequency encoded spatially separated beams and recombining them again so that they could be injected into a single mode fibre. The recombined beams are encoded on different carrier frequencies. The reference light is interfered with the object light and several parallel imaging channels are separated on different radio frequency bands in the spectrum of the photodetected signal, just like television channels. Our method allows inducing optical delays and modifying the polarisation state for each reference channel independently. All channels can be recorded simultaneously. We have explored the capabilities of the multiplexing method by using it in conjunction with three OCT modalities: time domain OCT, polarisation sensitive OCT

and swept source OCT.

The time domain OCT set-up employed the multiplexer to deliver up to eight parallel imaging channels for simultaneous *en face* imaging at different depths. Using the system we have imaged a woodlouse, *Armadillidium vulgare*, at five different depths. Furthermore, we have exploited the capability provided by the method, which allows adjusting the intensity of individual reference channels to equalise the brightness of all five channels. We have increased the reference light intensity for the channels that deliver data from deeper object layers to partially compensate for attenuation due to scattering in the object arm, and we have reduced the reference power for channels that are imaging superficial layers where too strong signal would otherwise lead to saturation of the photo detector.

The polarisation sensitive time domain OCT setup employed the multiplexer to deliver polarisation insensitive images as well as images visualising the birefringence of an object. In the reference arm we have employed the multiplexer to produce two orthogonally polarised beams. After interfering with the object arm, the signal was photodetected, and two polarisation sensitive signals were recorded from the photodetected spectrum. The multiplexer ensured that the signal in both polarisation sensitive channels is acquired at the same time from the same location in the object. This is important for accurate birefringence and polarisation insensitive images, as simultaneous acquisition reduces the effect of object movements. The set-up was employed to reveal the loss of birefringence in a thermally damaged muscle tissue. We believe that the future work will allow more than two channels in the multiplexer to obtain additional polarisation information so that Jones matrix or even Muller matrix could be reconstructed.

In chapter 3 we have provided designs for the systems that could provide simultaneous time domain polarisation sensitive imaging from several depths.

Finally, we have integrated the multiplexer into a swept source based OCT set-up to extend the sensitivity range. We have demonstrated, that by optically delaying different channels in the reference arm, the delay values can be adjusted so that the sensitivity of each subsequent channel picks up exactly at the point where the sensitivity of previous channel begins to drop. In this way, the overall sensitivity range can be extended several times. We applied this feature to extend the sensitivity range in B-scan imaging by combining two simultaneous B-scans from a mouse head sample.

Another direction of research focused on improving the accuracy of OCT data acquired from moving targets. Several tracking modalities have been recently developed to compensate for the distortion of images from the eye fundus due to the eye movement. A tracking solution for the eye was made functional and tested on the eye as well as in microscopy. We have demonstrated a closed loop tracking based set up that uses low coherence interferometry to monitor the cardiac dynamics of a *Drosophila melanogaster* embryo. We have employed a low coherence interferometer based Doppler monitoring set-up in conjunction with a closed loop optical tracker to ensure a continuous monitoring of a single spot in the heart of an embryo. We have shown that once the tracker was locked onto an area above the heart, the Doppler monitoring beam could be independently positioned to record the data from a point of interest. As the larva crawled around the set up field of view, the closed loop tracking system secured a stationary beam in respect to the larva, compensating for its lateral movements. This is the first time such a solution developed for the eye tracking is applied to a microscopy problem to serve biosciences interests. As the monitoring beam is almost stationary on the same part of the moving larvae, the system could continuously deliver data over extended periods of time.

9.2 Future work

As a general overview, this thesis proposed two novel approaches to extend the capabilities of OCT in imaging as well as of low coherence interferometry applied to sensing. The improvements of functionality were achieved either via simultaneous data collection in several channels or via assistive closed loop tracking systems to reduce the distorting effects of object movement. Several possible avenues for future research or applications have been commented in each chapter. There is however room for further experimental as well as theoretical avenues. Here we will briefly reiterate some of the proposed ideas.

9.2.1 Multiplexing based OCT

For the polarisation sensitive applications, the multiplexer could potentially benefit from the use of non-birefringent materials in the Bragg cells. That would allow increasing the number of channels to allow the measurement of Jones and even Mueller matrices using several simultaneous polarisation sensitive channels in the reference arm.

Another imaging modality which could potentially benefit from employing our proposed multiplexing method is structured interference OCT. This method was so far presented in a few peer reviewed communications only. If such method can be confirmed to benefit OCT, then the frequency multiplexing methods presented in this thesis could be employed to perform structural imaging. The Bragg cell multiplexer presented in this thesis allows independent modulation of optical power in each channel in the reference arm of the OCT setup. Therefore, images with multiple phase shifted illumination patterns can be acquired during the time it takes to scan a single frame.

This could lead to increased quality data needed for reconstructing the high resolution images when motile targets are being imaged.

9.2.2 Closed-loop tracking for accurate data acquisition in low coherence interferometry based imaging and monitoring

The closed loop tracking based imaging setup presented in chapter 8 can be enhanced by the addition of an axial closed-loop tracking modality. This addition would enhance the reliability of drosophila monitoring and imaging. Additionally, axial tracking could benefit other possible applications in microscopy such as imaging single blood cells *in vivo* or for observing the embryos of animals or small animals that are naturally suspended in liquid, such as zebrafish.

Alternatively, the functionality of the closed loop tracking based set-up, presented in this thesis could be extended by including a simultaneous swept source based imaging channel. That would allow acquisition of M-mode recordings in addition to Doppler monitoring.

9.3 List of publications

Journal papers

M. Zurauskas, J. Rogers, A. G. Podoleanu. Multiple-depth simultaneous *en face* Optical Coherence Tomography Imaging. *Optics express* 21 (2), 1925-1936, 2013.

M. Zurauskas, A. Bradu, A. G. Podoleanu. Frequency multiplexed long range swept source optical coherence tomography. *Biomedical optics express* 4 (6), 778-788, 2013.

M. Zurauskas, A. G. Podoleanu. Multiplexing-based polarization sensitive *en face* optical coherence tomography. *Journal of biomedical optics* 18 (10), 106010, 2013.

M. Zurauskas, A. Bradu, D. R. Ferguson, D. X. Hammer, A. G. Podoleanu. Closed loop tracked Doppler optical coherence tomography based heart monitor for the *Drosophila melanogaster* larvae. *Journal of biophotonics* 2015.

Conference proceedings

M. Zurauskas, J. Rogers, A. G. Podoleanu. A versatile frequency domain multiplexer for optical coherence tomography. *Frontiers in Optics 2012/Laser Science XXVIII, OSA Technical Digest Optical Society of America*, paper FTu1C.2, 2012. (Oral presentation).

M. Zurauskas, J. Rogers, A. G. Podoleanu. Polarization sensitive *en face* optical coherence tomography using multichannel acousto-optic deflectors. *Proc. SPIE 8571, Optical Coherence Tomography and Coherence Domain Optical Methods in Biomedicine XVII*, 85710X, March 20, 2013. (Oral presentation).

M. Zurauskas, A. G. Podoleanu. A versatile frequency domain multiplexer for optical coherence tomography. *Proc. SPIE 8914, International Symposium on Photoelectronic*

Detection and Imaging 2013: Fiber Optic Sensors and Optical Coherence Tomography, 89141C, August 29, 2013. (Oral presentation).

M. Zurauskas, A. Bradu, A. G. Podoleanu. Frequency multiplexed long range swept source optical coherence tomography. *Proc. SPIE 8934, Optical Coherence Tomography and Coherence Domain Optical Methods in Biomedicine XVIII*, 89340L, March 4, 2014. (Oral presentation).

Patent application

A. Podoleanu, **M. Zurauskas**, J. Rogers. Multiple paths measuring and imaging apparatus and method. *US pat. app.* 14/025,970, 2013.

Appendix A

Supplementary list of technical documents about selected instruments used in the work presented in this thesis

Acousto-optic deflectors *Gooch and Housego 46080-1-.85-LTD.*

Digital frequency synthesiser *Gooch and Housego MSD040-150-0.8ADS2-A5H-8X1.*

Spectrum analyser *HP 8590A.*

Balanced photodetector receiver *New Focus 1807 .*

Universal motion controller *Newport ESP300.*

Actuator *Newport LTA-HS.*

Balanced photodetector *Nirvana model 2007.*

DAQ card *NI PCI-5124*.

DAQ card *NI PCI-6110*.

Connector block *NI SCB-68*.

PSI customized retinal tracker.

Function generator *Stanford research systems DS335*.

Function generator *Stanford Research DS345*.

Low noise preamplifier *Stanford Research SR560*.

Broadband SLD light source *Superlum S840-B-I-20*.

Swept source *Superlum Broad-sweeper 840*.

Super luminescent diode *Superlum SLD-531*.

Frequency generator *Thurlby Thandar Instruments TG210*.

Bibliography

- [1] M. Adhi and J. S. Duker. Optical coherence tomography—current and future applications. *Current opinion in ophthalmology*, 24(3):213, 2013.
- [2] D. C. Adler, Y. Chen, R. Huber, J. Schmitt, J. Connolly, and J. G. Fujimoto. Three-dimensional endomicroscopy using optical coherence tomography. *Nature Photonics*, 1(12):709–716, 2007.
- [3] A. Ahmad, S. G. Adie, E. J. Chaney, U. Sharma, and S. A. Boppart. Cross-correlation-based image acquisition technique for manually-scanned optical coherence tomography. *Optics express*, 17(10):8125–8136, 2009.
- [4] M. K. Al-Qaisi and T. Akkin. Polarization-sensitive optical coherence tomography based on polarization-maintaining fibers and frequency multiplexing. *Optics Express*, 16:13032–13041, 2008.
- [5] D. W. Arathorn. *Map-seeking circuits in visual cognition: A computational mechanism for biological and machine vision*. Stanford University Press, 2002.
- [6] D. W. Arathorn, Q. Yang, C. R. Vogel, Y. Zhang, P. Tiruveedhula, and A. Roorda. Retinally stabilized cone-targeted stimulus delivery. *Optics express*, 15(21):13731–13744, 2007.
- [7] G. B. Arden and P. A. Constable. The electro-oculogram. *Progress in retinal and eye research*, 25(2):207–248, 2006.

- [8] A. Bachmann, R. Leitgeb, and T. Lasser. Heterodyne fourier domain optical coherence tomography for full range probing with high axial resolution. *Optics Express*, 14:1487–1496, 2006.
- [9] T. Bajraszewski, M. Wojtkowski, M. Szkulmowski, A. Szkulmowska, R. Huber, and A. Kowalczyk. Improved spectral optical coherence tomography using optical frequency comb. *Optics Express*, 16:4163–4176, 2008.
- [10] C. Blatter, S. Coquoz, B. Grajciar, A. S. G. Singh, M. Bonesi, R. M. Werkmeister, L. Schmetterer, and R. A. Leitgeb. Dove prism based rotating dual beam bidirectional doppler oct. *Biomedical Optics Express*, 4:1188–1203, 2013.
- [11] B. Bouma. *Handbook of optical coherence tomography*. Informa Health Care, 2001.
- [12] B. Braaf, K. V. Vienola, C. K. Sheehy, Q. Yang, K. A. Vermeer, P. Tiruveedhula, D. W. Arathorn, A. Roorda, and J. F. de Boer. Real-time eye motion correction in phase-resolved oct angiography with tracking slo. *Biomedical optics express*, 4(1):51–65, 2013.
- [13] A. Bradu, L. Neagu, and A. Podoleanu. Extra long imaging range swept source optical coherence tomography using re-circulation loops. *Optics Express*, 18:25361–25370, 2010.
- [14] S. Brand, J. M. Ponomeros, B. E. Bouma, G. J. Tearney, C. C. Compton, and N. S. Nishioka. Optical coherence tomography in the gastrointestinal tract. *Endoscopy*, 32:796–803, 2000.
- [15] M. E. Brezinski. *Optical coherence tomography: principles and applications*. Academic press, 2006.

- [16] S. A. Burns, R. Tumber, A. E. Elsner, D. Ferguson, and D. X. Hammer. Large-field-of-view, modular, stabilized, adaptive-optics-based scanning laser ophthalmoscope. *JOSA A*, 24(5):1313–1326, 2007.
- [17] A. G. Capps, R. J. Zawadzki, Q. Yang, D. W. Arathorn, C. R. Vogel, B. Hamann, and J. S. Werner. Correction of eye-motion artifacts in ao-oct data sets. In *SPIE BiOS*, pages 78850D–78850D. International Society for Optics and Photonics, 2011.
- [18] X. Chen, H. Xie, R. Erkamp, K. Kim, C. Jia, J. Rubin, and M. O’Donnell. 3-d correlation-based speckle tracking. *Ultrasonic Imaging*, 27(1):21–36, 2005.
- [19] M. Choma, M. Sarunic, C. Yang, and J. Izatt. Sensitivity advantage of swept source and fourier domain optical coherence tomography. *Optics Express*, 11(18):2183–2189, 2003.
- [20] M. A. Choma, M. J. Suter, B. J. Vakoc, B. E. Bouma, and G. J. Tearney. Physiological homology between drosophila melanogaster and vertebrate cardiovascular systems. *Dis Model Mech*, 4(3):411–20, May 2011.
- [21] M. A. Choma, M. J. Suter, B. J. Vakoc, G. J. Tearney, and B. E. Bouma. Heart wall velocimetry and exogenous contrast-based cardiac flow imaging in drosophila melanogaster using doppler optical coherence tomography. *Journal of biomedical optics*, 15(5):056020–056020, 2010.
- [22] H. Collewijn, F. Van der Mark, and T. Jansen. Precise recording of human eye movements. *Vision research*, 15(3):447–455, 1975.
- [23] H. D. Crane and C. M. Steele. Generation-v dual-purkinje-image eyetracker. *Applied Optics*, 24(4):527–537, 1985.

- [24] R. G. Cucu, M. W. Hathaway, A. G. Podoleanu, and R. B. Rosen. Active axial eye motion tracking by extended range, closed loop opd-locked white light interferometer for combined confocal/en face optical coherence tomography imaging of the human eye fundus in vivo. In *European Conference on Biomedical Optics*, page 7372_1R. Optical Society of America, 2009.
- [25] R. G. Cucu, M. W. Hathaway, A. G. Podoleanu, and R. B. Rosen. Variable lateral size imaging of the human retina in vivo by combined confocal/en face optical coherence tomography with closed loop opd-locked low coherence interferometry based active axial eye motion tracking. In *BiOS*, pages 75540J–75540J. International Society for Optics and Photonics, 2010.
- [26] R. G. Cucu, J. Pedro, R. B. Rosen, and A. G. Podoleanu. Polarization-sensitive oct system using single-mode fiber. In *Proc. SPIE, Photonics North 2004: Photonic Applications in Telecommunications, Sensors, Software, and Lasers*, volume 5579, pages 170–177, 2004.
- [27] C. Dai, C. Zhou, S. Fan, Z. Chen, X. Chai, Q. Ren, and S. Jiao. Optical coherence tomography for whole eye segment imaging. *Optics Express*, 20:6109–6115, 2012.
- [28] D. P. Davé, T. Akkin, T. E. Milner, and H. G. R. lii. Phase-sensitive frequency-multiplexed optical low-coherence reflectometry. *Optics Communications*, 191:21–30, 2001.
- [29] J. F. de Boer, T. E. Milner, M. J. C. van Gemert, and J. S. Nelson. Two-dimensional birefringence imaging in biological tissue by polarization-sensitive optical coherence tomography. *Optics Letters*, 22:934–936, 1997.
- [30] A. Dhalla, D. Nankivil, T. Bustamante, A. Kuo, and J. A. Izatt. Simultaneous

- swept source optical coherence tomography of the anterior segment and retina using coherence revival. *Optics Letters*, 37:1883–1885, 2012.
- [31] A. Dhalla, D. Nankivil, and J. A. Izatt. Complex conjugate resolved heterodyne swept source optical coherence tomography using coherence revival. *Biomedical Optics Express*, 3:633–649, 2012.
- [32] Z. Ding, H. Ren, Y. Zhao, J. S. Nelson, and Z. Chen. High-resolution optical coherence tomography over a large depth range with an axicon lens. *Optics Letters*, 27:243–245, 2002.
- [33] W. Drexler and J. G. Fujimoto. *Optical coherence tomography: technology and applications*. Springer, 2008.
- [34] A. Dubra and Z. Harvey. Registration of 2d images from fast scanning ophthalmic instruments. In *Biomedical Image Registration*, pages 60–71. Springer, 2010.
- [35] S. Faisan, D. Lara, and C. Paterson. Scanning ophthalmoscope retinal image registration using one-dimensional deformation fields. *Optics express*, 19(5):4157–4169, 2011.
- [36] F. Fanjul-Vélez, M. Pircher, B. Baumann, E. Götzinger, C. Hitzenberger, and J. L. Arce-Diego. Polarimetric analysis of the human cornea measured by polarization-sensitive optical coherence tomography. *Journal of Biomedical Optics*, 15:056004–056004–10, 2010.
- [37] H. Feigenbaum. Role of m-mode technique in today’s echocardiography. *Journal of the American Society of Echocardiography*, 23(3):240–257, 2010.
- [38] F. Felberer, J.-S. Kroisamer, B. Baumann, S. Zotter, U. Schmidt-Erfurth, C. K.

- Hitzenberger, and M. Pircher. Adaptive optics slo/oct for 3d imaging of human photoreceptors in vivo. *Biomedical Optics Express*, 5(2):439–456, 2014.
- [39] R. D. Ferguson, D. X. Hammer, C. E. Bigelow, N. V. Iftimia, T. E. Ustun, S. A. Burns, A. E. Elsner, and D. R. Williams. Tracking adaptive optics scanning laser ophthalmoscope. In *Biomedical Optics 2006*, pages 613810–613810. International Society for Optics and Photonics, 2006.
- [40] R. D. Ferguson, D. X. Hammer, L. A. Paunescu, S. Beaton, and J. S. Schuman. Tracking optical coherence tomography. *Optics letters*, 29(18):2139–2141, 2004.
- [41] R. D. Ferguson, Z. Zhong, D. X. Hammer, M. Mujat, A. H. Patel, C. Deng, W. Zou, and S. A. Burns. Adaptive optics scanning laser ophthalmoscope with integrated wide-field retinal imaging and tracking. *JOSA A*, 27(11):A265–A277, 2010.
- [42] K. Goda, D. R. Solli, and B. Jalali. Real-time optical reflectometry enabled by amplified dispersive fourier transformation. *Applied Physics Letters*, 93(3):031106, 2008.
- [43] E. Götzinger, M. Pircher, B. Baumann, C. Hirn, C. Vass, and C. K. Hitzenberger. Retinal nerve fiber layer birefringence evaluated with polarization sensitive spectral domain oct and scanning laser polarimetry: A comparison. *Journal of Biophotonics*, 1:129–139, 2008.
- [44] A. P. Goutzoulis, D. R. Pape, and S. V. Kulakov. *Design and fabrication of acousto-optic devices*. Marcel Dekker, New York, 1994.
- [45] S.-Y. Guo, F.-T. Liao, M.-T. Su, C.-Y. Chang, H.-R. Su, J.-C. Huang, and W.-C. Kuo. Semiautomatic and rapid quantification of heartbeat parameters in drosophila using optical coherence tomography imaging. *Journal of biomedical optics*, 18(2):026004–026004, 2013.

- [46] J. Ha, M. Shishkov, M. Colice, W. Oh, H. Yoo, L. Liu, G. Tearney, and B. Bouma. Compensation of motion artifacts in catheter-based optical frequency domain imaging. *Optics express*, 18(11):11418–11427, 2010.
- [47] D. Hammer, R. D. Ferguson, N. Iftimia, T. Ustun, G. Wollstein, H. Ishikawa, M. Gabriele, W. Dilworth, L. Kagemann, and J. Schuman. Advanced scanning methods with tracking optical coherence tomography. *Optics express*, 13(20):7937–7947, 2005.
- [48] D. X. Hammer, R. Daniel Ferguson, M. Mujat, A. Patel, E. Plumb, N. Iftimia, T. Y. Chui, J. D. Akula, and A. B. Fulton. Multimodal adaptive optics retinal imager: design and performance. *JOSA A*, 29(12):2598–2607, 2012.
- [49] D. X. Hammer, R. D. Ferguson, C. E. Bigelow, N. V. Iftimia, T. E. Ustun, and S. A. Burns. Adaptive optics scanning laser ophthalmoscope for stabilized retinal imaging. *Optics express*, 14(8):3354–3367, 2006.
- [50] D. X. Hammer, R. D. Ferguson, J. C. Magill, M. A. White, A. E. Elsner, and R. H. Webb. Compact scanning laser ophthalmoscope with high-speed retinal tracker. *Applied optics*, 42(22):4621–4632, 2003.
- [51] M. R. Hee, D. Huang, E. A. Swanson, and J. G. Fujimoto. Polarization-sensitive low-coherence reflectometer for birefringence characterization and ranging. *Journal of the Optical Society of America B*, 9:903–908, 1992.
- [52] C. Hitzenberger, P. Trost, P. W. Lo, and Q. Zhou. Three-dimensional imaging of the human retina by high-speed optical coherence tomography. *Optics Express*, 11:2753–2761, 2003.
- [53] H. C. Ho, E. H. Young, and W. Seale. Microwave frequency translation with multiple bragg cells. In *Proc. SPIE, Optical Technology for Microwave Applications*

- VI and Optoelectronic Signal Processing for Phased-Array Antennas III*, volume 1703, pages 37–42, 1992.
- [54] B. Hofer, B. Považay, B. Hermann, A. Unterhuber, G. Matz, and W. Drexler. Dispersion encoded full range frequency domain optical coherence tomography. *Optics Express*, 17:7–24, 2009.
- [55] J. Holmes and S. Hattersley. Image blending and speckle noise reduction in multi-beam oct. In *Proc. SPIE, Optical Coherence Tomography and Coherence Domain Optical Methods in Biomedicine XIII*, volume 7168, pages 71681N–71681N–8, 2009.
- [56] D. Huang, E. A. Swanson, C. P. Lin, J. S. Schuman, W. G. Stinson, W. Chang, M. R. Hee, T. Flotte, a. A. P. K. Gregory, and J. G. Fujimoto. Optical coherence tomography. *Science*, 254:1178–1181, 1991.
- [57] Y. Huang, X. Liu, C. Song, and J. U. Kang. Motion-compensated hand-held common-path fourier-domain optical coherence tomography probe for image-guided intervention. *Biomedical optics express*, 3(12):3105–3118, 2012.
- [58] N. Iftimia, G. J. Tearney, and B. E. Bouma. Speckle reduction in optical coherence tomography by “path length encoded” angular compounding. *Journal of Biomedical Optics*, 8:260–263, 2003.
- [59] J. A. Izatt and A. M. Rollins. Frequency-encoded parallel oct and associated systems and methods, 10 2004. US Patent 6,775,007.
- [60] F. Jaillon, S. Makita, and Y. Yasuno. Variable velocity range imaging of the choroid with dual-beam optical coherence angiography. *Optics Express*, 20:385–396, 2012.

- [61] V. Jayaraman, J. Jiang, H. Li, P. Heim, G. Cole, B. Potsaid, J. G. Fujimoto, and A. Cable. Oct imaging up to 760kHz axial scan rate using single-mode 1310nm mems-tunable vcsels with >100nm tuning range. In *CLEO:2011 - Laser Applications to Photonic Applications*, page PDPB2. Optical Society of America, 2011.
- [62] M. W. Jenkins, M. Watanabe, and A. M. Rollins. Longitudinal imaging of heart development with optical coherence tomography. *Selected Topics in Quantum Electronics, IEEE Journal of*, 18(3):1166–1175, 2012.
- [63] Y. Jian, K. Wong, and M. V. Sarunic. Graphics processing unit accelerated optical coherence tomography processing at megahertz axial scan rate and high resolution video rate volumetric rendering. *Journal of biomedical optics*, 18(2):026002–026002, 2013.
- [64] R. C. Jones. A new calculus for the treatment of optical systems. *The Journal of the Optical Society of America*, 31:488–493, 1941.
- [65] H. H. Jr and R. C. Jones. A new calculus for the treatment of optical systems. *The Journal of the Optical Society of America*, 31:493–495, 1941.
- [66] M. J. Ju, Y. J. Hong, S. Makita, Y. Lim, K. Kurokawa, L. Duan, M. Miura, S. Tang, and Y. Yasuno. Advanced multi-contrast jones matrix optical coherence tomography for doppler and polarization sensitive imaging. *Optics Express*, 21:19412–19436, 2013.
- [67] W. Kang, H. Wang, Y. Pan, M. W. Jenkins, G. A. Isenberg, A. Chak, M. Atkinson, D. Agrawal, Z. Hu, and A. M. Rollins. Endoscopically guided spectral-domain oct with double-balloon catheters. *Optics Express*, 18:17364–17372, 2010.
- [68] K. H. Kim, M. C. Pierce, G. Maguluri, B. H. Park, S. J. Yoon, M. Lydon, R. Sheridan, and J. F. de Boer. In vivo imaging of human burn injuries with

- polarization-sensitive optical coherence tomography. *Journal of Biomedical Optics*, 17:066012–066012, 2012.
- [69] D. L. Kimmel, D. Mammo, and W. T. Newsome. Tracking the eye non-invasively: simultaneous comparison of the scleral search coil and optical tracking techniques in the macaque monkey. *Frontiers in behavioral neuroscience*, 6, 2012.
- [70] T. Klein, W. Wieser, C. M. Eigenwillig, B. R. Biedermann, and R. Huber. Megahertz oct for ultrawide-field retinal imaging with a 1050nm fourier domain mode-locked laser. *Optics Express*, 19:3044–3062, 2011.
- [71] T. Klein, W. Wieser, L. Reznicek, A. Neubauer, A. Kampik, and R. Huber. Multimhz retinal oct. *Biomedical optics express*, 4(10):1890–1908, 2013.
- [72] O. P. Kocaoglu, S. Lee, R. S. Jonnal, Q. Wang, A. E. Herde, J. C. Derby, W. Gao, and D. T. Miller. Imaging cone photoreceptors in three dimensions and in time using ultrahigh resolution optical coherence tomography with adaptive optics. *Biomedical optics express*, 2(4):748–763, 2011.
- [73] M. F. Kraus, B. Potsaid, M. A. Mayer, R. Bock, B. Baumann, J. J. Liu, J. Hornegger, and J. G. Fujimoto. Motion correction in optical coherence tomography volumes on a per a-scan basis using orthogonal scan patterns. *Biomedical optics express*, 3(6):1182–1199, 2012.
- [74] A. Kumar and G. Krol. Binocular infrared oculography. *The Laryngoscope*, 102(4):367–378, 1992.
- [75] A. Lang, P. Mousavi, S. Gill, G. Fichtinger, and P. Abolmaesumi. Multi-modal registration of speckle-tracked freehand 3d ultrasound to ct in the lumbar spine. *Medical image analysis*, 16(3):675–686, 2012.

- [76] F. LaRocca, D. Nankivil, S. Farsiu, and J. A. Izatt. Handheld simultaneous scanning laser ophthalmoscopy and optical coherence tomography system. *Biomedical optics express*, 4(11):2307–2321, 2013.
- [77] H. Y. Lee, H. Sudkamp, T. Marvdashti, and A. K. Ellerbee. Interleaved optical coherence tomography. *Optics Express*, 21:26542–26556, 2013.
- [78] J. Lee, V. Srinivasan, H. Radhakrishnan, and D. A. Boas. Motion correction for phase-resolved dynamic optical coherence tomography imaging of rodent cerebral cortex. *Optics express*, 19(22):21258–21270, 2011.
- [79] R. A. Leitgeb, C. K. Hitzenberger, A. F. Fercher, and T. Bajraszewski. Phase-shifting algorithm to achieve high-speed long-depth-range probing by frequency-domain optical coherence tomography. *Optics Letters*, 28:2201–2203, 2003.
- [80] M. K. K. Leung, A. Mariampillai, B. A. Standish, K. K. C. Lee, N. R. Munce, I. A. Vitkin, and V. X. D. Yang. High-power wavelength-swept laser in littman telescope-less polygon filter and dual-amplifier configuration for multichannel optical coherence tomography. *Optics Letters*, 34:2814–2816, 2009.
- [81] A. Li, O. O. Ahsen, J. J. Liu, C. Du, M. L. McKee, Y. Yang, W. Wasco, C. H. Newton-Cheh, C. J. O'Donnell, J. G. Fujimoto, et al. Silencing of the drosophila ortholog of sox5 in heart leads to cardiac dysfunction as detected by optical coherence tomography. *Human molecular genetics*, 22(18):3798–3806, 2013.
- [82] C. Li, J. A. Zeitler, Y. Dong, and Y.-C. Shen. Non-destructive evaluation of polymer coating structures on pharmaceutical pellets using full-field optical coherence tomography. *Journal of pharmaceutical sciences*, 103(1):161–166, 2014.
- [83] H. Li, J. Lu, G. Shi, and Y. Zhang. Tracking features in retinal images of adaptive

- optics confocal scanning laser ophthalmoscope using klt-sift algorithm. *Biomedical optics express*, 1(1):31–40, 2010.
- [84] H. Li, J. Lu, G. Shi, and Y. Zhang. Measurement of oxygen saturation in small retinal vessels with adaptive optics confocal scanning laser ophthalmoscope. *Journal of biomedical optics*, 16(11):110504–1105043, 2011.
- [85] F-T. Liao, C.-Y. Chang, M.-T. Su, and W.-C. Kuo. Necessity of angiotensin-converting enzyme-related gene for cardiac functions and longevity of *drosophila melanogaster* assessed by optical coherence tomography. *Journal of biomedical optics*, 19(1):011014–011014, 2014.
- [86] G. Liu, Z. Zhi, and R. K. Wang. Digital focusing of oct images based on scalar diffraction theory and information entropy. *Biomedical Optics Express*, 3:2774–2783, 2012.
- [87] L. Liu and N. Chen. Dynamic focusing with radial gratings for in vivo high resolution imaging. In *Proc. SPIE, Coherence Domain Optical Methods and Optical Coherence Tomography in Biomedicine XII*, volume 6847, pages 684718–684718–8, 2008.
- [88] X. Liu, Y. Huang, P. Gehlbach, and J. U. Kang. Freehand oct with real-time lateral motion tracking. In *SPIE BiOS*, pages 85711P–85711P. International Society for Optics and Photonics, 2013.
- [89] X. Liu, Y. Huang, and J. U. Kang. Distortion-free freehand-scanning oct implemented with real-time scanning speed variance correction. *Optics Express*, 20(15):16567–16583, 2012.
- [90] X. Liu, Y. Huang, J. C. Ramella-Roman, S. A. Mathews, and J. U. Kang. Quantitative transverse flow measurement using optical coherence tomography speckle decorrelation analysis. *Optics letters*, 38(5):805–807, 2013.

- [91] X. Liu and J. U. Kang. Tracking both magnitude and direction of 2-d transverse motion with optical coherence tomography. In *SPIE BiOS*, pages 89340I–89340I. International Society for Optics and Photonics, 2014.
- [92] D. G. Lowe. Distinctive image features from scale-invariant keypoints. *International journal of computer vision*, 60(2):91–110, 2004.
- [93] L. Ma, A. Bradu, A. G. Podoleanu, and J. W. Bloor. Arrhythmia caused by a drosophila tropomyosin mutation is revealed using a novel optical coherence tomography instrument. *PloS one*, 5(12):e14348, 2010.
- [94] S. Manzanera, M. A. Helmbrecht, C. J. Kempf, and A. Roorda. Mems segmented-based adaptive optics scanning laser ophthalmoscope. *Biomedical optics express*, 2(5):1204–1217, 2011.
- [95] A. Mariampillai, B. A. Standish, N. R. Munce, C. Randall, G. Liu, J. Y. Jiang, A. E. Cable, I. A. Vitkin, and V. X. Yang. Doppler optical cardiogram gated 2d color flow imaging at 1000 fps and 4d in vivo visualization of embryonic heart at 45 fps on a swept source oct system. *Optics Express*, 15(4):1627–1638, 2007.
- [96] S. Martinez-Conde, S. L. Macknik, and D. H. Hubel. The role of fixational eye movements in visual perception. *Nature Reviews Neuroscience*, 5:229–240, 2004.
- [97] A. Meadway, C. A. Girkin, and Y. Zhang. A dual-modal retinal imaging system with adaptive optics. *Optics Express*, 21(24):29792–29807, 2013.
- [98] M. Mujat, R. D. Ferguson, A. H. Patel, N. Iftimia, N. Lue, and D. X. Hammer. High resolution multimodal clinical ophthalmic imaging system. *Optics express*, 18(11):11607–11621, 2010.

- [99] O. Müller, S. Donner, T. Klinder, I. Bartsch, A. Krüger, A. Heisterkamp, and B. Rosenhahn. Compensating motion artifacts of 3d in vivo sd-oct scans. In *Medical Image Computing and Computer-Assisted Intervention–MICCAI 2012*, pages 198–205. Springer, 2012.
- [100] J. Mulligan. Recovery of motion parameters from distortions in scanned images. In *NASA CONFERENCE PUBLICATION*, pages 281–292. NASA, 1998.
- [101] L. Neagu, A. Bradu, L. Ma, J. W. Bloor, and A. G. Podoleanu. Multiple-depth en face optical coherence tomography using active recirculation loops. *Optics Letters*, 35:2296–2298, 2010.
- [102] K. Ocorr, T. Akasaka, and R. Bodmer. Age-related cardiac disease model of drosophila. *Mechanisms of ageing and development*, 128(1):112–116, 2007.
- [103] K. Ocorr, M. Fink, A. Cammarato, S. I. Bernstein, and R. Bodmer. Semi-automated optical heartbeat analysis of small hearts. *Journal of visualized experiments: JoVE*, 1(31), 2009.
- [104] K. Ocorr, N. L. Reeves, R. J. Wessells, M. Fink, H.-S. V. Chen, T. Akasaka, S. Yasuda, J. M. Metzger, W. Giles, J. W. Posakony, et al. Kcnq potassium channel mutations cause cardiac arrhythmias in drosophila that mimic the effects of aging. *Proceedings of the National Academy of Sciences*, 104(10):3943–3948, 2007.
- [105] K. Ocorr, G. Vogler, and R. Bodmer. Methods to assess drosophila heart development, function and aging. *Methods*, 68(1):265–272, 2014.
- [106] B. Park and J. Boer. Polarization-sensitive optical coherence tomography. In W. Drexler and J. Fujimoto, editors, *Optical Coherence Tomography, Biological and Medical Physics, Biomedical Engineering*, pages 653–695. Springer Berlin Heidelberg, 2008.

- [107] L. A. Paunescu, D. X. Hammer, R. D. Ferguson, S. Beaton, H. Ishikawa, J. C. Magill, G. Wollstein, and J. S. Schuman. Active retinal tracker for clinical optical coherence tomography systems. *Journal of biomedical optics*, 10(2):024038–02403811, 2005.
- [108] A. Peltsch, A. Hemraj, A. Garcia, and D. P. Munoz. Age-related trends in saccade characteristics among the elderly. *Neurobiology of Aging*, 20:669–679, 2011.
- [109] S. Periaswamy and H. Farid. Elastic registration in the presence of intensity variations. *Medical Imaging, IEEE Transactions on*, 22(7):865–874, 2003.
- [110] M. Pircher, B. Baumann, H. Sattmann, C. K. Hitzenberger, et al. Simultaneous slo/oct imaging of the human retina with axial eye motion correction. *Optics express*, 15(25):16922–16932, 2007.
- [111] M. Pircher, E. Götzinger, H. Sattmann, R. A. Leitgeb, and C. K. Hitzenberger. In vivo investigation of human cone photoreceptors with slo/oct in combination with 3d motion correction on a cellular level. *Optics express*, 18(13):13935–13944, 2010.
- [112] M. Pircher, C. K. Hitzenberger, and U. Schmidt-Erfurth. Polarization sensitive optical coherence tomography in the human eye. *Progress in Retinal and Eye Research*, 30:431–451, 2011.
- [113] A. Podoleanu. Multiple path interferometer and method, 08 2013. US Patent 8,514,404.
- [114] A. Podoleanu, M. Zurauskas, and J. Rogers. Multiple paths measuring and imaging apparatus and method, 09 2013. US Patent App. 14/025,970.
- [115] A. G. Podoleanu. Unique interpretation of talbot bands and fourier domain white light interferometry. *Optics Express*, 15:9867–9876, 2007.

- [116] A. G. Podoleanu. Route to oct from ofs at university of kent. *Photonic Sensors*, 1:166–186, 2011.
- [117] A. G. Podoleanu. Optical coherence tomography. *Journal of Microscopy*, 247:209–219, 2012.
- [118] A. G. Podoleanu, R. G. Cucu, J. Pedro, R. Weitz, D. A. Jackson, and R. B. Rosen. Hybrid configuration for simultaneous en-face oct imaging at different depths. In *Proc. SPIE, Advanced Sensor Systems and Applications II*, volume 5634, pages 160–165, 2005.
- [119] A. G. Podoleanu, G. M. Dobre, D. J. Webb, and D. A. Jackson. Simultaneous en-face imaging of two layers in the human retina by low-coherence reflectometry. *Optics Letters*, 22:1039–1041, 1997.
- [120] A. G. Podoleanu, J. A. Rogers, R. C. Cucu, D. A. Jackson, B. Wacogne, H. Porte, and T. Gharbi. Simultaneous low coherence interferometry imaging at two depths using an integrated optic modulator. *Optics Communications*, 191:21–30, 2001.
- [121] B. Potsaid, B. Baumann, D. Huang, S. Barry, A. E. Cable, J. S. Schuman, J. S. Duker, and J. G. Fujimoto. Ultrahigh speed 1050nm swept source / fourier domain oct retinal and anterior segment imaging at 100,000 to 400,000 axial scans per second. *Optics Express*, 18:20029–20048, 2010.
- [122] B. Potsaid, I. Gorczynska, V. J. Srinivasan, Y. Chen, J. Jiang, A. Cable, and J. G. Fujimoto. Ultrahigh speed spectral/fourier domain oct ophthalmic imaging at 70,000 to 312,500 axial scans per second. *Optics express*, 16(19):15149–15169, 2008.
- [123] S. Ricco, M. Chen, H. Ishikawa, G. Wollstein, and J. Schuman. Correcting motion artifacts in retinal spectral domain optical coherence tomography via image

- registration. In *Medical Image Computing and Computer-Assisted Intervention–MICCAI 2009*, pages 100–107. Springer, 2009.
- [124] N. A. Riza. Acousto-optically switched optical delay lines. *Optics Communications*, 145:15–20, 1998.
- [125] N. A. Riza and D. Psaltis. Acousto-optic signal processors for transmission and reception of phased array antenna signals. *Applied Optics*, 30:3294–3303, 1991.
- [126] N. A. Riza and Z. Yaqoob. Submicrosecond speed optical coherence tomography system design and analysis by use of acousto-optics. *Applied Optics*, 42:3018–3026, 2003.
- [127] D. A. Robinson. A method of measuring eye movement using a scieral search coil in a magnetic field. *Bio-medical Electronics, IEEE Transactions on*, 10(4):137–145, 1963.
- [128] J. A. Rogers, A. Bradu, and A. G. Podoleanu. Polarization maintaining multiple-depth en face optical coherence tomography system using active re-circulation loops in the non-stationary state. *Optics Express*, 20:29196–29209, 2012.
- [129] R. Rosen, M. van Velthoven, P. Garcia, R. Cucu, M. de Smet, T. Muldoon, and A. G. Podoleanu. Ultrahigh-resolution combined coronal optical coherence tomography confocal scanning ophthalmoscope (oct/slo): a pilot study. *Spektrum der Augenheilkunde*, 21(1):17–28, 2007.
- [130] J. O.-M. S. Martinez-Conde and S. L. Macknik. The impact of microsaccades on vision: towards a unified theory of saccadic function. *Nature Reviews Neuroscience*, 14:83–96, 2013.
- [131] B. Sahin, B. Lamory, X. Levecq, F. Harms, and C. Dainty. Adaptive optics with

- pupil tracking for high resolution retinal imaging. *Biomedical optics express*, 3(2):225–239, 2012.
- [132] H. Sakoe and S. Chiba. Dynamic programming algorithm optimization for spoken word recognition. *Acoustics, Speech and Signal Processing, IEEE Transactions on*, 26(1):43–49, 1978.
- [133] C. E. Saxer, J. F. de Boer, B. H. Park, Y. Zhao, Z. Chen, and J. S. Nelson. High-speed fiber based polarization-sensitive optical coherence tomography of in vivo human skin. *Optics Letters*, 76:1355–1357, 2000.
- [134] K. Schoenenberger, B. W. Colston, D. J. Maitland, L. B. D. Silva, and M. J. Everett. Mapping of birefringence and thermal damage in tissue by use of polarization-sensitive optical coherence tomography. *Applied Optics*, 37:6026–6036, 1998.
- [135] W. Seale. Acousto optic modulator model number: 23080-x-1.06-ltd, 2006. Operating manual.
- [136] S. Sénatore, V. R. Reddy, M. Sémériva, L. Perrin, and N. Lalevée. Response to mechanical stress is mediated by the trpa channel painless in the drosophila heart. *PLoS genetics*, 6(9):e1001088, 2010.
- [137] C. K. Sheehy, Q. Yang, D. W. Arathorn, P. Tiruveedhula, J. F. de Boer, and A. Roroda. High-speed, image-based eye tracking with a scanning laser ophthalmoscope. *Biomedical optics express*, 3(10):2611–2622, 2012.
- [138] J. Shi and C. Tomasi. Good features to track. In *Computer Vision and Pattern Recognition, 1994. Proceedings CVPR'94., 1994 IEEE Computer Society Conference on*, pages 593–600. IEEE, 1994.

- [139] M. Shirashaki. Large angular dispersion by a virtually imaged phased array and its application to a wavelength demultiplexer. *Optics Letters*, 21:366–368, 1996.
- [140] K. Sláma. A new look at the comparative physiology of insect and human hearts. *Journal of insect physiology*, 58(8):1072–1081, 2012.
- [141] H. Song, X. Qi, W. Zou, Z. Zhong, and S. A. Burns. Dual electro-optical modulator polarimeter based on adaptive optics scanning laser ophthalmoscope. *Optics Express*, 11:21892–21904, 2010.
- [142] S. B. Stevenson and A. Roorda. Correcting for miniature eye movements in high resolution scanning laser ophthalmoscopy. In *Biomedical Optics 2005*, pages 145–151. International Society for Optics and Photonics, 2005.
- [143] S. B. Stevenson, A. Roorda, and G. Kumar. Eye tracking with the adaptive optics scanning laser ophthalmoscope. In *Proceedings of the 2010 symposium on eye-tracking research & applications*, pages 195–198. ACM, 2010.
- [144] D. Stifter, P. Burgholzer, O. Höglinger, E. Götzinger, and C. K. Hitzenberger. Polarisation-sensitive optical coherence tomography for material characterisation and strain-field mapping. *Applied Physics A*, 76:947–951, 2003.
- [145] D. Stifter, E. Leiss-Holzinger, Z. Major, B. Baumann, M. Pircher, E. Götzinger, C. K. Hitzenberger, and B. Heise. Dynamic optical studies in materials testing with spectral-domain polarization-sensitive optical coherence tomography. *Optics Express*, 18:25712–25725, 2010.
- [146] M. Sugita, S. Zotter, M. Pircher, T. Makihira, K. Saito, N. Tomatsu, M. Sato, P. Roberts, U. Schmidt-Erfurth, and C. K. Hitzenberger. Motion artifact and speckle noise reduction in polarization sensitive optical coherence tomography by retinal tracking. *Biomedical optics express*, 5(1):106–122, 2014.

- [147] E. A. Swanson, J. Izatt, C. Lin, J. Fujimoto, J. Schuman, M. Hee, D. Huang, and C. Puliafito. In vivo retinal imaging by optical coherence tomography. *Optics letters*, 18(21):1864–1866, 1993.
- [148] P. Thevenaz, U. E. Ruttimann, and M. Unser. A pyramid approach to subpixel registration based on intensity. *Image Processing, IEEE Transactions on*, 7(1):27–41, 1998.
- [149] M.-T. Tsai, F.-Y. Chang, C.-K. Lee, T.-T. Chi, K.-M. Yang, L.-Y. Lin, J.-T. Wu, and C. Yang. Observations of cardiac beating behaviors of wild-type and mutant drosophilae with optical coherence tomography. *Journal of biophotonics*, 4(9):610–618, 2011.
- [150] B. J. Vakoc, D. Fukumura, R. K. Jain, and B. E. Bouma. Cancer imaging by optical coherence tomography: preclinical progress and clinical potential. *Nature Reviews Cancer*, 254:1178–1181, 1991.
- [151] K. V. Vienola, B. Braaf, C. K. Sheehy, Q. Yang, P. Tiruveedhula, D. W. Arathorn, J. F. de Boer, and A. Roorda. Real-time eye motion compensation for oct imaging with tracking slo. *Biomedical optics express*, 3(11):2950–2963, 2012.
- [152] C. R. Vogel, D. W. Arathorn, A. Roorda, and A. Parker. Retinal motion estimation in adaptive optics scanning laser ophthalmoscopy. *Optics express*, 14(2):487–497, 2006.
- [153] B. Wang, B. Yin, J. Dwelle, H. G. Rylander, M. K. Markey, and T. E. Milner. Path-length-multiplexed scattering-angle-diverse optical coherence tomography for retinal imaging. *Optics Letters*, 21:4374–4377, 2013.
- [154] N. Weiss, T. G. van Leeuwen, and J. Kalkman. Doppler-based lateral motion tracking for optical coherence tomography. *Optics letters*, 37(12):2220–2222, 2012.

- [155] W. Wieser, B. R. Biedermann, T. Klein, C. M. Eigenwillig, and R. Huber. Multi-megahertz oct: High quality 3d imaging at 20 million a-scans and 4.5 gvoxels per second. *Optics Express*, 18:14685–14704, 2010.
- [156] W. Wieser, B. R. Biedermann, T. Klein, C. M. Eigenwillig, and R. Huber. Multi-megahertz oct: high quality 3d imaging at 20 million a-scans and 4.5 gvoxels per second. *Biomedical Optics Express*, 3:2647–2657, 2012.
- [157] M. Wiesner, J. Ihlemann, H. H. Müller, E. Lankenau, and G. Hüttmann. Optical coherence tomography for process control of laser micromachining. *Review of Scientific Instruments*, 81(3):033705, 2010.
- [158] M. J. Wolf, H. Amrein, J. A. Izatt, M. A. Choma, M. C. Reedy, and H. A. Rockman. Drosophila as a model for the identification of genes causing adult human heart disease. *Proc Natl Acad Sci U S A*, 103(5):1394–9, Jan 2006.
- [159] T. Xie, S. Guo, Z. Chen, D. Mukai, and M. Brenner. Grin lens rod based probe for endoscopic spectral domain optical coherence tomography with fast dynamic focus tracking. *Optics express*, 14:3238–3246, 2006.
- [160] J. C. Yang, J. Wright, T. S. Huang, and Y. Ma. Image super-resolution via sparse representation. *Ieee Transactions on Image Processing*, 19:2861–2873, 2010.
- [161] Q. Yang, D. W. Arathorn, P. Tiruveedhula, C. R. Vogel, and A. Roorda. Design of an integrated hardware interface for aoslo image capture and cone-targeted stimulus delivery. *Optics express*, 18(17):17841–17858, 2010.
- [162] G. Yao and L. V. Wang. Two-dimensional depth-resolved mueller matrix characterization of biological tissue by optical coherence tomography. *Optics Letters*, 24:537–539, 1999.

- [163] J. Yi, Q. Wei, H. F. Zhang, and V. Backman. Structured interference optical coherence tomography. *Optics letters*, 37(15):3048–3050, 2012.
- [164] R. J. Zawadzki, A. G. Capps, D. Y. Kim, A. Panorgias, S. B. Stevenson, B. Hamann, and J. S. Werner. Progress on developing adaptive optics–optical coherence tomography for in vivo retinal imaging: Monitoring and correction of eye motion artifacts. *Selected Topics in Quantum Electronics, IEEE Journal of*, 20(2):1–12, 2014.
- [165] R. J. Zawadzki, A. R. Fuller, S. S. Choi, D. F. Wiley, B. Hamann, and J. S. Werner. Correction of motion artifacts and scanning beam distortions in 3d ophthalmic optical coherence tomography imaging. In *Biomedical Optics (BiOS) 2007*, pages 642607–642607. International Society for Optics and Photonics, 2007.
- [166] C. Zhou, A. Alex, J. Rasakanthan, and Y. Ma. Space-division multiplexing optical coherence tomography. *Optics Express*, 21:19219–19227, 2013.
- [167] C. Zhou, J. Wang, , and S. Jiao. Dual channel dual focus optical coherence tomography for imaging accommodation of the eye. *Optics Express*, 17:8947–8955, 2009.
- [168] H. Zhu, S. O. Isikman, O. Mudanyali, A. Greenbaum, and A. Ozcan. Optical imaging techniques for point-of-care diagnostics. *Lab on a Chip*, 13(1):51–67, 2013.